Investigation of the CO Density in a Microscaled Dielectric Barrier Discharge using TALIF

Master Thesis

in the
degree program
„Master of Science"
in Physics

at the Faculty of Physics and Astronomy
of the Ruhr-Universität Bochum

by
Oliver Robert Krettek

from
Moers

Bochum 2025

April 16, 2025
by Oliver Robert Krettek
oliver.krettek@ruhr-uni-bochum.de
Faculty of Physics and Astronomy of the Ruhr-Universität Bochum
Experimental Physics II - Plasma Interface Physicsg
Supervisor and first reviewer: Jun.-Prof. Dr. Judith Golda
Second reviewer: Dr. Marc Böke

Deutsche Zusammenfassung

In dieser Arbeit wird die Umwandlung von CO_2 zu CO mittels einer mikroskalierten dielektrisch behinderten Entladung mit der Methode der Zwei-Photonen-Absorptions Laser-induzierten-Fluoreszenz (TALIF) untersucht. Dafür wurde ein TALIF-Experiment aufgebaut und optimiert, das sowohl einen Photomultiplier als auch eine ICCD-Kamera enthält. Für die Anregung wurde der Übergang $B^1\Sigma^+(\nu' = 0) \leftarrow X^1\Sigma^+(\nu'' = 0)$ benutzt, während die Fluoreszenz aus dem Übergang $B^1\Sigma^+(\nu' = 0) \rightarrow A^1\Pi(\nu'' = 2)$ detektiert wurde. Wichtige Systemparameter des Aufbaus, einschließlich der Stabilität der Laserenergie, Polarisation des Laser-Strahls, Einstellungen der Second Harmonic Generator (SHG) und Third Harmonic Generator (THG) Kristalle sowie die Überprüfung des Bereichs der Laserenergie in Bezug auf den linearen oder gesättigten Bereich, wurden charakterisiert, um genaue Messungen zu ermöglichen.

Experimente zur CO-Produktion durch das Plasma wurden sowohl im stationären Modus in einer Gasatmosphäre sowie in einem gasdurchströmten Modus durchgeführt. Messungen der Rotationstemperatur, die für die Berechnung der absoluten CO-Dichte benötigt werden, zeigten keinen Anstieg ebendieser im Plasma. Der stationäre Modus des Plasmabetriebs zeigt einen linearen Anstieg der CO-Dichte über die Zeit, mit einer maximalen CO_2-zu-CO Konversionsrate von 3.5 %, während im gasdurchströmten Modus eine Konversionsrate von 3.2 % gemessen wurde, die über die Zeit konstant blieb. Eine Variation der Parameter führte zu der höchsten gemessenen CO-Dichte in dieser Arbeit von $1 \cdot 10^{22}\,\mathrm{m}^{-3}$, was einer Konversionsrate von 3.7 % entspricht. Diese Konversionsraten passen zu bereits gemessenen Konversionsraten dieser DBD. Eine Spannungsvariation zeigte ein lineares Verhältnis zwischen absoluter CO-Dichte und angelegter Spannung, während eine Abstandsvariation zeigte, dass die absolute CO-Dichte mit Abstand zum Plasma abnimmt.

Während die absoluten CO-Dichten erfolgreich bestimmt werden konnten, konnte die räumliche Auflösung der CO-Produktion aufgrund des geringen Signal-zu-Rausch Verhältnisses nicht gemessen werden. Außerdem wurden die Experimente zur Gasbeimischung im Strömungsmodus durch Einschränkungen der Gasdurchfluss-Regelung beeinträchtigt.

English abstract

This thesis investigates the conversion of CO_2 to CO using a microscaled dielectric barrier discharge (DBD) with the method of two-photon-absorption laser-induced fluorescence (TALIF). A TALIF setup was developed and optimised, incorporating both a photomultiplier and an ICCD camera. For the excitation, the $B^1\Sigma^+(\nu' = 0) \leftarrow X^1\Sigma^+(\nu'' = 0)$ transition was used, while fluorescence was detected coming from the $B^1\Sigma^+(\nu' = 0) \rightarrow A^1\Pi(\nu'' = 2)$ transition. Key system parameters, including laser energy stability, beam polarisation, adjustion of the second harmonic generator (SHG) and third harmonic generator (THG) crystals, as well as verification of the laser energy in regards of the linear or saturated regime, were characterised to ensure accurate measurements.

Experiments regarding the CO production by the plasma were conducted in a stationary mode in a controlled atmosphere, as well as in a gas flowing mode. Rotational temperature measurements, needed for calculation of absolute CO densities, showed no increase of the temperature of the CO in the plasma. The stationary mode shows a linear increase in CO density over time, with a maximum CO_2-to-CO conversion rate of 3.5 %, while the flowing mode shows a conversion of 3.2 % when reaching an equilibrium. Parameter variation lead to the highest absolute CO density of $1 \cdot 10^{22}\,\mathrm{m}^{-3}$, corresponding to a conversion of 3.7 % for the flowing mode. These conversion rates are in accordance with previously measured conversion rates of this DBD. A voltage variation study demonstrated a linear relationship between applied voltage and CO density, while a distance variation showed that the absolute CO density decreases with distance to the plasma.

While absolute CO densities were successfully determined, spatial resolution of CO production was not achieved due to low signal-to-noise ratios. Additionally, flow control limitations affected gas admixture experiments in flowing mode.

Contents

1 Introduction

1.1 Motivation

One of the biggest challenges mankind is facing right now is global climate change [1]. The main mechanism behind climate change is the emission of so-called greenhouse gases, for example methane (CH_4), nitrous oxide (N_2O) and especially carbon dioxide (CO_2) [2]. When fossil fuels are burned, large quantities of CO_2 are released into the atmosphere [3]. The majority of the world's energy production still relies on fossil fuels [4]. With substantial amounts of CO_2 in the atmosphere, sunlight reflected by Earth's surface can be absorbed by the CO_2, as it very efficiently absorbs infrared radiation [5], which then consequently increases the global temperature.

Climate change has enormous consequences: the global average temperature has risen by roughly 1.5° C in comparison to the average from 1850 to 1900 [6], extreme weather events are occurring more frequently [7] and the ice shelves at the poles are melting [8, 9].
Since climate change has many effects, various approaches exist to combat it, affecting multiple areas of life. One example is the increased use of renewable energy sources such as solar and wind energy, with solar energy having a great potential [10].

A direct approach to tackling this problem would be the destruction of CO_2. This could potentially be achieved using non-thermal plasmas [11], which have gained research attention in recent years. In non-thermal plasmas, chemical reactions can deviate significantly from pathways in thermal equilibrium. One of the main researched non-thermal plasmas which is applied in atmospheric pressure are dielectric barrier discharges (DBDs) [12]. DBDs typically consist of two electrodes with a dielectric material placed between them. The insulator prevents arcing, which would destroy the reactor due to the high current. A high voltage is applied to the electrodes. When the DBD operates in a gas atmosphere or even in a gas-flowing mode, with the right conditions, a plasma can be ignited.

This thesis is written within the framework of the *Collaborative Research Centre (CRC) 1316: Transient atmospheric plasmas - from plasmas to liquids to solids.* The CRC is researching energy efficient substance conversion with the combination of non-thermal atmospheric plasmas and catalysis. The sub-project *A6: Pulsed plasma interaction with catalytic surfaces within micro-structured array devices* investigates micro-cavities plasma arrays (MCPA). Within the MCPA, discharges are ignited in µm-scale cavities. The cavities are cut into a nickel-foil, forming a metal-grid, which has a longer lifetime than comparable silica-based arrays [14, 13]. These reactors have already been studied in terms of electric field strengths [15], electric field components [16], intra-cavity dynamics [17] and oxygen densities [18] as well as surface charges [19]. The oxygen densities show, that the MCPA has a very high dissociation efficiency and a high reactivity. The measurements in [16, 18] therefore lay a very good foundation for the use of catalysts. In the future, MCPAs should be investigated regarding the conversion of volatile organic compounds (VOCs), which are harmful to the environment. In this thesis, the conversion of CO_2 to CO is investigated. This aligns with the direct approach of CO_2 destruction, as mentioned earlier, and is also a preparation for the conversion of VOCs, as one of the products can be CO.

Due to the small dimension of the MCPA, particularly the cavities, not all diagnostics commonly used in plasma physics are suitable for investigating the destruction of CO_2. One indirect approach with a powerful diagnostic is the measurement of CO, which is a product of CO_2 destruction, using the method of two-photon-absorption laser-induced fluorescence (TALIF). This method can spatially resolve absolute CO densities directly over the cavities of the MCPA, though not directly within the discharge due to the geometry of the MCPA. With a calibration, absolute densities of the ground state can be obtained [20], in contrast to densities often determined in plasma research using methods such as actinometry, where models are needed for the ground state. The production of CO, which is toxic to humans, is linked to the Fischer-Tropsch process. This process consists of a series of chemical reactions that convert CO and hydrogen, coming for example from methane and coal, into liquid hydrocarbons. Since crude oil is a finite fossil resource, alternatives are being explored. Methane and coal are available in significantly larger quantities and are considered promising interim solutions until renewable fuels become widely viable [21].

In this thesis, TALIF is deployed with both a photomultiplier (PMT) and an intensified charge-coupled device (ICCD) camera. The upside of the photomultiplier lies in its high-speed analysis capability. When correctly focussed, each laser shot exciting the CO molecules and the subsequent de-excitation can be measured. This allows for a much faster data acquisition compared to the ICCD camera, which requires an integration time to capture an image. This enables efficient determination of CO rotational temperatures, as wavelength scans can be conducted relatively quickly with the PMT. However, with the current setup, the PMT cannot spatially resolve fluorescence. This is where the ICCD camera excels: with proper calibration and background measurement, spatial distribution measurements are straightforward.

1.2 Structure of this thesis

The main goal of this thesis is to measure absolute CO densities. For this, the following intermediate steps can be formulated:

- Development of the TALIF setup incorporating both a photomultiplier and an ICCD camera.
- Measurement of rotational temperatures of CO originating from the plasma
- Calculation of absolute CO densities under different plasma conditions by varying the plasma mode (stationary and flowing) and plasma parameters. Additionally, to obtain spatial resolution of the CO density.

On the experimental side, the experiment setup of the TALIF system is described. First, a characterisation of the laser is required, including parameters such as laser energy, beam profile, and wavelength. Additionally, the use of the second harmonic generator (SHG) and third harmonic generator (THG) is explained. The characteristics of the photomultiplier, photodiode for triggering, and ICCD camera are also determined.
On the theoretical side, a simulation program for excitation spectra is developed. Furthermore, a program for absolute density calculations from ICCD images must be implemented. In addition, the setup was automated for PMT measurements.

2 Theoretical Background

Investigating plasma-produced carbon monoxide using TALIF is a complex and challenging task. This chapter provides the necessary theoretical background in various fields of physics that play a role: the plasma physics of the dielectric barrier discharge, the plasma chemistry involved in carbon monoxide production, and the measurement process, particularly aspects related to lasers, molecular physics, and optics. The first section presents a physical description of the plasma source used in this thesis.

2.1 Dielectric Barrier Discharge

The plasma source investigated in this thesis is a dielectric barrier discharge (DBD). The defining characteristic of DBDs is the presence of an insulating layer within the plasma channel. This insulator prevents arcing and leads to a self-pulsing plasma mode, enabling the generation of non-thermal plasma at atmospheric pressure. The first DBD was demonstrated in 1857 by Werner von Siemens [22], with the goal of producing ozone. Today, DBDs have numerous applications, including surface treatment [23], plasma-chemical processes in combination with catalysts [24], and the decomposition of harmful chemicals [25], among many others [26].

2.1.1 Types of DBD

Although DBDs are used in a wide range of applications, and various configurations exist, they can generally be categorised into three main types: volume DBDs, surface DBDs, and coplanar DBDs. These are schematically illustrated in figure 2.1. In volume DBDs, one or both electrodes are covered with an insulator, and the plasma is formed in the volume between them. In surface DBDs, the insulator is placed between the electrodes, allowing the plasma to exist only on its surface. In the coplanar configuration, both electrodes are embedded within the insulator, and the discharge occurs above the insulator's surface [27]. In reality, these geometries are often more complex, as electrode arrangements are not always symmetric.

To ignite DBDs, an alternating voltage in the range of several kilovolts with frequencies in the kilohertz range is typically applied [26]. The exact parameters depend on the reactor geometry and the gas composition. Once ignition occurs, the insulator becomes charged, generating an electric field opposing the applied voltage. When the charge on the insulator exceeds the applied field, ignition ceases. The insulator thus acts as a barrier, preventing arcing. This is crucial, as arcing results in a thermal plasma, counteracting the purpose of DBDs as non-thermal plasma sources and destroying the electrodes.

2.1.2 Discharge Characteristics

DBDs can exhibit different characteristics and appearances. A key difference between volume DBDs and surface DBDs is the relationship between the applied voltage U and the effective power P_{eff}. This relationship is illustrated in figure 2.2. For volume DBDs, the effective power is directly proportional to the applied voltage, whereas for surface DBDs, it scales with U^2 [27]. The DBD used in this thesis, a Micro-Cavities Plasma-Array (MCPA), exhibits

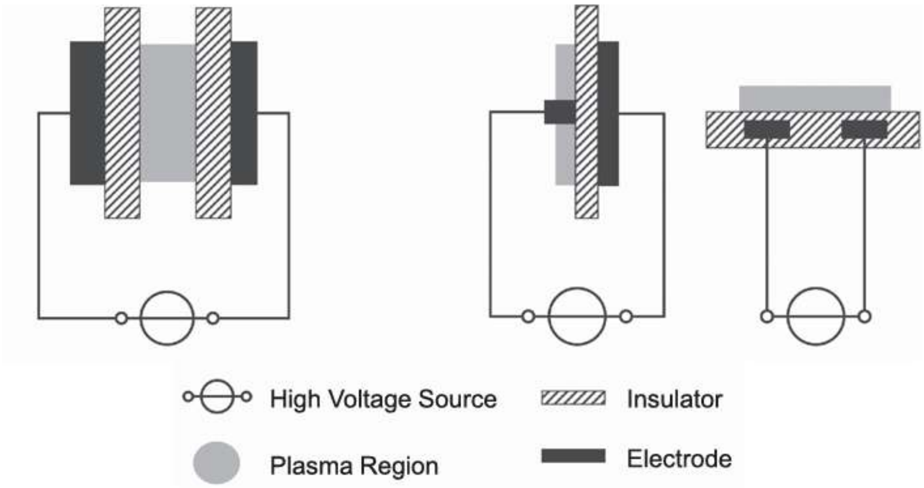

Figure 2.1: Schematic representation of different DBD reactor types, adapted from [27]. From left to right: volume DBD, surface DBD and coplanar DBD.

characteristics of both volume and surface DBDs [14], and is further described in section 3.2.

Another distinguishing feature of DBDs is their discharge appearance, which can be filamentary [28], homogeneous [29], or a mixture of both [30, 31]. At higher pressures, DBDs typically ignite in a filamentary mode due to the streamer mechanism. This is due to the higher pressure, where there are many collisions which lead to a high electron density. The high electron density then leads to a self-propagation of the ionisation wave, which is the streamer.

A unique property of DBDs is the memory effect. This effect refers to the phenomenon where the discharge is influenced by residual charge deposited on the insulator or by metastables in the volume [32]. The polarity of these charges changes with the alternating voltage, affecting subsequent discharge events, changing the γ-coefficient. The γ-coefficient, or second Townsend-coefficient, stands for the number of electrons that are generated per ion hitting the cathode. It is important for ignition, the local electric field and modifying the ignition voltage [33]. As the general principles behind DBDs are now described, the next section covers the plasma chemistry of CO_2, which leads to the formation of the CO-molecule.

2.2 Plasma Chemistry of CO_2

This section provides an overview of the involved plasma chemistry and describes the chemical reactions leading to the formation of CO from CO_2.
The dissociation of CO_2 into CO was thoroughly analysed by A. Fridman in *Plasma Chemistry* [34]. The primary decomposition reaction of CO_2 is:

$$CO_2 \rightarrow CO + O, \quad \Delta H = 5.5\,\mathrm{eV/mol} \tag{2.1}$$

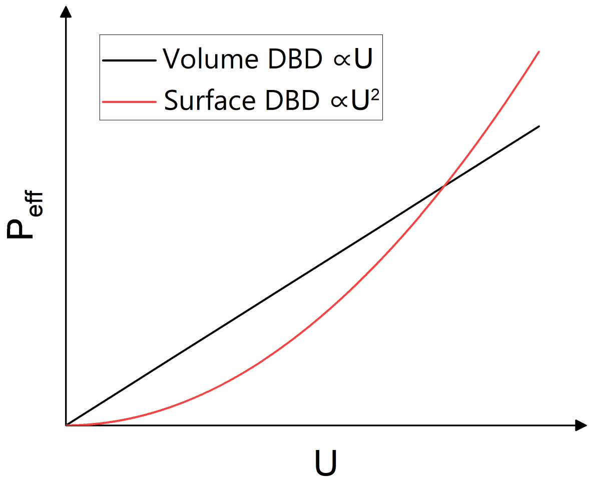

Figure 2.2: Effective power of volume DBDs $\propto U$ and surface DBDs $\propto U^2$ as a function of the applied voltage.

However, due to its high reactivity, the oxygen atom (O) rapidly reacts with other atoms or molecules or recombines with another oxygen atom. Consequently, the plasma-chemical process of CO_2 decomposition can be summarised as follows:

$$CO_2 \rightarrow CO + \frac{1}{2}O_2, \quad \Delta H = 2.9\,\text{eV/mol} \tag{2.2}$$

This is an endothermic process, meaning that energy input is required. The enthalpy change of this reaction is relatively high and comparable to the energy required for hydrogen production from water [34]. The research interest in dissociation of CO_2 arises from several key factors, including:

- CO_2-lasers: CO_2 dissociation is an important process in CO_2-lasers, which rank among the most powerful lasers [35]. In this case, CO_2 dissociation is undesired.
- Industrial applications: CO_2 dissociation has diverse applications, for example power plant exhaust treatment and synthesis of new transportation fuels [34].

On the other side, CO as a product of dissociation of CO_2 has also use cases, for example in the hydrogen production: CO produced in plasma can be efficiently converted into hydrogen via the thermocatalytic reactions, without additional energy input [34]:

$$CO + H_2O \rightarrow CO_2 + H_2, \quad \Delta H = -0.4\,\text{eV/mol} \tag{2.3}$$

In the next subsections, the different ways of dissociation of CO_2, which all might play a role in context of this thesis for the CO production, are explained.

2.2.1 Dissociation of CO_2 in Plasmas by Stimulated Vibrational Excitation

There are multiple pathways for CO_2-dissociation in plasmas. According to [34], the most efficient mechanism is stimulated vibrational excitation of CO_2 molecules.

The plasma-electrons excite CO_2 vibrational states, with typical electron temperatures of $T_e \approx 1\,\text{eV}$. However, with the MCPA used in this thesis, higher electron temperatures of about $T_e \approx 4\,\text{eV}$ have been measured [36]. Despite this, the most efficient energy transfer mechanism remains unchanged, as illustrated in figure 2.3. Classifying the plasma used in this thesis, it has a value for E/n between $\approx 8 \cdot 10^{16}\,\text{V} \cdot \text{cm}^2$ and $\approx 10 \cdot 10^{16}\,\text{V} \cdot \text{cm}^2$ in this figure, so still in the range of vibrational excitation, according to measurements of the electric field strength [36]. The primary effect of higher electron temperatures is a shift in the vibrational excitation pathways, but vibrational excitation remains significantly more energy efficient than rotational or electronic excitation. Energy losses through vibrational relaxation are two orders of magnitude lower than the energy input, as indicated by Fridman [34].

This results in significant overpopulation of vibrational levels in the CO_2 ground state $^1\Sigma^+$. The higher vibrational states are further populated through vibrational-vibrational (V-V) relaxation processes [34]. If a highly vibrational excited state gains enough energy that in sum exceeds the dissociation threshold E_D, it can undergo dissociation according to equation 2.1.

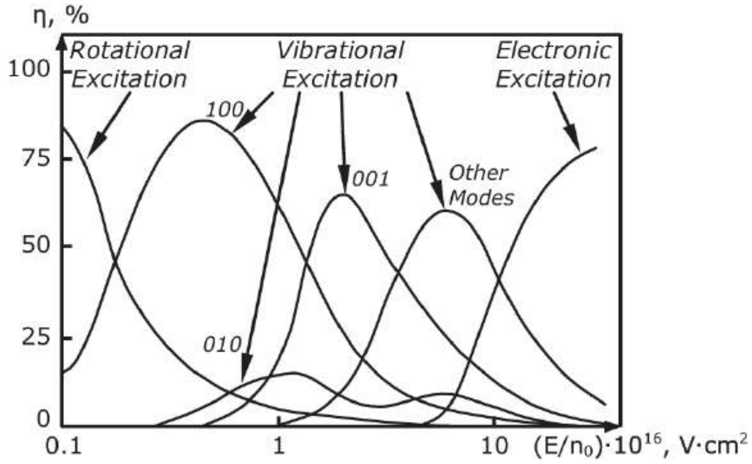

Figure 2.3: The image shows fractions of non-thermal plasma energy transfer from plasma electrons to different excitation paths of the CO_2-molecule, taken from [34]. The plasma used in this thesis is in the range of vibrational excitation.

Figure 2.4 illustrates the low-energy electronic states of the CO_2 molecule and the possible dissociation paths. The direct dissociation process is:

$$CO_2^*(^1\Sigma^+) \rightarrow CO(^1\Sigma^+) + O(^1D) \tag{2.4}$$

This adiabatic process, which holds total spin conservation, requires an energy input of more than 7 eV, producing an electronically excited oxygen atom $O(^1D)$. Although electron energies in the range of 6–7 eV are theoretically available [36], alternative, more efficient dissociation pathways exist. A more effective route involves a stepwise vibrational excitation, leading to a non-adiabatic transition $^1\Sigma^+ \rightarrow {}^3B_2$:

$$CO_2^*(^1\Sigma^+) \rightarrow CO_2^*(^3B_2) \rightarrow CO(^1\Sigma^+) + O(^3P), \quad E = 5.5\,\text{eV/mol} \tag{2.5}$$

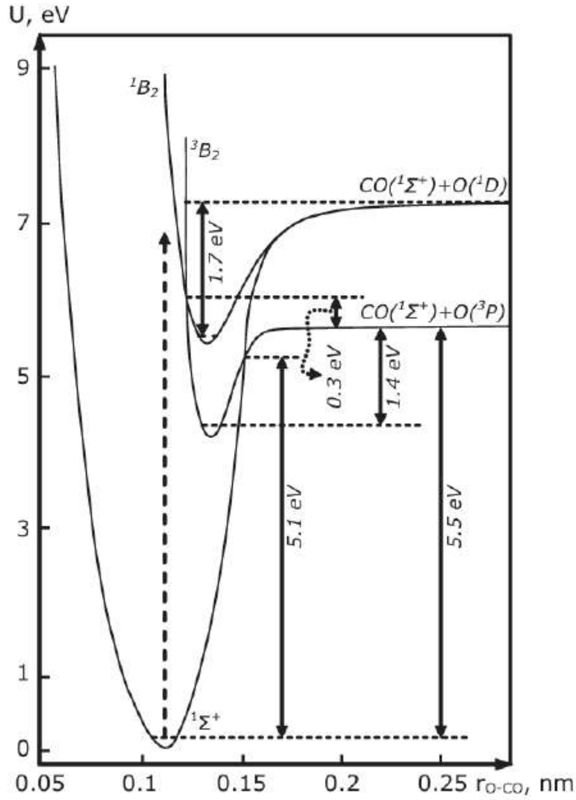

Figure 2.4: The image shows the low electronic terms of CO_2, taken from [34].

This process produces atomic oxygen in its electronic ground state $O(^3P)$ and requires 5.5 eV, exactly the energy of the $OC = O$ bond [34]. The atomic oxygen then reacts with another vibrationally excited CO_2-molecule:

$$O + CO_2^* \rightarrow CO + O_2, \quad \Delta H = 0.3\,\text{eV/mol}, \quad E \approx 0.5 - 1\,\text{eV/mol} \tag{2.6}$$

According to Rusanov and Fridman [34], when the vibrational temperature is sufficiently high ($T_v \geq 0.1\,\text{eV}$), this reaction is faster than the three-body recombination of atomic oxygen:

$$O + O + M \rightarrow O_2 + M \tag{2.7}$$

This pathway offers three advantages over alternative plasma-chemical dissociation mechanisms:

- Efficient energy transfer: At electron temperatures of $T_e \approx 1 - 2\,\text{eV}$, at least 95 % of the discharge energy can be transferred from plasma generated electrons to the vibrational excitation of the CO_2 molecules.

- Optimal dissociation mechanism: According to the α-model of Fridman and Macheret [34], vibrational excitation is the most effective means of stimulating CO_2 dissociation.

- Lower energy requirement: dissociation via vibrational excitation requires only 5.5 eV, compared to over 8 eV for direct electron impact dissociation (see figure 2.4). The Franck-Condon principle states that the transition from $CO_2(^1\Sigma^+)$ to the electronically excited state $CO_2(^1B_2)$ requires more than 8 eV. Dissociation then occurs via a transition from $CO_2(^1B_2)$ to $CO_2(^3B_2)$.

The next subsection covers an alternative way of CO_2-dissociation which also might occur to some degree in the plasma used in this thesis.

2.2.2 Dissociation of CO_2 in Plasmas by Electronic Excitation

If electron energies in the plasma are sufficiently high, a significant portion of CO_2 dissociation can occur via electronic excitation:

$$e^- + CO_2(^1\Sigma^+) \rightarrow CO(a^3\Pi) + O(^3P) \tag{2.8}$$

This process can be dominant, particularly in non-thermal plasmas that have high values of reduced electric fields E/p, which are typically found in low-pressure discharges [34]. In such cases, the vibrational excitation of CO_2 molecules is partially suppressed. However, the energy efficiency of this dissociation mechanism is limited by three factors:

- Higher energy requirement: The electron energy required for direct dissociation is greater than the O=CO bond energy.
- Inefficient energy transfer: At typical electron temperatures ($T_e \approx 1...2\,\mathrm{eV}$), only a small fraction of the discharge energy is transferred from electrons to electronic excitation.
- Competing excitations: High electron temperatures also populate other electronic states of CO_2 that do not contribute to dissociation, further reducing efficiency.

In the next subsection, the last way of CO_2-dissociation of interest is covered, as well as a summary of all three dissociation ways.

2.2.3 Dissociation of CO_2 in Plasmas by Dissociative Electron Attachment

Another mechanism for CO_2 dissociation is the dissociative attachment of electrons to CO_2-molecules:

$$e^- + CO_2 \rightarrow CO + O^- \tag{2.9}$$

The energy threshold for this reaction is lower than that of dissociation via electronic excitation. However, its cross section is relatively small ($\approx 10^{-18}\,\mathrm{cm}^2$) compared to the other dissociation pathways [34]. Consequently, this reaction contributes only marginally to the total kinetics of CO_2 dissociation, as shown in figure 2.5. Despite its limited role in dissociation, dissociative attachment plays a crucial role in charge balance and in sustaining non-thermal discharges. The energy efficiency of this process is limited primarily by the loss of an electron, which requires approximately 30–100 eV [34]. Although the electron can be recovered via associative detachment,

$$O^- + CO \rightarrow CO_2 + e^- \tag{2.10}$$

this process is inefficient, as it results in the loss of the dissociation product CO. Other mechanisms of CO_2 dissociation with losses of charged particles, for example dissociative recombination, are also not energy efficient due to the small cross section, as shown in figure 2.5.

In summary, different CO_2 dissociation mechanisms exhibit different energy efficiencies. Among them, vibrational excitation of CO_2 molecules from their electronic ground state $CO_2(^1\Sigma^+)$ has been identified as the most efficient dissociation pathway. However, all of the above mentioned CO_2 dissociation pathways might somewhat play a role in dissociation for the discharge used in this thesis.
In order to measure absolute CO densities, first it is crucial to understand the behaviour of molecules regarding their different energy levels. As the origin of the plasma-generated CO-molecules is explained now, the next section will cover absorption spectroscopy.

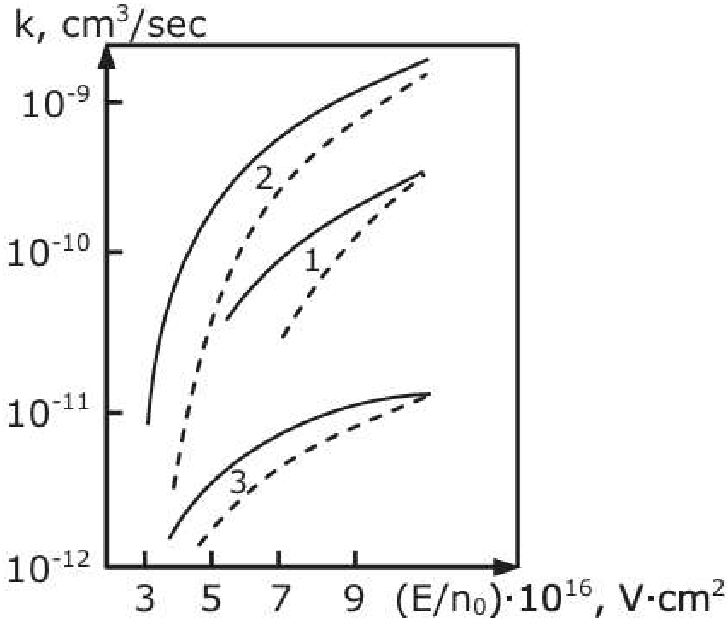

Figure 2.5: Rate coefficients as functions of the reduced electric field: (1) shows the CO_2 dissociation from direct electron impact, (2) electronic excitation and (3) dissociative electron attachment. The solid lines indicate calculations based on electron energy distribution functions in CO_2, while the dashed lines show it in CO. The image is taken from [34].

2.3 Absorption Spectroscopy

In this thesis, the goal is to measure absolute CO densities using TALIF. For this, we must first take a look at the principles of absorption spectroscopy. CO is a diatomic molecule which therefore has different energy levels for electronic, vibrational and rotational states. A schematic overview of this is shown in figure 2.6. The different electronic states as well as their excitation is described in section 2.5.2, where the selection of the states for TALIF is explained. In figure 2.6, the difference between electronic states, vibrational levels and rotational levels is illustrated in dependence of the energy. Electronic states have different potential wells, and contain different vibrational energy levels, which then itself contain different rotational energy levels.

The excitation to the different vibrational and rotational levels is described by the Franck-Condon principle (vibrational) and Hönl-London factors (rotational) which will be explained within the next subsections.

2.3.1 Franck-Condon Principle

The Franck-Condon factors govern the vibrational structure of transitions and can be understood by looking at a classical model of vibrational transitions.

The first assumption this model makes, is that the process of photon impact happens in a time interval that is short in comparison to one vibrational period [38]. Looking at this in a potential diagram as in figure 2.7, a calculation of the energy balance of the two radii yields

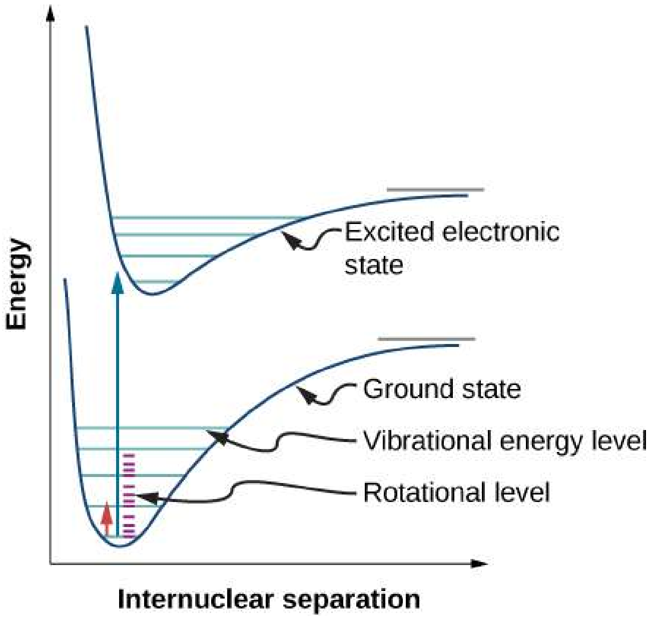

Figure 2.6: Schematic image of electronic, vibrational and rotational levels in a molecule. Taken from [37].

that the transition only occurs in molecules, when the two radii in the ground and excited state and their kinetic energies are equal. In quantum mechanical terms, this means that a transition at this point has the highest probability.
In figure 2.7, this is also illustrated, as the transition probability is highest when the overlap in the vibrational wave function is also at its maximum.

2.3.2 Hönl-London factors

The Hönl-London factors are used to determine how the intensity of a transition is spread between the different rotational transitions in the case for diatomic molecules and namely for carbon monoxide the O-, Q- and S-branches by TALIF. This is due to the selection rules only allowing transitions of $\Delta J = -2; 0; 2$, where J is the rotational quantum number. The calculations of the Hönl-London factors were done by Bray et al. [40] and also shown in [20]:

$$S_{ll}^{O} = C(2J+1)\frac{1}{45}\mu_s^2 b_{J-2,J} \tag{2.11}$$

$$S_{ll}^{Q} = C(2J+1)\left(\frac{1}{9}\mu_I^2 + \frac{1}{45}\mu_s^2 b_{J,J}\right) \tag{2.12}$$

$$S_{ll}^{S} = C(2J+1)\frac{1}{45}\mu_s^2 b_{J+2,J} \tag{2.13}$$

In these equations, C is a constant of normalisation ($S_{ll}^{O} + S_{ll}^{Q} + S_{ll}^{S} = 2J+1$) and both μ_s^2 and μ_I^2 are invariants of the two-photon polarisability tensor.
The factors $b_{J-2,J}, b_{J,J}$ and $b_{J+2,J}$ are Placzeck-Teller coefficients. These coefficients denote the relative strength between the branches for depolarised scattering [41]:

$$b_{J-2,J} = \frac{3J(J-1)}{2(2J+1)(2J-1)} \tag{2.14}$$

$$b_{J,J} = \frac{(J-1)}{(2J-1)(2J+3)} \tag{2.15}$$

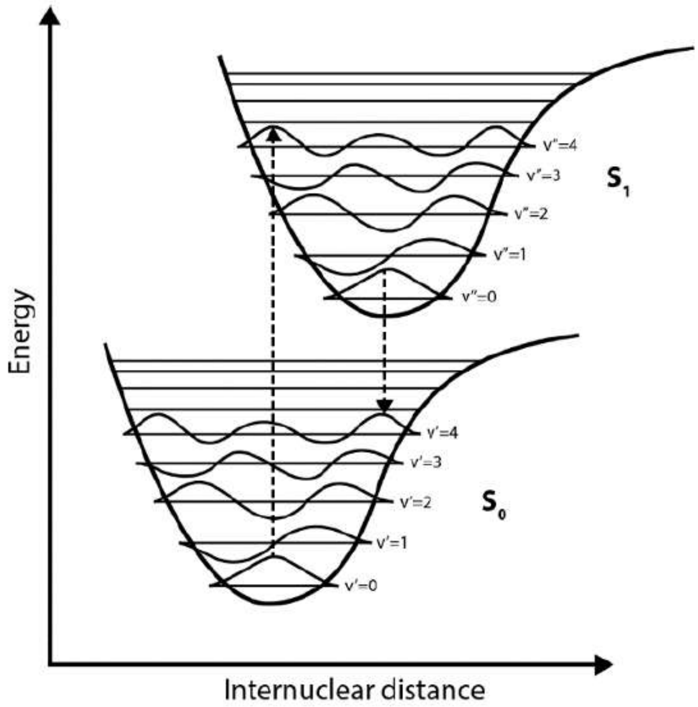

Figure 2.7: Schematic illustration of the Franck-Condon principle. Straight arrows indicate transitions between two electronic states. Within the electronic states, vibrational levels and their potentials are indicated. Taken from [39].

$$b_{J+2,J} = \frac{3(J+1)(J+2)}{2(2J+1)(2J+3)} \tag{2.16}$$

The Placzek-Teller coefficients equal unity, hence the normalisation C is:

$$C = \frac{1}{\frac{1}{9}\mu_I^2 + \frac{1}{45}\mu_s^2} \tag{2.17}$$

Now we have the equations for linearly polarised light. To compare the ratio to circularly polarised light, we need again the equation for the Hönl-London factor for the case of circularly polarised light, given by [40]:

$$S_{cc}^{Q} = C(2J+1)\frac{1}{30}\mu_s^2 b_{J,J} \tag{2.18}$$

The ratio between linearly and circulary polarised light is then:

$$\frac{S_{ll}^{Q}}{S_{cc}^{Q}} = \frac{2}{3}\left(1 + \frac{5\mu_I^2}{b_{J,J}\mu_s^2}\right) \tag{2.19}$$

The typical value for the ratio is over 200, experimentally validated in [42]. With this number, the ratio between μ_s^2 and μ_I^2 can be calculated and in the next step, the Hönl-London factors. The Hönl-London factors of the Q-branch for each $J \neq 0$ are two magnitudes larger then the ones of the O- and S-branch [20], as shown in figure 2.8. This is confirmed by other experiments, where the O- and S-branch are not detected [43]. These results justify the omission of the O- and S-branch in further calculations, if the used laser is polarised linearly. With that, the two rules for the excitation into vibrational and rotational levels are explained. With this knowledge, we can dive into the excitation spectra and the rotational temperature.

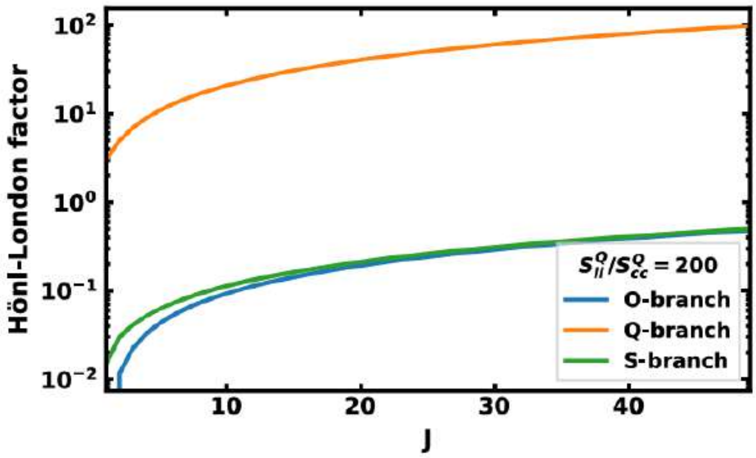

Figure 2.8: The image shows calculated and normalised Hönl-London factors of linearly and circularly polarised light S^Q_{ll}/S^Q_{cc} of value 200. Taken from [20].

2.3.3 Excitation Spectra and Rotational Temperature

When considering LIF and TALIF, two different spectra have to be considered: the excitation spectra and the fluorescence spectra. Both are illustrated in figure 2.9, where the excitation is indicated in blue and the fluorescence in red. As can be seen in figure 2.9, the excitation and the fluorescence both can go into different vibrational states of each electronic state. The rotational states are not illustrated. The rotational temperature indicates the states for an assumed Maxwell-Boltzmann distribution. If the rotational temperature is higher than the ambient temperature of the molecules, the population of the rotational states with the rotational quantum number J is shifted towards higher rotational levels. In this thesis, excitation spectra are measured: this means, that the excitation wavelength is varied, and the fluorescence spectrum is summed. From this, the information regarding the rotational temperature and, in the next step, of absolute CO density can be obtained.

With this knowledge, the next section covers the Laser-Induced Fluorescence, which lays the foundation for the Two-Photon Absorption Laser-Induced Fluorescence, the method that utilises the physics mentioned before.

2.4 Laser Induced Fluorescence

Before discussing Two-Photon Absorption Laser-Induced Fluorescence (TALIF), the principles of Laser-Induced Fluorescence (LIF) will be introduced. The fundamental theory behind LIF is analogous to that of TALIF but less complex.

LIF is a spectroscopic diagnostic technique used to detect specific species by selecting an appropriate laser wavelength. The photon energy is tuned to match the energy difference between two states, $|1\rangle$ and $|2\rangle$, of the target species. When the laser light hits the species, it excites electrons from the lower state $|1\rangle$, in most cases the ground state, to the higher state $|2\rangle$. This excitation process is governed by the Einstein coefficient B_{12} and the laser power density ρ, and selection rules determine the possible transitions. Once in the excited state $|2\rangle$, the species undergoes relaxation, characterised by a natural lifetime τ_{nat}. The relaxation can occur via different mechanisms:

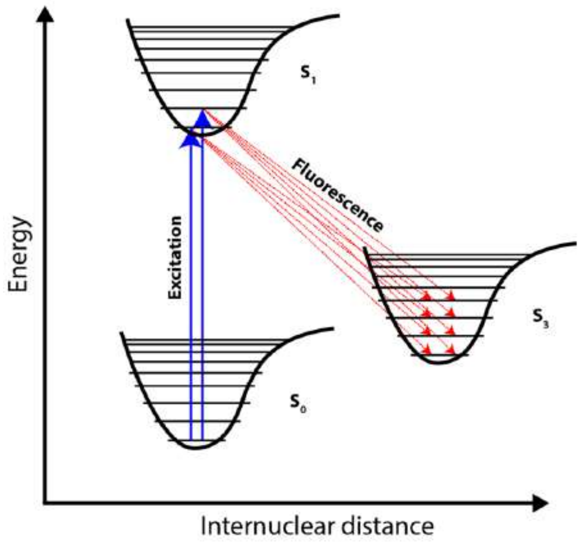

Figure 2.9: Schematic image of electronic excitation and fluorescence from different vibrational levels. Taken from [39].

- Stimulated Emission: The species can return to the ground state through stimulated emission, described by the product of the Einstein coefficient B_{21} and ρ.
- Spontaneous Emission: The species can decay spontaneously, governed by the Einstein coefficient A_{21}, falling back to the ground state.
- Fluorescence Emission: A transition to an intermediate state $|3\rangle$ can occur, described by the Einstein coefficient A_{23}. This transition is the desired fluorescence process for detection, as the emitted photon has a different energy compared to direct relaxation of the ground state. This is helpful because laser light can not be mistaken for fluorescence.
- Quenching: Quenching is the process of radiation-free relaxation via collisions with species, and is covered in subsection 2.4.2.

Fluorescence emission from state $|3\rangle$ is distinct and can be detected to obtain parameters such as species density and temperature. Since the final state $|3\rangle$ is generally different from the initial state $|1\rangle$, the selection rules again determine the possible transitions. A schematic illustration of this process is shown in figure 2.10. From this illustration, it is possible to derive a simple model that predicts the different populations of each state. This is done in the next subsection.

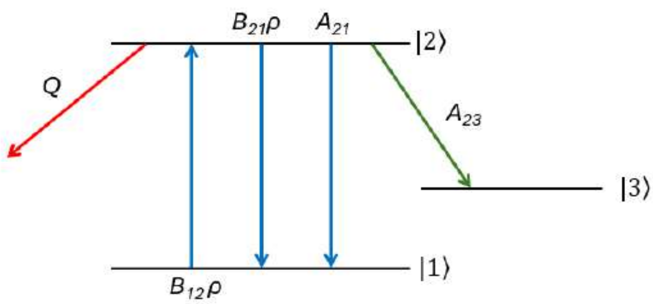

Figure 2.10: Schematic image of the energy levels in a LIF measurement.

2.4.1 Rate equations for LIF

For the simplified model shown in figure 2.10, rate equations describing the population dynamics of each state can be formulated. Using the same Einstein coefficients as in the figure, we define $n_i(t)$ as the time-dependent population of each state i. The rate equations, based on [44] and extended, are given by:

$$\frac{\partial n_1(t)}{\partial t} = -B_{12}\rho(t)n_1(t) + (B_{21}\rho(t) + A_{21})n_2(t) \tag{2.20a}$$

$$\frac{\partial n_2(t)}{\partial t} = B_{12}\rho(t)n_1(t) - (B_{21}\rho(t) + A_{21} + A_{23} + Q)n_2(t) \tag{2.20b}$$

$$\frac{\partial n_3(t)}{\partial t} = A_{23}n_2(t) - L \tag{2.20c}$$

with L being a loss term, e.g. due to quenching. The Einstein coefficients B_{ij} for stimulated absorption and emission can be calculated with the degeneracy g_i of each state:

$$B_{12} = \frac{g_2}{g_1}B_{21} \tag{2.21}$$

In the above rate equations, the laser power density is assumed to be constant over time and uniform across the absorption spectral interval. However, in reality, this is not the case, and the overlap between the laser and absorption line profiles must be considered:

$$\rho_\nu(t,\nu) = \rho_L(t)\epsilon(\nu - \nu_L) \tag{2.22}$$

Here, $\epsilon(\nu - \nu_L)$ is assumed to be a Gaussian laser line profile centered at the set wavelength ν_L, and $\rho_L(t)$ is the time-dependent laser power density. The laser power density is defined as:

$$\rho_L(t) = \frac{E_P \cdot \tau_L(t)}{A \cdot c} \tag{2.23}$$

with E_P being the energy of the laser pulse, assumed to be constant in time, $\tau_L(t)$ the normalised time profile and $A \cdot c$ being the product of the cross-sectional area of the laser beam and the speed of light. The absorption line profile is given by:

$$B_{ij}(\nu) = B_{ij} \cdot b(\nu - \nu_{ij}) \tag{2.24}$$

where the factor $b(\nu - \nu_{ij})$ stands for the normalised absorption line profile, centered at ν_{ij}. The interaction of the laser line profile with the species is influenced by two broadening mechanics: the pressure broadening and the Doppler broadening, shown in equations 2.25 and 2.26, respectively:

$$\Delta\omega_{\text{Pressure}} = p \cdot 0.74 \cdot \left(\frac{295}{T}\right)^{0.65} \tag{2.25}$$

$$\Delta\omega_{\text{Doppler}} = \frac{\nu}{c} \cdot \sqrt{\frac{8k_{\text{B}}T\ln(2)}{M_{\text{CO}}}} \tag{2.26}$$

In this equations, the $\Delta\omega_{\text{Pressure}}$ and $\Delta\omega_{\text{Doppler}}$ stand for the broadening of the laser line profile, p is the pressure, T the temperature, ν the laser-light frequency, the speed of light is c, k_{B} is the Boltzmann-constant and M_{CO} is the molar mass of CO. Since pressure broadening follows a Lorentzian distribution and Doppler broadening follows a Gaussian distribution, their convolution results in a Voigt profile.

Looking now into the coupled differential eqs. (2.20a) to (2.20c), some assumptions have to be made in order to solve them. At the start of the laser pulse at $t = 0$, the ground state has the density $n_1 = N$ while the higher states $n_2 = n_3 = 0$ are depleted. Also, it is assumed that stimulated emission does not occur. Therefore, the rate equation for the second state then can be written as:

$$\frac{\partial n_2(t)}{\partial t} = -(A_{21} + A_{23} + Q)n_2(t) \tag{2.27}$$

which has the solution:

$$n_2(t) = C \cdot \exp\left(\frac{-t}{A_{21} + A_{23} + Q}\right) \tag{2.28}$$

The denominator of the exponential can be summarised as an effective lifetime τ_{eff} as the sum of the lifetimes and the quenching:

$$\tau_{\text{eff}} = \frac{1}{A_{21} + A_{23} + Q_2} \tag{2.29}$$

To ensure the validity of these assumptions, the following has to be taken into account:

- The effective lifetime τ_{eff} must be small enough to deplete n_2 before the next laser pulse. Otherwise, n_2 would accumulate over time, making equation 2.28 inaccurate.
- As equation 2.29 shows, increasing quenching reduces τ_{eff}, which must be considered in analysis.
- The laser pulse duration τ_p should be much shorter than τ_{eff} to allow for accurate measurement of τ_{eff}. In this thesis, this is not the case, as later measurements show.

With this, the theoretical construct behind LIF is explained. This is the foundation for the theory behind TALIF. But before coming to that, the next subsection covers quenching, since it is already a crucial factor for LIF.

2.4.2 Quenching

Quenching is the radiation-free relaxation process caused by collisions between species, leading to a decrease in the fluorescence signal. If this effect were not accounted for, it would result in an underestimation of the absolute CO densities. A direct measurement of the change in the effective lifetime is not possible with this laser setup, as the laser pulse duration is in the nanosecond range and coincides with the effective lifetime. Another effect to consider is radiation trapping: Classically speaking, a fluorescence photon is emitted, absorbed, and re-emitted, thereby prolonging the effective lifetime. For these reasons, quenching will not be measured in this thesis but rather calculated.
The total quenching frequency Q consists of the sum of the quenching rate coefficients q_i, weighted by the fractions of the present species in the gas mixture f_i:

$$\mathrm{Q} = \left(q_{\text{He}} f_{\text{He}} + q_{\text{CO}} f_{\text{CO}} + q_{\text{CO}_2} f_{\text{CO}_2}\right) p \tag{2.30}$$

where p is the pressure. The values of the quenching rate coefficients are shown in table 2.1. Generally, quenching rate coefficients are temperature-dependent. However measurements in this thesis show that the temperature remains constant at room temperature, allowing for the calculation of the absolute CO density with satisfactory accuracy.
In later calculations of the density, the branching ratios are used:

$$a_{ik} = \frac{A_{ik}}{Q + \tau_{\text{nat}}^{-1}}. \tag{2.31}$$

With this description of quenching, it is now possible to look into the fluorescence, as this is the desired relaxation that will later be measured.

Table 2.1: Quenchers and their corresponding quenching rate coefficients in MHz/mbar, from [45]

Quencher	q [MHz/mbar]
He	0.083
CO	6.1
CO_2	26

2.4.3 Fluorescence

The total fluorescence light emitted originates from the second excited state $|2\rangle$, in the simplest case with no in-between states, where two different fluorescence pathways exist: back to the ground state or to a third state. This can be expressed mathematically as:

$$F = F_{21} + F_{23} = \int_0^\infty (A_{21} + A_{23}) n_2(t) dt \tag{2.32}$$

The population density of the second state can be determined using equations 2.20. Fluorescence behaviour depends on the laser power. Two distinct regimes exist:

- Linear regime: At lower laser powers, fluorescence intensity increases proportionally with laser power.
- Saturation regime: When the ground state is nearly depleted, fewer molecules remain available for excitation. As a result, fluorescence intensity plateaus. This is also the case in a Boltzmann-equilibrium, where the states $|1\rangle$ and $|2\rangle$ have approximately the same population.

This is shown in figure 2.11. In this thesis, measurements have been conducted to ensure that experiments remain in the linear regime. The saturation regime is avoided for two reasons: density calculations become more challenging, as the assumptions for their derivation no longer hold. The second reason is that the fluorescence intensity no longer changes with laser energy, making signal verification difficult.

Now, in the linear regime, it is possible to make two reasonable assumptions: First the stimulated emission from state 2 to state 1 is negligible. Second the spontaneous emission back to the first state is considered to be negligible in the case of this thesis for CO. This can be written as:

$$A_{23} >> B_{21}\rho(t) \tag{2.33a}$$

$$A_{23} >> A_{21} \tag{2.33b}$$

Those assumptions simplify the rate equations in 2.20 to:

$$\frac{\partial n_1(t)}{\partial t} = -B_{12}\rho(t) n_1(t)\Phi \tag{2.34a}$$

$$\frac{\partial n_2(t)}{\partial t} = B_{12}\rho(t) n_1(t)\Phi - (A_{23} + Q) n_2(t) \tag{2.34b}$$

where Φ is defined as the overlap integral between the normalised absorption line profile $b(\nu - \nu_{ij})$ and the laser line profile $\epsilon(\nu - \nu_L)$:

$$\Phi = \int_{-\infty}^{\infty} b(\nu - \nu_{ij}) \cdot \epsilon(\nu - \nu_L) \mathrm{d}v \tag{2.35}$$

Solving those equations leads to the fluorescence signal:

$$F = (1 - \exp(-B_{12}\rho(t)\Phi\tau_L)) \cdot \frac{A_{23}}{A_{23} + Q} \cdot N \tag{2.36}$$

with N being the density. When the ground state is far from depletion, the equation is simplified even more:

$$F = B_{12}\rho(t)\Phi\tau_L \cdot \frac{A_{23}}{A_{23} + Q} \cdot N \tag{2.37}$$

Here the dependence is clear: the fluorescence signal is linearly dependent on the density N as well as the laser power $\rho(t)$. The next subsection will cover the detection efficiency of the fluorescence, as this is crucial for obtaining reliable results.

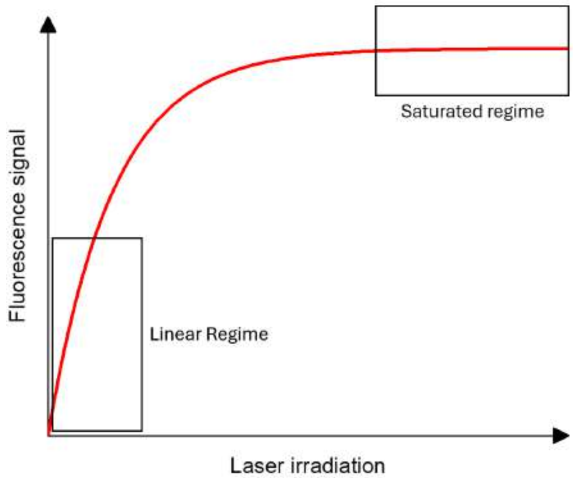

Figure 2.11: Fluorescence signal in dependence of the laser energy.

2.4.4 Detection efficiency of the fluorescence signal

The detectable fluorescence signal S is determined by the product of the fluorescence signal F and the detection efficiency G, which may be dependent on the detected wavelength λ:

$$S = F \cdot G(\lambda) \tag{2.38}$$

The detection efficiency is composed of the detection volume V_{det}, the solid angle Ω, the detection efficiency $\eta(\lambda)$ as well as the detection transmittance T:

$$G(\lambda) = V_{\text{det}} \cdot \frac{\Omega}{4\pi} T(\lambda)\eta(\lambda) \tag{2.39}$$

Since at least four different variables contribute to the detection efficiency, uncertainties in these parameters can introduce significant errors in signal measurements. This, in turn, would lead to inaccuracies in determining the absolute density of the species. To mitigate these uncertainties, it is more practical to perform a calibration of the optical path instead of relying on direct measurements of each individual component. This ensures a more accurate determination of the fluorescence signal and ultimately improves the reliability of absolute density measurements.

With that, the theoretical background needed for TALIF has been laid, and the next section will explore the TALIF method.

2.5 Two-photon absorption laser induced fluorescence

The energy required for a transition from the ground state to an excited state does not necessarily have to be in the visible range. If the transition requires more than 6.5 eV, the corresponding laser wavelength will be in the vacuum ultra-violet (VUV) range. This poses a challenge because VUV light is absorbed by air. Placing the entire laser path in a vacuum is often not feasible.

The solution to this problem is Two-Photon-Absorption Laser-Induced Fluorescence (TALIF). Instead of using a single high-energy UV photon, two lower-energy photons (maybe in the visible range) are used, whose combined energy matches the required excitation energy. The two photons do not necessarily need to have the same wavelength, although in this thesis, they do. The absorption takes place in this way: one photon hits the species and excites it to a virtual level, lying in-between the ground and upper state. When the second photon is absorbed, the species gets excited from the virtual state to the upper state. The energy diagram is shown in figure 2.12. The whole process happens instantaneously. In this thesis, TALIF is applied to CO. As done for LIF, it is possible to formulate rate equations for the populations of the different states, which is done in the next section.

2.5.1 Rate equations for TALIF

The rate equations previously derived for LIF remain, with minor adjustments, also valid for TALIF. One significant difference is that the selection rules have to be applied twice, since two photons are involved. The selection rule is then:

$$\Delta J = 0, \pm 2 \tag{2.40}$$

As a consequence, another important change to the LIF rate equations is that single photon stimulated emission back to the original ground state is not allowed. This means the factor $B_{21} = 0$ for the TALIF rate equations:

$$\frac{\partial n_1(t)}{\partial t} = -B_{12}\rho_{2P}(t)n_1(t) \tag{2.41a}$$

$$\frac{\partial n_2(t)}{\partial t} = B_{12}\rho_{2P}(t)n_1(t) - (A_{21} + A_{23} + Q)n_2(t) \tag{2.41b}$$

$$\frac{\partial n_3(t)}{\partial t} = A_{23}n_2(t) - L \tag{2.41c}$$

The factor $B_{12}\rho_{2P}(t)$ represents the laser power density in the case of two photons and consists of the two photon statistical factor $P^{(2)}$, the absorption cross section for two photons $\sigma^{(2)}$, the laser intensity $\hat{I}$ and the photon energy $h\nu$ and $g(\Delta\nu)$ being the normalised line profile, consisting of the convolution of one-photon spectral profile and the absorption line profile of CO [39]. Thus, the expression for two-photon absorption is:

$$B_{12}\rho_{2P}(t) = P^{(2)}\sigma^{(2)}g(\Delta\nu)\left(\frac{\langle\hat{I}(t)\rangle}{h\nu}\right)^2 \tag{2.42}$$

The two-photon cross sections are typically very low, which justifies the assumption that the ground state is far from depletion, meaning the TALIF signal is typically in the linear regime. Finally, the TALIF signal can be expressed as:

$$S_{TALIF} = G(\lambda) \cdot F = G(\lambda) \cdot \frac{\Sigma A}{\Sigma A + Q_2} P^{(2)}\sigma^{(2)}g(\Delta\nu)\left(\frac{\langle\hat{I}(t)\rangle}{h\nu}\right)^2 \tau_L N_{\mathrm{ref}} \tag{2.43}$$

It should be noted that, in this thesis, the TALIF experiment was setup from another TALIF experiment performed before, were atomic oxygen was measured. There is a huge difference between TALIF on CO and on atomic oxygen, as for the later, practically only a single wavelength is used. This is in contrast to TALIF on CO, where for absolute densities, a scan has to be made. The next section covers the principles behind TALIF on CO, especially the excitation spectrum.

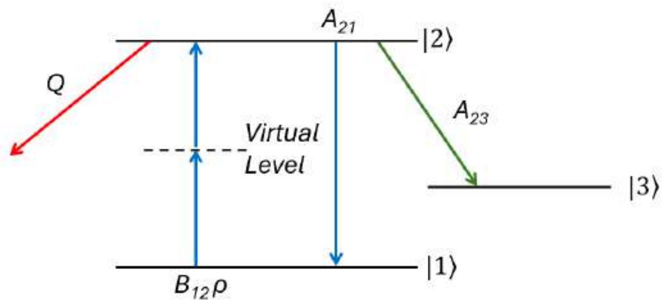

Figure 2.12: Schematic image of the energy levels in a TALIF measurement.

2.5.2 CO TALIF

Now that the TALIF method has been introduced, the next step is to determine the best excitation path, which is discussed in this section.
An energy diagram for CO is shown in figure 2.13. The ground state, denoted as the $|1\rangle$ state, is called $X^1\Sigma^+$. Possible excited states for $|2\rangle$ and $|3\rangle$ include:

- Triplet state $a^3\Pi$
- Singlet states: $A^1\Pi$, $B^1\Sigma^+$, $C^1\Sigma^+$, $E^1\Sigma^+$

Each of these states can be reached through direct excitation from the ground state.

Triplet state $a^3\Pi$
The first transition considered is $X^1\Sigma^+ \rightarrow a^3\Pi$. However, this is a forbidden transition due to the spin selection rule

$$\Delta S = 0. \tag{2.44}$$

This transition is therefore very weak [46] and meta-stable, meaning it has a long lifetime compared to other states. This makes it unsuitable for TALIF measurements.

Singlet state $A^1\Pi$
The next higher state is the $A^1\Pi$, which decays via fluorescence back to the ground state $X^1\Sigma^+$. This transition would emit light of the same wavelength as the laser, which falls into the VUV range. This overlap creates detection challenges due to strong Rayleigh scattering. Since the $|3\rangle$ state must be lower in energy than the $|2\rangle$ state, the $A^1\Pi$ state is chosen as $|3\rangle$. This is a convenient choice because all transitions from the higher states lie in the visible range of light, making the fluorescence less challenging to detect.

Now the question is, into which state $|2\rangle$ the stimulated excitation should happen.

State $E^1\Sigma^+$
The $E^1\Sigma^+$ state lies above the dissociation limit. Exciting CO into this state would result in molecular dissociation, making absolute density measurements impossible. This state is therefore not suitable.

Comparison of $B^1\Sigma^+$ and $C^1\Sigma^+$ state
The two remaining options for $|2\rangle$ are $B^1\Sigma^+$ and $C^1\Sigma^+$. The $C^1\Sigma^+$ state has the following characteristics:

- It has fluorescence in the visible range, making detection straightforward.
- $C^1\Sigma^+$ has a higher oscillator strength: The probability of absorption and emission is one to two orders of magnitude higher than for $B^1\Sigma^+$ [47, 48].
- However, this state has a very short natural lifetime of 2.2 ± 0.8 ns [49], which is an order of magnitude shorter than $B^1\Sigma^+$ (22.3 ± 0.5 ns) [45].
- With a nanosecond pulsed laser (pulse width up to 10 ns), this short lifetime overlaps with the laser pulse, making it difficult to resolve fluorescence signals. A picosecond laser would be required for accurate measurements. With a picosecond laser, the short lifetime would be a great advantage, as the time in which quenching could happen, is much shorter, thus increasing the fluorescence signal.
- Additionally, $C^1\Sigma^+$ lies above the dissociation limit, leading to molecular loss and thus reducing the fluorescence.

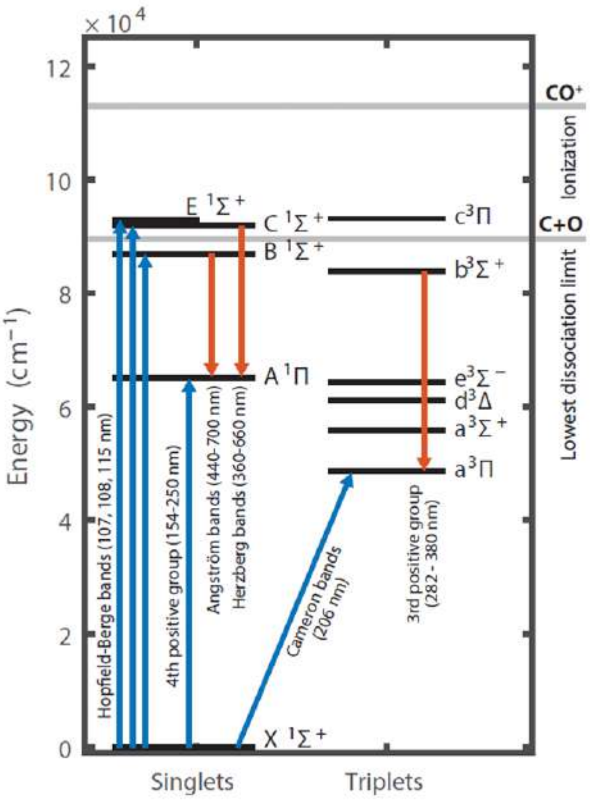

Figure 2.13: Schematic image of the energy levels in a CO TALIF measurement [39].

While some points advocate for choosing the $C^1\Sigma^+$ state, the $B^1\Sigma^+$ state has some other very good characteristics for TALIF:

- $B^1\Sigma^+$ lies below the dissociation limit, avoiding molecular destruction.
- Fluorescence of $B^1\Sigma^+$ also lies in the visible range, making detection straightforward.
- This state is well studied and characterised in literature, for example in [20, 50, 51].
- The collisional quenching rates with relevant species are known [45, 52]
- Additionally, the photoionisation rates are known [53].

For the stated reasons, the $B^1\Sigma^+$ is chosen as the excited state $|2\rangle$ in this thesis. In summary, in this thesis TALIF is used for the excitation spectra $B^1\Sigma^+(\nu' = 0) \leftarrow X^1\Sigma^+(\nu'' = 0)$. This also means, that the excitation occurs from the vibrational ground level of the electronic ground state to the vibrational ground level of the electronically excited state. The fluorescence is therefore detected from the $B^1\Sigma^+(\nu' = 0) \rightarrow A^1\Pi(\nu'' = 2)$ transition, laying in the range of 520 nm [54].

Characterising the $B^1\Sigma^+$ state, it is important to look at the natural lifetime of this state. The natural lifetime of the $B^1\Sigma^+$ state was intensively studied by Di Teodoro et al. [45]. It is strongly dependent on the pressure because of quenching. At low pressures of 1 mTorr, the natural lifetime is roughly 22 ns. If the pressure is increased to $\approx$ 200 mTorr, the lifetime increases up to roughly 65 ns. The explanation provided in [45] is that the opacity of the CO increases and with that, so called radiation trapping occurs, prolonging the lifetime. If the pressure is increased even more into the range of several Torr, the lifetime decreases again. This is because quenching starts to play a role. This behaviour is shown figure 2.14.
In case of this thesis, TALIF measurements were performed in various pressure regimes with an admixed bottle of 99 % Helium and 1 % CO and at 800 mbar as well as atmospheric pressure with CO_2.

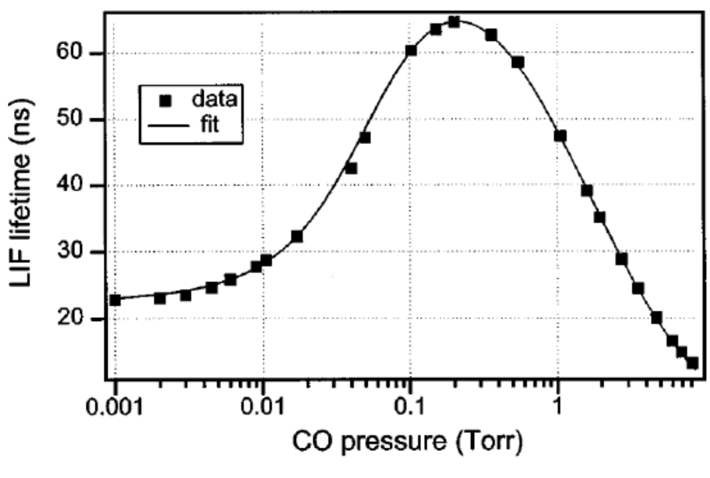

Figure 2.14: Illustrated is the lifetime of the fluorescence emitted by pure CO as a function of the CO pressure. The figure was taken from [45].

2.5.3 CO TALIF Spectra

Behind all this theory of TALIF, the result is always the same: one wants to obtain an excitation spectrum of the CO, on which the intensity of the different lines is plotted against the wavelength/wavenumber. The different intensities at each wavelength result from the different excited rotational levels of the CO. An example is shown in figure 2.15. In this example, two different spectra are shown for two temperatures: if the temperature changes compared to room temperature, the rotational levels of higher states get more populated, thus resulting in a stronger fluorescence signal at those wavenumbers.

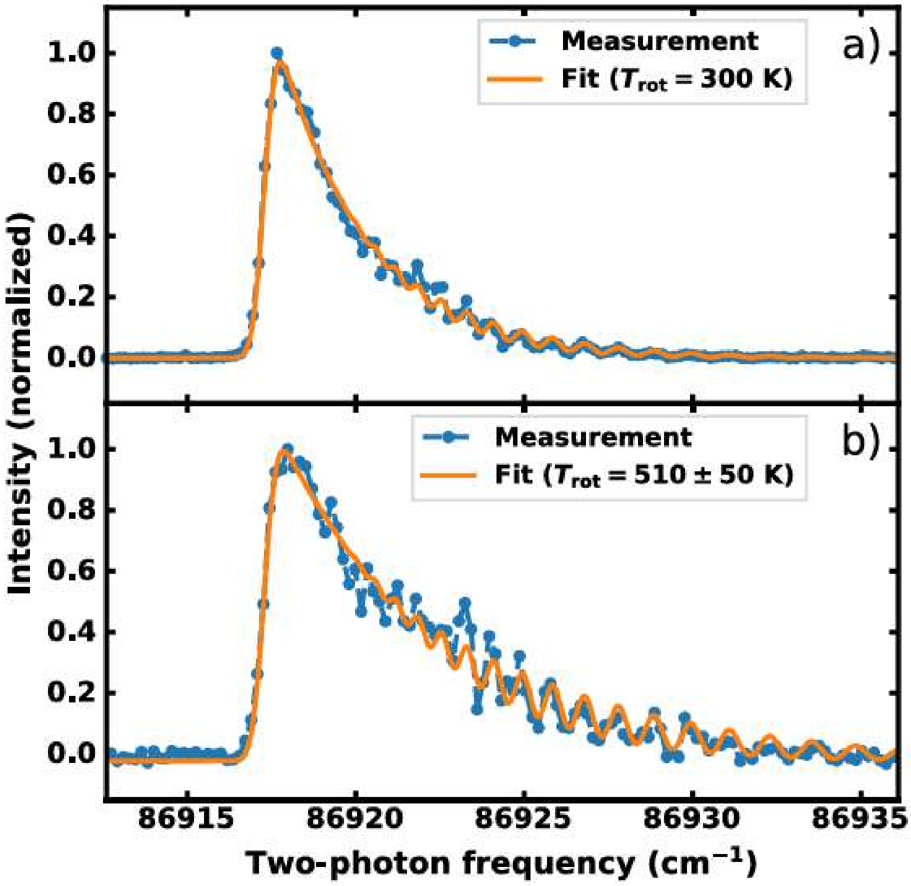

Figure 2.15: The image shows two CO TALIF spectra of $B^1\Sigma^+(\nu' = 0) \leftarrow X^1\Sigma^+(\nu'' = 0)$ excitation and fluorescence detection of the $B^1\Sigma^+(\nu' = 0) \rightarrow A^1\Pi(\nu'' = 2)$ transition, obtained by Damen et al. using TALIF at a) room temperature and b) during the cool down period of the plasma with simulated fits [20].

2.6 Calculation of the density

The calculation of the CO density N_{CO} is rather complex when the temperature of the CO is different to the reference case. In this thesis, it became clear that the temperature of the overall gas is not changed by the plasma, which makes calculation a lot simpler. The key equation is the following one, given by [20]:

$$N_{\mathrm{CO}} = \frac{Q + \tau_{nat}^{-1}}{Q_{\mathrm{ref}} + \tau_{nat}^{-1}} \cdot \frac{P_{\mathrm{ref}}^2}{\Gamma_{ref}} \cdot \frac{\Gamma}{P^2} \cdot N_{\mathrm{ref}} \tag{2.45}$$

Here, the Q_i stands for the quenching at measurement and reference conditions, τ_i is the natural lifetime at each condition, and both fractions containing P_i^2 and Γ_i represent the laser power and the measured signal. The last variable is the reference density N_{ref}, which is calculated with the ideal gas law as follows:

$$p = nk_{\mathrm{B}}T \Leftrightarrow \frac{p}{k_{\mathrm{B}}T} = N_{\mathrm{ref}} \tag{2.46}$$

In the case of the flowing mode of the plasma, atmospheric pressure is assumed. Equation 2.45 can also be written as:

$$N_{\mathrm{CO}} = \frac{a_{ik,\mathrm{ref}}}{a_{ik}} \cdot \frac{P_{\mathrm{ref}}^2}{\Gamma_{\mathrm{ref}}} \cdot \frac{\Gamma}{P^2} \cdot N_{\mathrm{ref}} \tag{2.47}$$

3 Experimental Setup and Diagnostics

This chapter describes all the diagnostics used in this work. For a better comprehensibility, it is divided into different sections. The central setup is the laser setup, which will be described first.

3.1 Laser setup

In the following, the laser setup will be described, as for the needed wavelength scans, some precautions have to be taken. An overview of the setup is shown in figure 3.1. The wavelength needs to be adjustable between 229.99 nm to 230.33 nm, so over a range of 34 pm.
For that, a Nd:YAG laser (Continuum: Powerlite 8000) is used, which emits pulsed light of wavelength 1064 nm. It is triggered by a pulse-delay-generator with a frequency of 10 Hz (Stanford Research Systems DG535). The Nd:YAG laser beam is then directed into a frequency doubling crystal, making it 532 nm.

In the next step, a dye laser (Continuum: ND6000) is pumped with the beam. For the pumping, a mixture of pyridin and DCM is used. The dye laser can emit wavelengths ranging from 650 nm to 715 nm. For the wavelength selection, a variable grating (Dual 2400 1/mm) is used, which can be controlled by a step-motor and select wavelengths in 1 pm steps. In order to achieve a wavelength of 230 nm, the selected wavelength is around 690 nm and the frequency is tripled using non-linear frequency mixing in crystals.

The first step after the dye laser, is the frequency doubling by a potassium dihydrogen-phosphate crystal (KDP). The laser beam then consists of the original wavelength and the frequency doubled wavelength, so 345 nm. This beam then goes into a beta-barium-borate crystal (BBO), the unchanged and doubled frequency are superimposed and the so-called third harmonic is created. The laser beam then consists of three different frequencies, of which two frequencies are undesired. In order to filter out the undesired frequencies, a Pellin-Broca prism is used. It directs the undesired frequencies into beam dumps.

For a good and evenly distributed laser profile, the orientation of the crystals is essential. In the crystals, the wavelengths of the photons are superimposed by rotation of the crystals. After alignment of the crystals, the laser profile is evenly distributed. Both the second harmonic generator (SHG) crystal and third harmonic generator (THG) crystal can be adjusted with Continuum devices. The beam is then directed by a mirror, going through a reflective neutral density filter (Thorlabs: ND02A) into a beam splitter. The neutral density filter must be used to ensure that the laser energy is not so high that the CO signal is later in the saturated regime of fluorescence. For measurements with varying laser energy, also the delay of the amplifier to the Nd:YAG laser was changed, which can be set also with a continuum device.

One part of the beam then goes through a quartz glass diffuser onto the photodiode, which is used for triggering of the oscilloscope and for normalisation of the fluorescence signal. The diffuser before the diode is used for two different reasons: first, it weakens the laser beam so

that the photodiode is not damaged or saturated. Second, the diffuser is homogenising the profile of the laser beam, so that the photodiode is registering an averaged intensity.
The other part of the beam is then directed by a mirror onto a lense (f = 30 cm, made out of Suprasil). The beam enters then the chamber through a window and has its focal point in the centre of the chamber. There the beam diameter is roughly 200 µm. Here, the MCPA is positioned on a height-variable stage (Zaber X-VSR40A-SV1). The laser beam passes over the MCPA, out of the chamber into a beam dump. The MCPA is described in the next section.

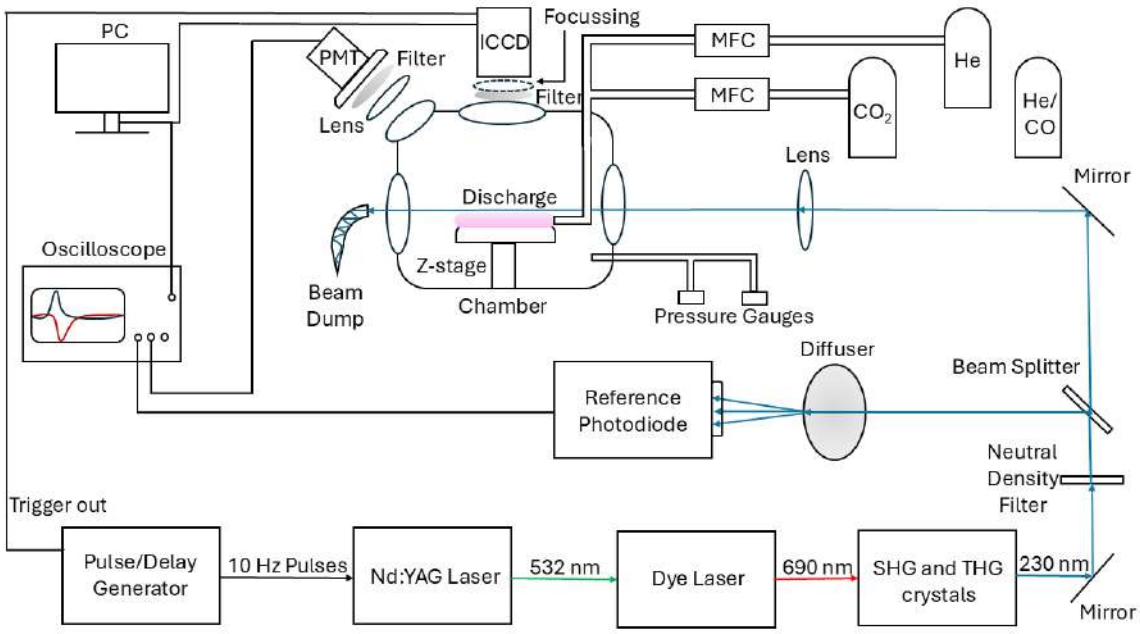

Figure 3.1: Schematic image of the used setup in this thesis, based on [55]. The CO_2 bottle can be swapped for a He and CO admixture bottle.

3.2 Micro-Cavities Plasma-Array

The plasma investigated in this thesis can be characterised as a dielectric barrier discharge. A schematic sketch of the array is shown in figure 3.2. It utilises a nickel foil as a grid, into which holes of 50 µm up to 200 µm are cut with a laser, coming from company Photonicfab. The construction is made as follows: a plastic mounting made out of polyether ether ketone (PEEK) holds a samarium-cobalt (Sm_2Co_{17}) magnet of the dimension 50 mm in length, 15 mm in width and 5 mm in height. A dielectric foil of 88 mm length, 27 mm in width and 40 µm made out of zirconia-dioxide (ZrO_2) is placed on the magnet. The ZrO_2-foil has a relative permittivity of $\epsilon_r \approx 20...30$ [56]. The dielectric is fixed to the setup by being clamped by magnetic force between the magnet and the nickel foil. The holes are then covered by one side, creating cavities.

The arrangement of the cavities is then called array. In this thesis, an array of the following dimensions is used: the cavity size is 200 µm, while the distance between cavities is varied in four squares: 50 µm, 100 µm, 150 µm and 200 µm, as shown in figure 3.2.

On top of the squares, a quartz glass cover can be attached. Then, the array can be operated in flowing mode. The quartz glass is needed, because normal glass would lead to absorption of the used laser wavelength, thus making measurements over the array with the cover attached impossible.

The array is powered using a function generator (Tektronix AFG 3012B) connected with a 50 Ω BNC-cable to an amplifier (Trek PZD700A M/S). The voltage is applied to the grid, while the magnet is used as the grounded electrode. The array is operated with a 15 kHz frequency with a triangular bipolar voltage shape. The set amplitude voltage at the function generator has then to be doubled (for peak-to-peak values of the voltage) and multiplied with 200, coming from the amplifier. For plasma operation in this thesis, Helium is used as the feed gas for ignition of the plasma. For the CO production, CO_2 is admixed in small quantities. The required voltage for ignition changes, depending on the admixture of CO_2, which makes ignition more difficult to happen and thus needs higher voltages, coming from Paschens-law and the energy that is put into the excitation of rotational and vibrational states of the CO_2. The next section covers the chamber and vacuum system, which is needed for operation of the plasma in both modes.

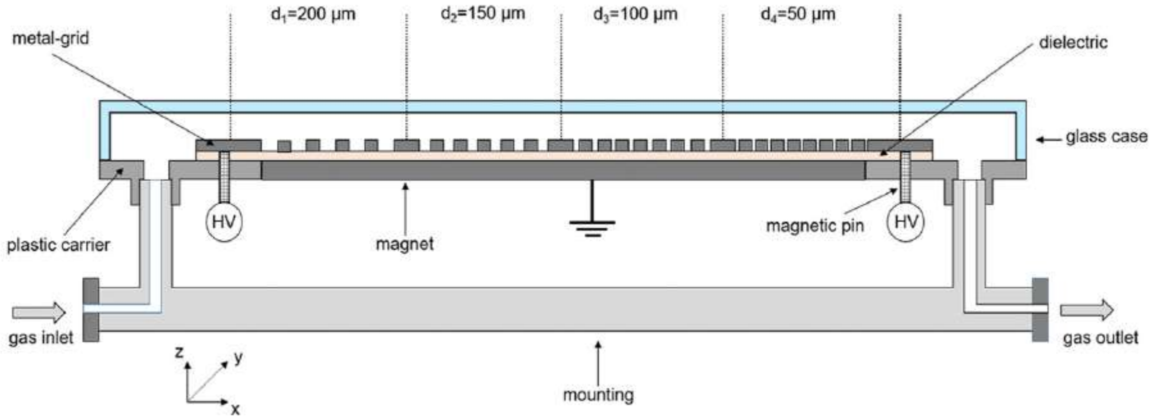

Figure 3.2: Schematic image of the MCPA, taken from [15].

3.3 Chamber and vacuum system

In this thesis, three different types of measurements were conducted. For calibration measurements, an atmosphere had to be used, where a defined amount of He and CO was put into a vacuum chamber. Also, the stationary case of a plasma ignited in a Helium and carbon dioxide atmosphere as well as operation of plasma in flowing mode, where the array gets confined by a quartz glass cover and the gas flows over the array, were performed. In this section, the chamber setup with the vacuum system is described.

For calibration measurements, no plasma was ignited, instead the chamber was filled with a gas mixture of 99 % helium and 1 % carbon monoxide (CO), already premixed in a gas bottle. To fill the chamber with the gas mixture, a pump system is needed. The first pump is a membrane pump (ABM-4EKF63CX), which is used going from 1 atm down to approximately 100 mbar. Then, a turbo molecular pump (Pfeiffer DCU 100) can be started. The turbo molecular pump can pump the chamber down to $9 \cdot 10^{-6}$ mbar. The pressure is measured using two different pressure gauges: one for the range of 1 mbar to 1 atm (vacuubrand DVR 5), the other pressure gauge for pressures below 1 mbar (Edwards Wide Range Gauge WRG-S 14.5-36V 2W), read out on a Edwards Active Gauge controller. It is essential for the measurements, to know the pressure inside the chamber.

For flow measurements, two mass flow controllers are used: 10 slm (or 10^4 sccm) and 100 sccm. The mass flow controllers of MKS are calibrated for molecular nitrogen, hence why there is a need for a gas correction factor (GCF), counting in the gauge factor, the temperature and conversion factor. The calculation of the gas correction factors is shown in the appendix A. The calculated values are shown in table 3.1. The SCF values are set at a MKS Flow Controller readout (MKS Type 247 Four Channel Flow Controller Power Supply and Readout). With this device, the gas flows can be controlled. If the values would not be set correctly, the gas admixture would be unknown, and with that, the conversion rates would be undefined.

In the next section, the two different detection systems of the fluorescence from the CO are described.

Table 3.1: Values of the GCF.

Gas	GCF Value
He	155.5
CO_2	75.1
99 % He and 1 % CO mixture	153.3

3.4 Detection Systems

For analysing the TALIF signal coming from either the carbon monoxide from calibration or the plasma itself, two different detectors are used in this thesis. The first measurements were done using a photomultiplier, while later measurements have been done using an intensified charge-coupled device (ICCD) camera. With the PMT, it was possible to scan over the whole excitation spectrum of the CO, and being able to extract the rotational temperature. With the ICCD camera, it was possible to measure the fluorescence of the CO in gas flowing operation of the plasma. Due to the added quartz glass cover, the PMT could not be used in those measurements. On the other side, it was deemed impractical to use the ICCD camera for a scan of the excitation spectrum, as one measurement point of the wavelength would have taken ≈ 10 min instead of ≈ 30 s, prolonging the measurement by a factor of 20. The setup for both detectors is discussed in the next sections.

3.4.1 Photomultiplier

A photomultiplier (Burle: C31034A) is mounted at a 45° angle to the surface against the beam direction. This angle comes from the setup of the chamber. Directly ahead of the photomultiplier, a filter (center wavelength (520 ± 10) nm) is placed to only let light of the desired transition $B^1\Sigma^+(\nu' = 0) \rightarrow A^1\Pi(\nu'' = 2)$ from the CO enter into the PMT. A lens (f = 30 cm) is placed after the filter. This optical path is shielded from ambient light to minimise background signal. The acceleration voltage of the PMT is usually set at 1.5 kV in this thesis, otherwise it is mentioned specifically. The triggering of the gate of the PMT comes from the same pulse-delay-generator that triggers the laser system. The values at the pulse-delay-generator are shown in table 3.2. It is really important, that the triggering is coordinated with each other, otherwise it would not be possible to detect the fluorescence.

The signal then goes into the oscilloscope (Teledyne Lecroy WavePro HD), where then the waveform is sent to the computer and analysed with a LabVIEW program.

For the later normalisation of the TALIF signal, the signal of the photodiode has to be saved, because the laser energy varies from shot to shot and goes quadratically into the calculation of the density, as in equation 2.43. This is also done with the LabVIEW program.

Table 3.2: Delay values set at the pulse-delay-generator. The photomultiplier delay is smaller than the delay for the laser, as the gating of it needs some time.

Delay set for	Delay value / µs
Laser	250.03
Photomultiplier	246.4
ICCD	250.49

3.4.2 ICCD Camera

For measurements in gas flowing operation of the plasma and taking 2D images of the CO density, a camera (Andor iStar ICCD-06083) is placed at a right angle against the laser beam path in the horizontal plane, focused onto the surface of the discharge array. Here, also a filter of the same bandwidth and centre wavelength is used to only detect the desired signal. The readout is done with a software provided by the company.

Before the measurement, a background without the laser beam is taken. A substantial problem for the measurements in flowing mode is stray light due to the quartz glass cover for the array. To at least mitigate the stray light, a 3D-printed cover is put on top of the glass cover, only leaving room for the laser beam to pass through the glass cover and one side open for the ICCD images. The triggering of the camera comes also from the pulse-delay-generator. For the focussing of the camera, an objective is used (Nikon ED AF MICRO NIKKOR 200mm 1:4D).

With the PMT and ICCD introduced, the next section covers the treatment and analysis of the data, as well as the simulation of theoretical spectra, which are needed for the determination of the rotational temperature in order to calculate absolute CO densities.

3.5 Data analysis

Some steps have to be taken to make a profound analysis of the measured signals, especially for the wavelength scans using the photomultiplier to determine the temperature of the CO. For that, different scripts have been written which are described in the next sections.

3.5.1 Labview Analysis

To automate the lengthy wavelength scan measurements, which take more than two hours per spectrum, a LabVIEW program was implemented. The program integrates multiple controls of the setup:

- First, the program controls the laser, allowing adjustments to the wavelength and enabling automated scans across the entire spectrum.

- Second, it facilitates the adjustment of the crystals via an Arduino serial interface. This is needed to ensure the profile of the laser beam remains constant and the laser energy per pulse does not decrease.
- Third, the program is connected to the oscilloscope, enabling the direct calculation of the TALIF signal (PMT/PD^2).

The program also saves the measurement data, and thus makes the whole process of data acquisition with the photomultiplier fairly simple. For the PD signal, measurements showed that only the maximum of it is needed, in contrast to the PMT signal, which is integrated in time. A comparable program connected to the ICCD camera was not written, but would be a step for future measurements. In the next subsection, the simulation of the theoretical excitation spectra is described.

3.5.2 Simulating a spectrum

In order to determine the rotational temperature and number densities, a simulation of the excitation spectra is needed for comparison. This section covers the theory behind the simulation.

The first thing the simulation program does is account for a wavelength shift, because the laser setup might not show the true outgoing wavelength. Reasons for this could be the optical setup, where a shift could be induced for example by a wrong calibration of the laser grid or temperature effects. The wavelength offset can not be measured with a wavemeter, because it is typically below $5\,\text{cm}^{-1}$, which would require a resolution of single wave numbers. It is more practical to simply shift the measured spectra because, with the known values from the literature, it is a fairly accurate method to determine the true wavelengths.

In the next step, the energy of CO of the electronic ground state $X^1\Sigma^+$ in the vibrational ground state $\nu = 0$, F_X, has to be calculated. This can be done using the following equation, coming from [57]:

$$F_X(J) = B_X \cdot J(J+1) + D_X \cdot J^2(J+1)^2 \tag{3.1}$$

In this equation, J is the rotational quantum number, B_X is the so-called rotational constant of the electronic ground state in the vibrational ground state $X^1\Sigma^+$ $\nu = 0$, and D_X is the centrifugal distortion constant [57]. For the electronically excited state $B^1\Sigma^+$ in the vibrational ground state $\nu = 0$, the energy F_B can be calculated equivalently:

$$F_B(J) = E_B + B_B \cdot J(J+1) + D_B \cdot J^2(J+1)^2 \tag{3.2}$$

Here, B_B and D_B are the rotational constant and the centrifugal distortion constant for the $B^1\Sigma^+$ $\nu = 0$, respectively. The E_B is the energy difference between the $X^1\Sigma^+$ and $B^1\Sigma^+$ states. The values for all constants can be found in table 3.3.

With those two equations, one can now calculate the energy difference between the two electronic states in the same rotational state, so with the same quantum number J:

$$E_{B\leftarrow X}(J) = F_B(J) - F_X(J) \tag{3.3}$$

The difference between these is equal to the energy of the transition between the two electronic states $E_{B\leftarrow X}$. With these equations, the wavenumbers needed for excitation for all rotational states can be calculated. But for creating a spectrum, also the intensity of each rotational transition as well as the broadening of the lines have to be taken into account.

Table 3.3: Overview of the constants used in the simulation.

Constant	Value	Source
E_B	$86917.8\,\mathrm{cm}^{-1}$	[57]
B_X	1.922521	[58]
D_X	$6.1193 \cdot 10^{-6}$	[58]
B_B	1.9475	[58]
D_B	$6.1 \cdot 10^{-6}$	[58]

The intensity of the rotational transition is dependent on the population of the lower state: when there is a low population, the intensity will be lower, as not much light can be emitted. The relative rotational state population $N_J(J)$ for a rotational quantum number J can be calculated using

$$N_J(J) = (2J+1) \cdot \exp\left(\frac{-F_X}{k_B T}\right) \tag{3.4}$$

This equation is simply the multiplication of the rotational degeneracy and the Boltzmann factor.

The Hönl-London factors, determining the line strength of the rotational transitions, are all equal to 1 according to Di Rosa et al. [52], which comes from the degeneracy of the ground state, as seen in equation 2.12. With this, the theoretical excitation spectrum is calculated. However, the spectrum is in nature broadened due to different effects.

Because of this, in the next step, the broadening mechanics of the line profiles are calculated. The pressure broadening $\Delta\omega_{Pressure}$ is calculated according to [51] with this equation:

$$\Delta\omega_{Pressure} = p \cdot 0.74 \cdot \left(\frac{295}{T}\right)^{0.65} \tag{3.5}$$

Here, p is the pressure in atm and T is the temperature in Kelvin. The pressure broadening has a Lorentz profile. Also the Doppler broadening has to be calculated for all rotational states J:

$$\Delta\omega_{Doppler} = \frac{1}{\frac{1}{\lambda} \cdot \sqrt{\frac{8 k_{\mathrm{B}} T \ln(2)}{M_{\mathrm{CO}}}}} \tag{3.6}$$

Here, the λ is the wavelength, the factor k_{B} is the Boltzmann constant and M_{CO} is the atomic mass of CO. The Doppler broadening profile has a Gaussian profile.

Both profiles then have to be convoluted into a Voigt profile. In the next step, the theoretical spectrum can actually be calculated, which is just the convolution of the calculated rotational state population $N_J(J)$ and the Voigt profile for the specific transition. In the last step, the convolution of the obtained spectra with the laser profile, which is assumed to be a Gaussian, is performed, and the spectra are finally simulated.

This routine includes some assumptions. The first one is that the intensity of the transitions is dependent on the line strength which do not have to be the same. The difference between the intensity and the line strength is, that the line strength does not depend on external conditions, while the intensity does. In other words, line strength describes how strong the transition can be, and intensity describes how strong it actually appears in the spectrum.

However, according to Di Rosa et al. [52], the line strength is equal to one for all rotational levels. This means, that there is no difference in intensity in the theoretical spectra between different rotational transitions. The second assumption is that the pressure shift can be neglected according to [51].

With this, the foundation for the measurement is layed. In the next chapter, preliminary measurements are presented, in order to characterise the setup sufficiently for the measurement of absolute CO densities.

4 Preliminary Measurements

This chapter presents the preliminary results of this master's thesis, detailing how a functioning TALIF setup was achieved and what intermediate measurements and checks were necessary. This measurements were necessary in order to ensure reproducibility and reliable results. The first section covers a comparison between two different filters, which are placed before the photomultiplier (PMT) and ICCD camera. The motivation behind is, that the measurements with both detectors can be done simultaneously, or at least the setup of the optical paths is then fixed.

4.1 Filter comparison

Two different filters were used in the setup to enable simultaneous operation of both detection systems. The filters are needed to ensure a better quality of the signal, filtering out ambient light and stray light. To compare them, the filters were placed in front of a broadband lamp, and an ICCD camera was used as the detector. The results are shown in figure 4.1. It can be observed that the transmission bandwidth of both filters is approximately the same. However, the central wavelength is slightly shifted to the left of the expected 520 nm centre. This shift was not considered problematic, as the bandpass remains sufficiently broad to detect the $B^1\Sigma^+(\nu' = 0) \rightarrow A^1\Pi(\nu'' = 2)$ fluorescence emitted by the CO.

Now that we have confirmed our ability to filter the fluorescence of the specific transition, the laser setup must be further investigated.

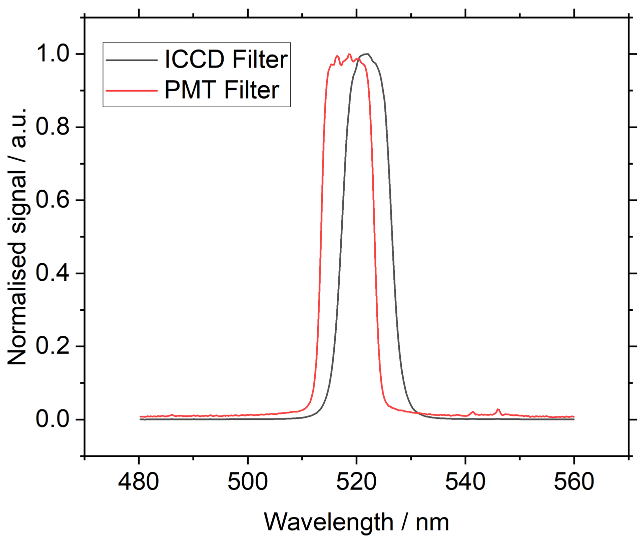

Figure 4.1: Comparison between the filters used for the PMT and for the ICCD in wavelength.

4.2 Characterisation of the laser

In this section, the characteristics of the laser are analysed. Understanding the laser's behaviour, especially the laser energy in time, is crucial for interpreting the measurement results. The first subsection focuses on the laser energy, one of its most important properties. This comes from the fact that, in contrast to TALIF on atomic oxygen, the measurement takes longer and scans over a whole spectrum, where as for O-TALIF, the wavelength is changed minimally.

4.2.1 Laser energy

Since a full wavelength scan of the CO excitation spectrum, with a reasonable number of averages, takes over an hour, it is important to determine whether the laser energy remains stable over long periods. The range of the wavelength before frequency doubling and tripling is 689.80 nm to 690.12 nm, and the steps are usually 2 pm. Before analysing the outgoing beam, the energy of the Nd:YAG laser was measured. The measured wavelength is 532 nm.

To do this, a piezoelectric detector (or energy measurement diode) with 21.6 V/J was placed in the beam path behind a beam splitter to prevent damage on the detector. The beam splitter damped the laser energy down to 4 %, therefore the obtained energy values had to be multiplied by 25. The piezoelectric detector was then connected to an oscilloscope. Both single laser shots, to check for outliers or trends, and averages of 100 shots were recorded over the course of one hour. The results for the averaged laser energy over 100 shots are shown in figure 4.2. The data indicates that the laser remains highly stable over time, with an energy level of approximately 320 mJ and a standard deviation of only ±8 mJ. This finding is further confirmed by figure 4.3, which displays individual laser shots at each time step. Aside from a minor outlier at the 30-minute mark, the single-shot measurements also appear highly stable, with standard deviations for each point in time ranging from ±4 mJ up to ±11 mJ. This confirms that the laser maintains stability at this stage of the experiment.

Next, the outgoing beam of the dye laser was examined with a piezoelectric detector of 541 V/J. The wavelength was fixed at 690.080 nm, before frequency doubling and tripling, where the maximum fluorescence signal of CO was observed. To minimize thermal effects, the laser was warmed up for several hours prior to measurement. At each time step, both 100-shot averages and 10-single-shot measurements were recorded. The results are presented in figures 4.4 and 4.5, respectively.

In contrast to the Nd:YAG laser energy measurements, a decreasing trend was observed. The average laser energy gradually declined from approximately 325 µJ to 260 µJ. This poses a potential issue for the setup: without compensation, this energy drift could introduce significant measurement errors, affecting later data analysis. However, it is important to note that during this measurement, no crystal adjustments were made after the initial setup. The observed energy decline could be attributed to thermal effects, not necessarily from the laser itself, but due to ambient temperature fluctuations. This might be for example the position of the crystals, or a distortion of the optics. The position of the crystals definitely plays a role, as the laser profile changed over time. Therefore, the laser profile must be kept constant, so crystal adjustion is needed.

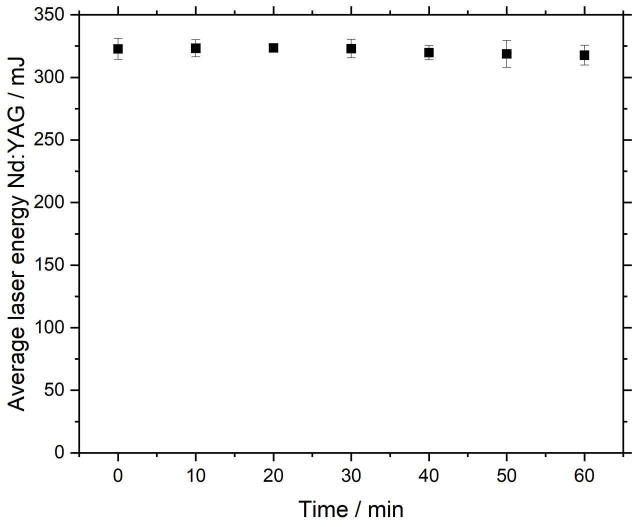

Figure 4.2: Averaged laser energy of the Nd:YAG, measured at a wavelength of 532 nm.

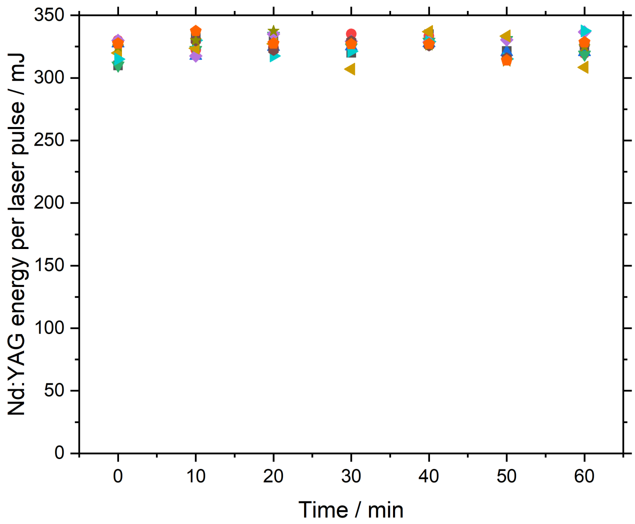

Figure 4.3: Ten single shots at each time step show the stable energy of the Nd:YAG, measured at a wavelength of 532 nm.

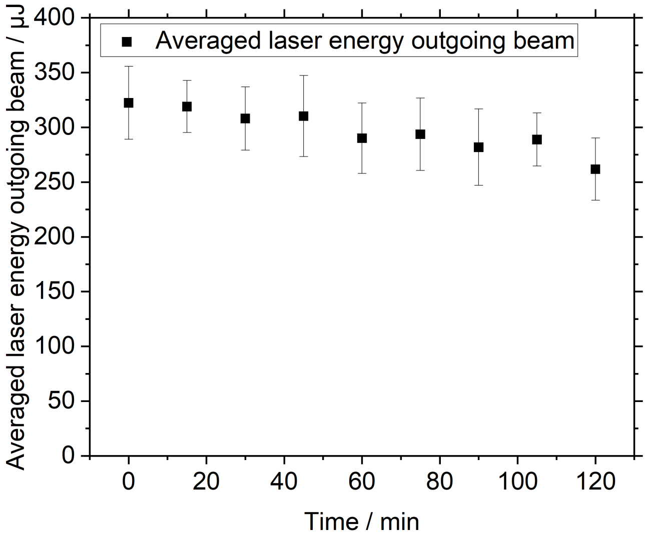

Figure 4.4: Averaged laser energy of the outgoing dye laser beam, measured at a set wavelength of 690.080 nm and after frequency tripled 230.03 nm.

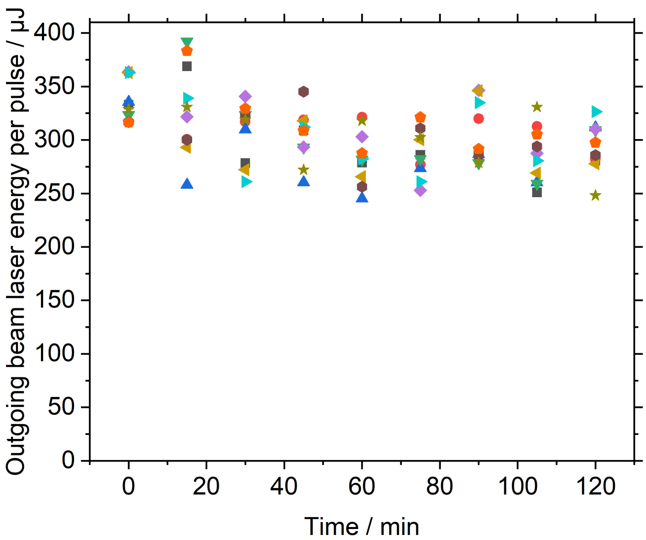

Figure 4.5: Ten single shots at each time step show the stable energy of the outgoing dye laser beam at a set wavelength of 690.080 nm and after frequency tripling 230.03 nm.

Thus, for future measurements, it is essential to monitor the diode signal continuously and make the necessary adjustments using the SHG and THG crystals. This trend is also evident in figure 4.5, where individual laser shots are plotted. Notably, at the first measurement point (0 min), the spread in laser energy is smaller compared to the later time points. The decreasing trend in laser energy is once again confirmed, and the same explanations apply as in the averaged case.

In summary, it is crucial to adjust the crystal positions when performing long-duration measurements (over one hour) with this laser system. The next section explores another key characteristic of the laser, which is particularly important for later analysis, as shown in the theoretical background 2.3.2: the polarisation of the light.

4.2.2 Polarisation

In the later analysis of the excitation spectra, certain assumptions must be made to simplify calculations. One key assumption is that the laser light responsible for exciting the CO molecules is linearly polarised. This can be easily verified in the current setup by placing a single polarisation filter into the dye laser beam before the reference photodiode. The laser wavelength is 230.03 nm.

This measurement is shown in figure 4.6. The wavelength was set at 230.03 nm. The highest voltage from the diode is observed at approximately 90°, and the measurement follows a $\cos^2(\theta)$ pattern, in accordance to Malus' law. This confirms that the laser light is indeed linearly polarised, in accordance with the assumptions made in the theory section, especially in the calculation of the Hönl-London factors 2.3.2. With that, the laser setup is investigated sufficiently and the focus can now lay on the laser profile and the best method to obtain a good and evenly distributed laser profile in space. This is crucial, as a badly distributed laser profile changes the measured fluorescence drastically. In the next section, the behaviour of the SHG and THG crystals is investigated to obtain the best possible laser profile in space.

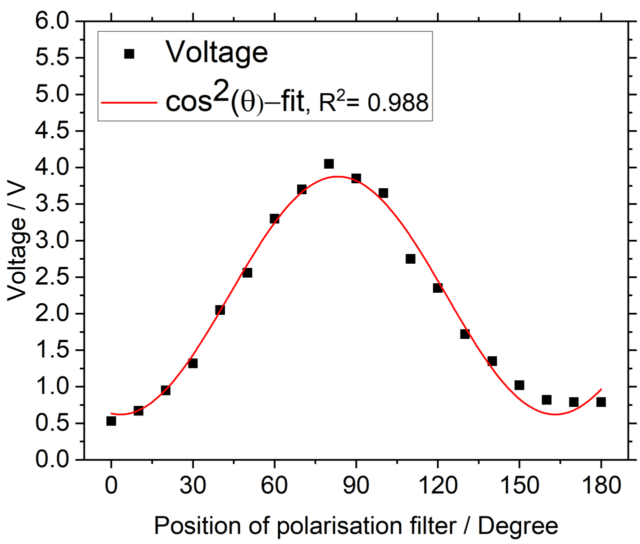

Figure 4.6: Investigation of the laser light polarisation.

4.2.3 Adjustion of the Crystals

Proper alignment of both the second harmonic generator (SHG) and third harmonic generator (THG) crystals is essential for achieving high energy density in the laser beam and comparable laser profiles. This results in a stronger reference photodiode signal and, most importantly, greater excitation of CO molecules, leading to a better overall fluorescence signal.

The two crystals can be adjusted using devices from the same manufacturer as the laser. Each device is equipped with two levers that allow the crystals to be rotated in either direction. However, the adjustment is not quantised, pulling the lever for a longer time causes the step motor to continue turning, entering a "fast mode" after approximately two seconds. This lack of precise step control poses a reproducibility issue, as motor steps cannot be reliably replicated.

To address this, a LabVIEW control system was programmed using an Arduino. The step motor controllers apply voltage to initiate movement, and the duration of this voltage application depends on how long the lever is engaged. By programming the Arduino to apply a fixed time of voltage application for each step (550 ms for the SHG and 230 ms for the THG), the step duration remains consistent, improving reproducibility. These durations were determined based on experience with the setup: adjustments to the SHG require larger movements than those for the THG to observe changes in the diode signal or laser profile.

While this method ensures consistent step sizes, absolute positional reproducibility remains unattainable, as the optimal crystal positions must still be manually determined before each measurement. The wavelength scans are required to obtain the rotational temperature of the CO and at each position, the crystals therefore must be adjusted.
The wavelength scan procedure follows these steps:

- The optimal positions of both the SHG and THG at the starting wavelength (689.80 nm) are manually determined using the levers. This method is faster and more precise than using the Arduino, as it does not require reprogramming the step duration.
- In the next step, the positions of the crystals at higher wavelengths (in 10 pm steps up to 690.1 nm) are obtained using the Arduino. These positions are determined using the program, and not manually, as the reproducibility of it is essential. If it would be done manually, the positions for the automatic scan would have a great uncertainty.
- A key consideration in adjusting the crystals is gear slippage. When reversing direction, the absolute position may shift. To mitigate this, adjustments are made in only one direction. If an overshoot occurs, the crystal must be moved beyond the intended position before returning to restart the alignment process.

Following this procedure, the crystal positions shown in figure 4.7 were determined. The two measurement sessions were conducted several weeks apart, highlighting the necessity of periodic realignment. However, the overall trend remained consistent: in both measurements, the SHG and THG required adjustments in the same direction. Additionally, SHG adjustments were needed less frequently than THG adjustments, likely due to the longer set step duration for the SHG (more than twice that of the THG).

Despite this, the crystal positions do not exhibit a strict one-to-one correlation, in other words the SHG and THG do not require identical adjustments. In summary, the crystal positions must be checked periodically, particularly after extended downtime of the setup.

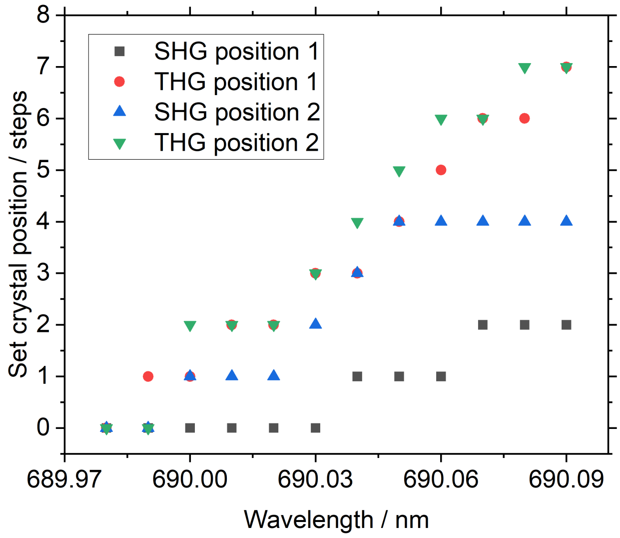

Figure 4.7: SHG and THG positions set in the LabVIEW program for two different measurements.

A challenge with crystal positioning is that adjustments can drastically alter the recorded signals for both the reference photodiode, photomultiplier and the ICC camera. This comes from the I^2-dependence as shown in equation 2.43. To mitigate this issue, several approaches were tested in this thesis, as discussed in the following.

Figure 4.8 illustrates crystal adjustments at different positions in the excitation spectrum of the CO, specifically at 689.98 nm, 690.02 nm and 690.06 nm. Those wavelength values correspond to the wavenumbers 86959 cm^{-1}, 86954 cm^{-1} and 86949 cm^{-1}, which will be used from now on in this thesis. These specific values have been chosen, as they are equally distributed over the range of the spectrum. The measurement was performed using an unknown concentration of CO, as beforehand, measurements with plasma were performed, which produced the CO.

One attempted approach to minimise the impact of adjustments was to modify the crystal positions only when the signal became too weak. However, this method led to an undesirable effect: the signal shifted from one measurement point with a very low intensity to another with a much higher intensity, creating artificial spikes in the spectrum, as clearly visible in figure 4.8. Due to these inconsistencies, this approach was deemed ineffective and ultimately abandoned.

Another approach involved making a single adjustment to the crystal position within a spectral region where only a low signal was expected. This method is demonstrated in figures 4.9 and 4.10. However, this approach also introduced complications. In figure 4.9, the crystals were adjusted at 86950 cm^{-1}, roughly in the middle of the spectrum. After the adjustment, the laser was reset to the starting wavelength to minimize grid slippage effects. The scan direction proceeded from lower to higher wavelengths, corresponding to a transition from higher to lower wavenumbers. As seen in figure 4.9, this resulted in a significant overestimation

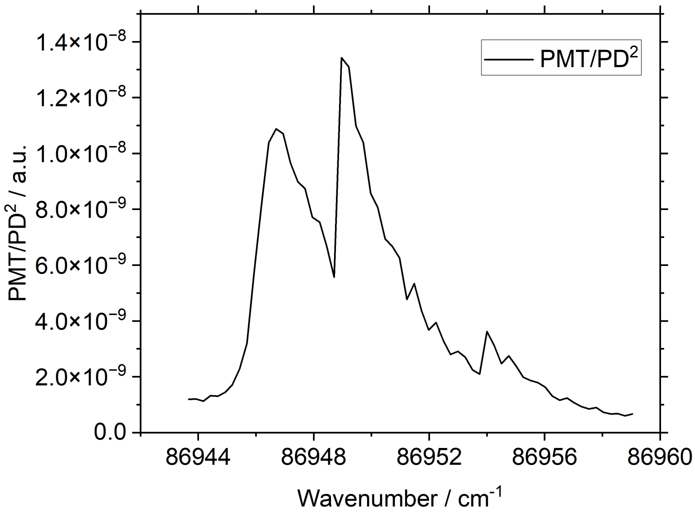

Figure 4.8: Crystal adjustment at $86959\,\mathrm{cm}^{-1}$, $86954\ \mathrm{cm}^{-1}$ and $86949\,\mathrm{cm}^{-1}$.

of the background signal in the high wavenumber range, reaching nearly half the total signal strength.

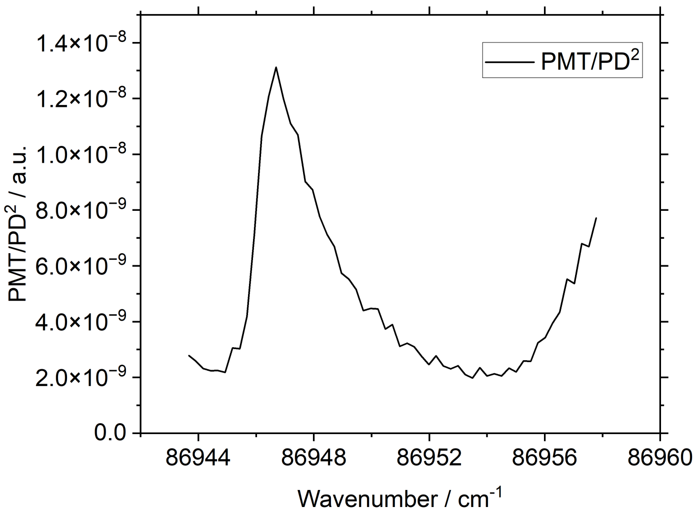

Figure 4.9: Crystal adjustment at $86950\,\mathrm{cm}^{-1}$.

In figure 4.10, the crystal adjustment was performed at $86954\,\mathrm{cm}^{-1}$, shifting it into the range of lower signal. While this approach improved the signal trend in the low-intensity region compared to figure 4.9, it again led to background overestimation at the lower wavenumber end. These signal fluctuations can be attributed to changes in the laser profile induced by crystal adjustments. A misaligned crystal setup, even by visual estimation, would compromise measurement accuracy.

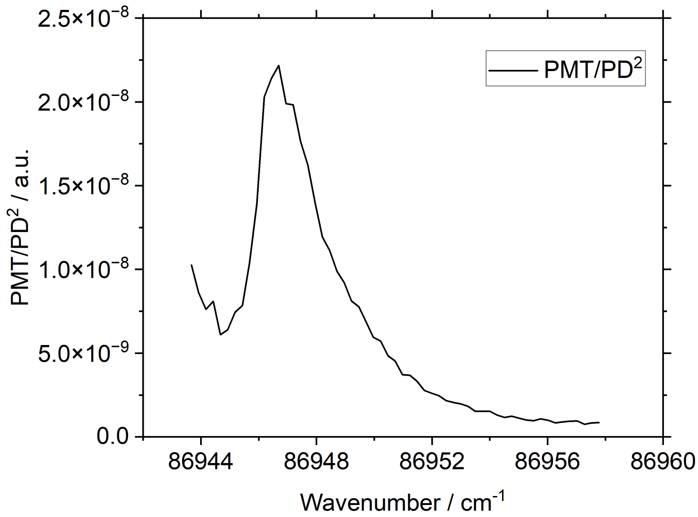

Figure 4.10: Crystal adjustment at 86954 cm^{-1}.

The solution to this issue is automating the crystal adjustment process. As outlined in section 4.2.3, the optimal crystal positions are pre-recorded in small increments (e.g., 10 pm or 2 cm^{-1}) before starting a measurement. These values are then integrated into the LabVIEW program, which automatically scans the selected wavelengths and adjusts the crystals at predefined positions. The outcome of this automated approach is shown in figure 4.11. A minor signal deviation remains visible at 86948 cm^{-1}, which can be due to the adjustment, or come from the CO itself. However, as later comparisons with simulations indicate, this does not interfere with the extraction of rotational temperature, confirming that the method provides a reasonably accurate solution.
In the next section, the automated crystal adjustment is applied in a measurement of the laser profile at different wavelengths, testing its reliability.

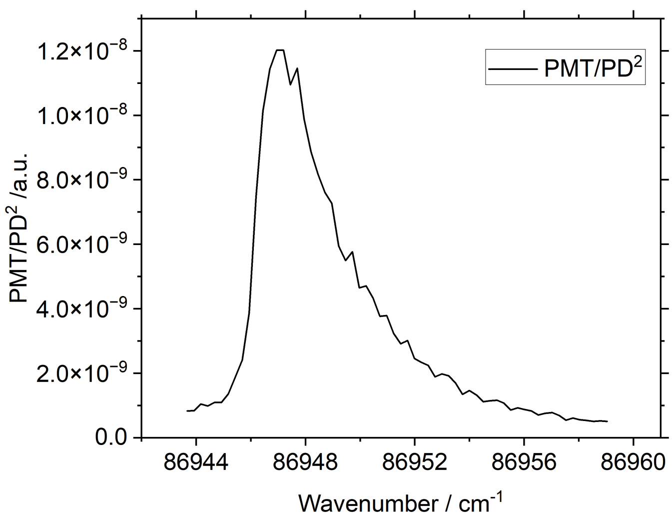

Figure 4.11: Automated crystal adjustment with adjustion in 2 cm^{-1} steps.

4.2.4 Laser profile

The laser profile was measured using a gentec-ϵo profiler (BSF23RS11.3N). The crystal positions were optimised based on the diode signal maximum at each wavelength. The profiler was placed behind the chamber, at the location of the beam dump. The results are shown in figure 4.12. As seen in figure 4.12, the laser profiles remain highly consistent, despite the wavelength

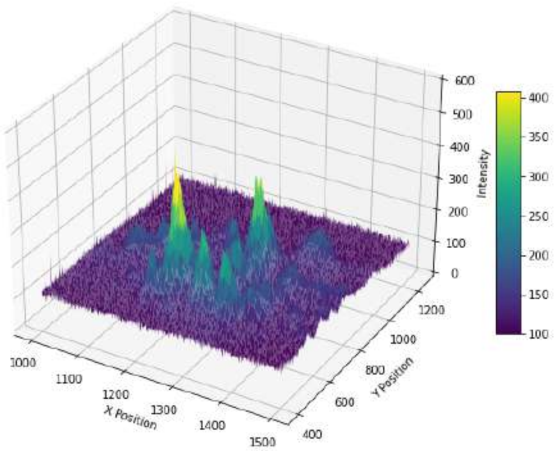

(a)

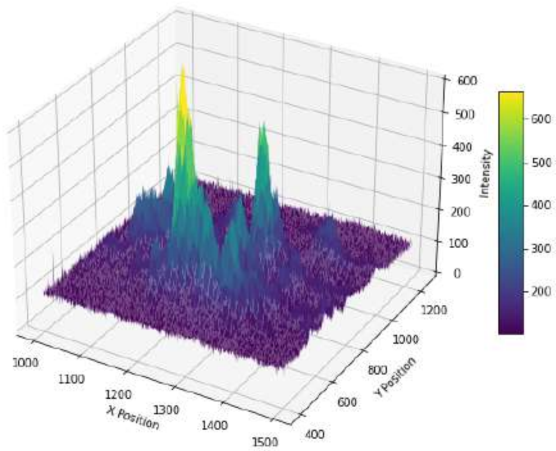

(b)

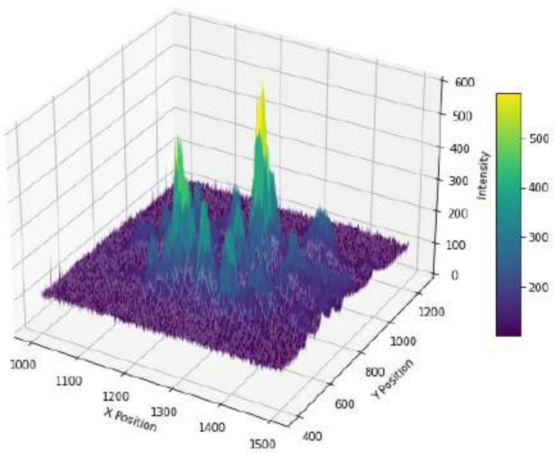

(c)

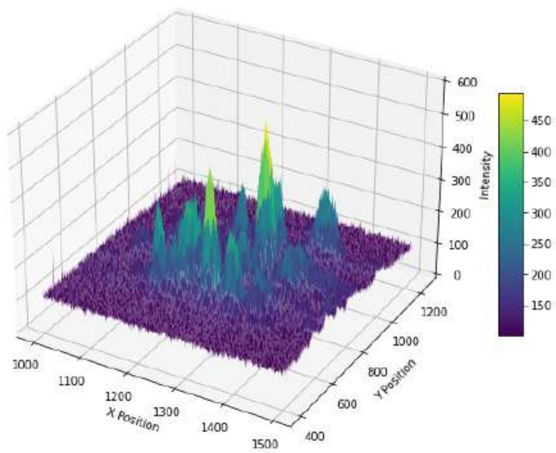

(d)

Figure 4.12: Measurements of the laser profile at different wavelengths: (a) 229.93 nm, (b) 230.01 nm, (c) 230.02 nm and (d) 230.04 nm.

variations across the measured CO spectrum. This level of consistency was only achieved through precise crystal adjustments at each wavelength position. Before optimisation, the laser profile was weak or even undetectable.

With this knowledge, the general setup has been verified and deemed suitable for conducting TALIF measurements with CO. The next section discusses the correct crystal alignment, which is essential for obtaining good results. The next section discusses additional precautions taken to ensure measurement reliability.

4.2.5 Remarks on analysis

When analysing the TALIF signal (PMT/PD^2), several precautions must be taken to ensure accuracy. The first consideration concerns the treatment of the reference photodiode signal.

For calculation of the absolute CO densities, the diode signal is used. However, the question arises as to which part of the diode signal should be utilised. The common approach is to integrate the signal over time. However, measurements conducted in this thesis indicate that there is no significant difference between using the integral of the diode signal and using its peak value.
Another important aspect of the analysis is how the TALIF signal (PMT/PD^2) averaging is performed. The TALIF signal averaging is needed, as single measurement points are subject to large fluctuations of up to 20 %. There are two possible approaches:

- Averaging the signals directly at the oscilloscope: This is a straightforward method, as modern oscilloscopes offer built-in averaging functions. Here, the average PMT signal is divided by the average reference photodiode signal.
- Division of each individual laser shot before averaging: In this approach, the PMT signal of each laser shot is divided by the square of the reference photodiode signal's maximum. This ensures that stronger and weaker signals are treated individually, reducing systematic errors. The averaging process is then applied afterward. The systematic errors can come from the various methods of averaging.

This second method has been implemented in the LabVIEW analysis program. An example of the recorded signals is shown in figure 4.13. The first and a second peak of the photodiode signal are clearly visible, along with a third peak. These two additional peaks likely originate from the photodiode's electrical circuitry rather than from a second or third laser pulse.

To summarise, the characteristics of analysis and the laser setup have been described. It is now possible, to investigate the behaviour of the photon energy behaviour, in order to verify the assumptions made in the theoretical background regarding the equations behind TALIF 2.42.

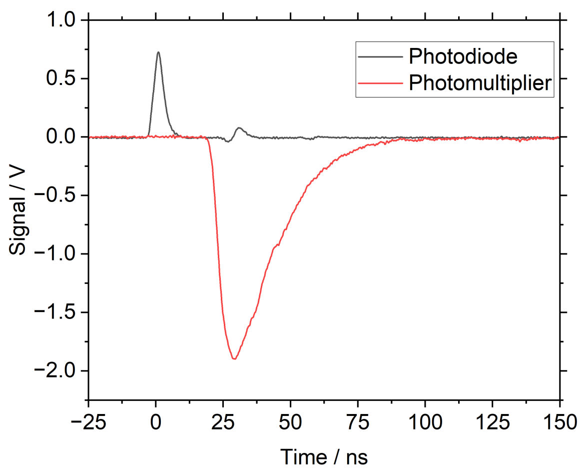

Figure 4.13: Photomultiplier and reference photodiode signal in time, averaged over 1000 laser shots, performed in 500 mbar of 99 % He and 1 % CO.

4.3 Laser Intensity Variation

In this section, we examine and verify our theoretical assumptions regarding the rate equations of TALIF. The rate equations 2.41 lead to an equation 2.42 which shows, that the fluorescence signal scales with the square of the laser intensity. This can be verified by varying the laser energy using neutral density (ND) grey-filters, manufactured by Thorlabs. In the rate equations, effects like photoionisation and stimulated emission are neglected. However, if the laser energy is too high, the signal may saturate. This would invalidate the model.

In the measurements, different ND grey-filters were put into the laser beam. To get more measurement points, even combinations of different ND grey-filters were put behind each other. The wavelength was fixed at maximum CO signal, and 200 averages of each configuration were taken. The chamber was filled with 1 atm of 99 % He and 1 % CO, while the photomultiplier voltage was kept constant at 1.3 kV. The plot is shown in figure 4.14. The linear trend is clearly visible for the lower PMT signals. For the higher signals, only a few measurement points could be obtained, due to the fact that the ND filters are very strong, thus combinations of them weaken the laser beam even more.

To counter this, additionally to the ND filter variation, the delay for the Nd:YAG amplifier was varied. This however also changes the laser profile, which makes the measurement inaccurate. The profile changes, because the change in the delay-amplifier changes the energy that is stored in the Nd:YAG crystal. Despite this limitation, the experiment was conducted to gain further insight. The results are shown in figure 4.15. An approximately linear trend is also visible for the lower values of PD^2. However, for the higher values after 0.6 V^2 of PD^2, the beginning of saturation can be interpreted from the data.

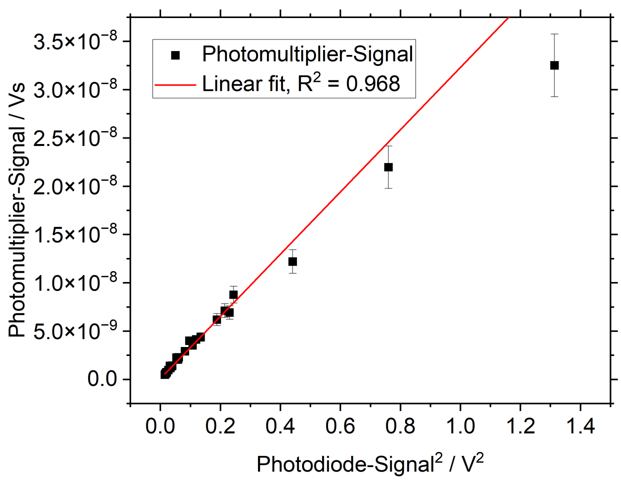

Figure 4.14: The ND grey-filter variation shows the PMT-signal plotted against the PD^2 at full Nd:YAG amplifier power.

The combination of both measurements is shown in figure 4.16. The measurements do not overlap perfectly, the amplifier-delay variation values are somewhat higher than the grey-filter variation. Nevertheless, those values are in each others error bars, which are calculated

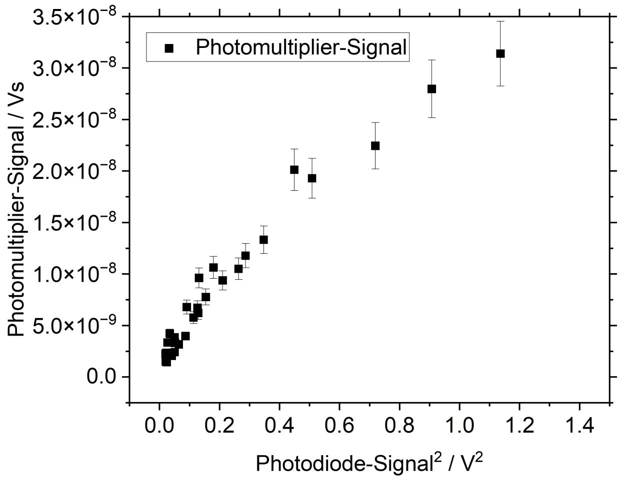

Figure 4.15: The amplifier-delay variation of the Nd:YAG without ND grey-filters shows the PMT-signal plotted against the PD^2.

according to section 4.5 and have a value of 10%. To ensure that future measurements remain within the linear regime and avoid excessive laser energy, an ND grey-filter with an optical density (OD) of 0.2 is used in future measurements. This corresponds to the third measurement point in figure 4.14, counted from the right side. This value lies in the upper limit of the supposed linear regime, resulting in the best possible signal-to-noise ratio without leaving the linear regime. The value of ND0.2 results in a transmission T of the signal given by:

$$OD = \log_{10}\left(\frac{1}{T}\right) \Leftrightarrow T = 10^{-OD} \approx 63\%. \tag{4.1}$$

The next section covers the behaviour of the signal at different pressures.

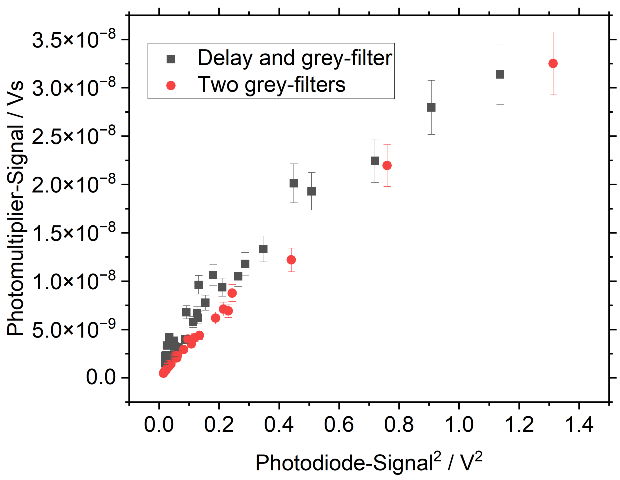

Figure 4.16: Both variations of amplifier-delay variation and grey-filter variation are shown here. To make sure future measurements are in the linear regime, a grey-filter of ND = 0.2 is used.

4.4 Pressure Variation

In this section, the pressure of 99 % He and 1 % CO in the chamber was varied to investigate quenching effects and verify whether the TALIF signal remains within the linear regime. Figure 4.17 presents example curves of the normalised PMT signal, averaged over 100 laser shots. The set wavenumber was at maximum signal, so at 86947 cm^{-1}. The curves do not overlap for different pressures, indicating that they exhibit different lifetimes according to equation 2.28.

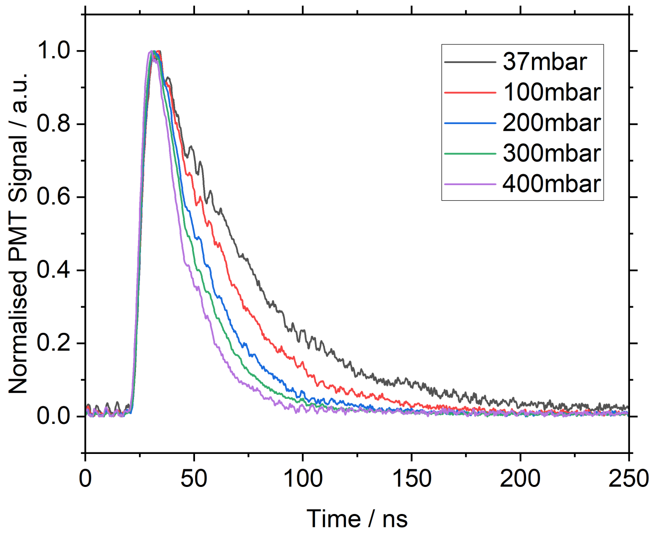

Figure 4.17: Normalised photomultiplier signals at different pressures.

By applying a simple fitting routine based on equation 2.28, the lifetime of the excited state can be determined for each pressure. An exponential decay fit with the following formula was applied:

$$y = y_0 + A \cdot e^{-x/\tau_{fit}} \tag{4.2}$$

to extract the fitted lifetime τ_{fit}. An example fit is shown in figure 4.18. As can be seen, the fit does not begin at the peak of the signal. The reason for this is that, at this point in time, the laser is still on and thus influencing the signal. The fit only starts after roughly 15 ns, where the laser beam should already be off for a few ns at least.

Additionally, the obtained lifetime can be compared to the theoretical value, calculated as follows: Using equation 2.30, the quenching frequency Q for different pressures can be determined:

$$\mathrm{Q} = (q_{He} f_{He} + q_{CO} f_{CO})\, p \tag{4.3}$$

Here, q_{He} and q_{CO} are the quenching rate coefficients, f_{He} and f_{CO} represent the respective gas fractions, and p denotes the total pressure. Now, only the literature values for the Einstein coefficients A_{21} and A_{23} have to be added to Q for each pressure to obtain the total decay rate q:

$$q = A_{21} + A_{23} + Q \tag{4.4}$$

with $A_{21} = 31$ MHz and $A_{23} = 13$ MHz [45]. The total decay rate q is given in MHz, to calculate the lifetime τ, the inverse has to be calculated according to $T = 1/q$. Using this approach, the

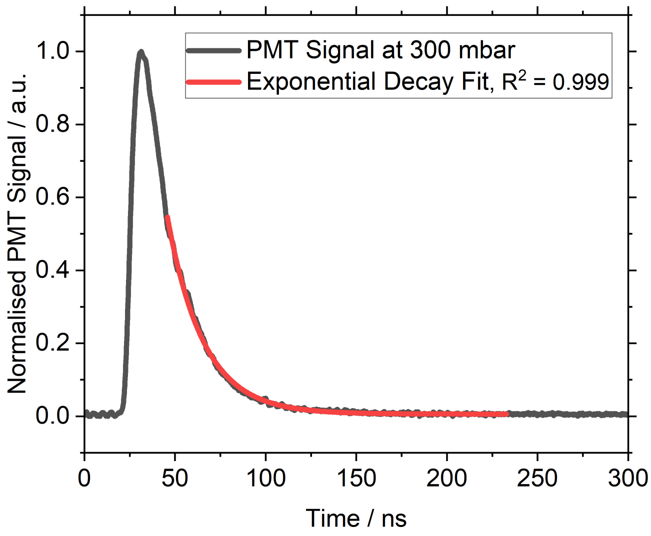

Figure 4.18: Normalised photomultiplier signal of 300 mbar measurement with exponential decay fit.

theoretical lifetimes are determined and compared to the experimentally measured lifetimes obtained from fitting the normalised signals. Figure 4.19 illustrates this comparison. The zero crossing of the theoretical lifetime gives the natural lifetime of 22 ns, as shown in figure 2.14.

A significant discrepancy between the measured and theoretical lifetimes is observed: the measured lifetimes are 50 % to 100 % longer than theoretically expected. This confirms the assumption made in the theoretical background (section 2.4.1) that the laser pulse duration τ_L is not sufficiently short in comparison to the effective lifetime τ_{eff} to measure it accurately. Due to this deviation, only the theoretical lifetimes will be used in subsequent analysis.

Next, the pressure variation is extended over a wider pressure range to verify that the quenching correction is properly accounted for. To achieve this, the obtained TALIF signal PMT/PD^2 is divided by the branching ratio:

$$a_{ik} = \frac{A_{ik}}{\sum_k A_{ik} + Q} \Rightarrow a_{21} = \frac{31\,\text{MHz}}{31\,\text{MHz} + 13\,\text{MHz} + Q} \tag{4.5}$$

using the same Q as in equation 4.3. The results are shown in figure 4.20. A linear trend is observed up to the highest measured pressure, indicating that quenching has been properly accounted for. If quenching had been incorrectly handled, it would have reduced the measured TALIF signal and disrupted the linear trend.

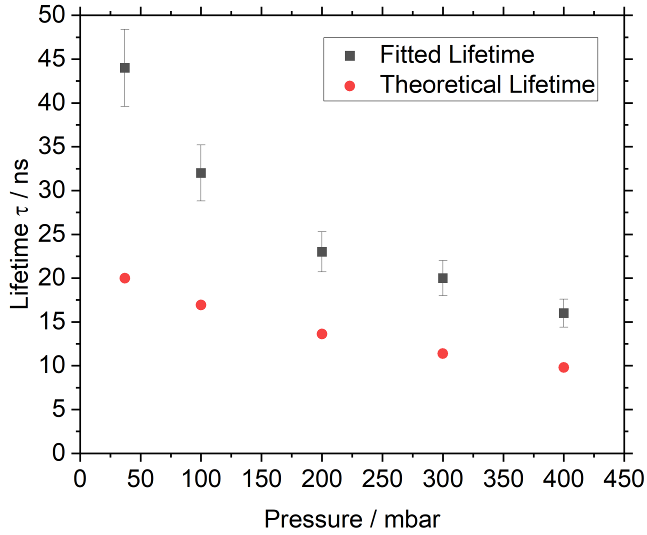

Figure 4.19: Comparison between theoretically calculated lifetimes and lifetimes obtained from fitting the measurement.

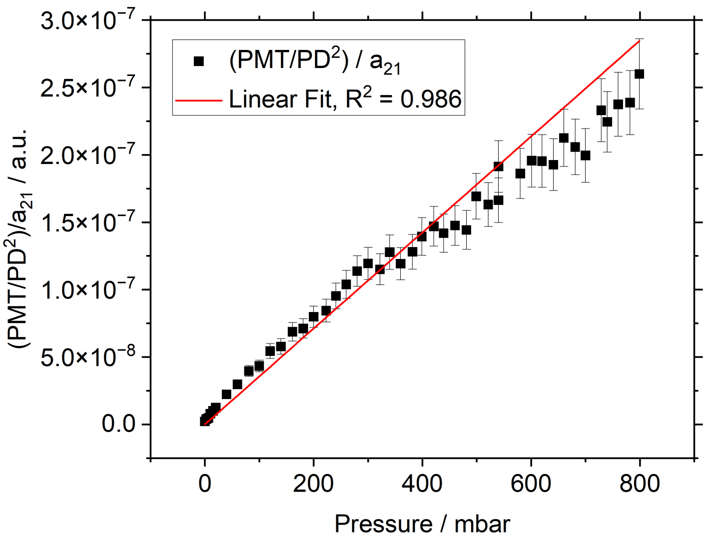

Figure 4.20: The TALIF signal (PMT/PD^2) divided by the branching ratio a_{21}.

4.5 Variation of Distance between MCPA and Laser Beam

In this section, the height of the MCPA is varied relative to the laser beam without the quartz glass cover. The MCPA was put into the chamber without a quartz glass cover. The plasma is not ignited during these measurements, as the purpose is to investigate potential reflection effects and to estimate the measurement uncertainty of the signal.

The height of the array was varied with a Z-stage. The scanning began with the height of the stage being set to z = 0 mm, and subsequently raised. The measurements were performed with 20 mbar of 99 % He and 1 % CO, and the set wavelength of the laser was 690.08 nm or 86946.4 cm^{-1}, at maximum signal. The results are shown in figure 4.21. For distances between 0 mm up to 8 mm, the signal should remain unchanged, as no interference from the array is expected. These measurements are therefore considered suitable for error estimation in future experiments. To quantify the uncertainty, only data points up from 0.5 mm are used, since measurements beyond this point may already be affected by reflections. The standard deviation calculated from these values is $\sigma_E = \pm 1.14 \cdot 10^{-7}$ a.u.. However, this standard deviation is valid only for the present measurement. A repeat experiment on a different day, focusing specifically on reflection effects, yielded different absolute values, as shown in figure 4.22. To account for day-to-day variations, a relative error calculation is performed. The average signal value measured is $2.23 \cdot 10^{-6}$ a.u., resulting in a relative deviation of ±5.1 %. Given the high sensitivity of TALIF measurements, this error is relatively small. Therefore, the error margin is doubled, leading to an assumed uncertainty of 10 % in future experiments.

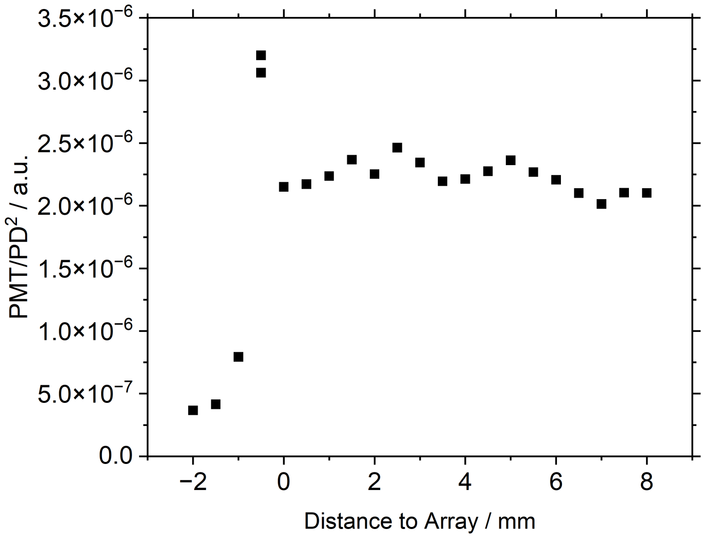

Figure 4.21: Distance variation of the array with no plasma, performed at 20 mbar of 99 % He and 1 % CO at 86946.4 cm^{-1}.

In figure 4.21, the moment when the laser beam hits the edge of the array is clearly visible, as stray light is reflected into the photomultiplier. When the distance is further decreased, the signal decreases rapidly, indicating that a portion of the laser beam is being blocked by the array, reducing the excitation of CO molecules. To investigate this effect in greater detail, a second measurement was performed with a finer distance resolution, focusing on the critical region, as shown in figure 4.22. This second measurement reveals the same abrupt transition compared to the initial experiment. A peak-like structure is now observed, which is again attributed to stray light reflections. The gradual signal decrease also aligns with the expectation that with each height increment, a fraction of the laser beam is obstructed by the array.

In summary, a reliable error estimation for future measurements has now been established. Additionally, the interaction between the MCPA and the laser beam has been characterised. In subsequent measurements, it is critical to ensure that the laser beam is positioned sufficiently high above the array to prevent signal distortion due to reflections.
With this section, the laser setup and its associated challenges have been analysed and addressed. The following sections will now focus on conversion experiments using plasma.

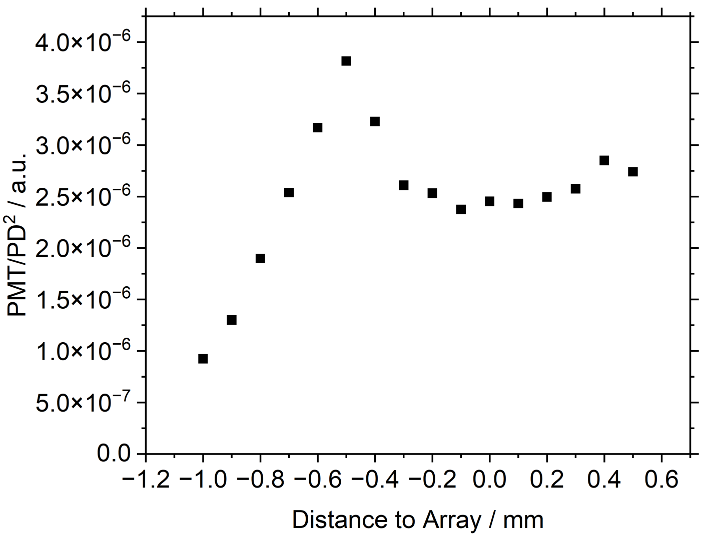

Figure 4.22: Height variation of the array with no plasma, performed at 20 mbar of 99 % He and 1 % CO at 86946.4 cm^{-1} and focussed on the area of reflections.

5 Stationary Plasma Experiments

This chapter presents the experimental results obtained from plasma operation in a stationary atmosphere. Unlike flowing mode operation, the plasma ignition in these experiments was not performed at atmospheric pressure, rather at pressures of 800 mbar of helium and roughly 8 mbar (or 1 %) of CO_2.

The motivation behind these measurements is the following: the setup is simpler in comparison to flowing mode, due to the fact that no quartz glass cover is needed. This also enables measurements with the PMT, particularly for obtaining the rotational temperature of the CO. Additionally, when the chamber is closed, high CO densities can be produced, because the CO is not flushed away.

5.1 Temporal Evolution of the TALIF Signal

The first experiment aimed to verify the CO production of the plasma by analysing the temporal evolution of the TALIF signal. For this purpose, the chamber was filled with 800 mbar of He and 5 mbar of CO_2 (which corresponds to an admixture of 0.6 %), ensuring that the stage height was sufficiently low to avoid potential reflections, but still as close as possible to the MCPA surface, so at $z = 0$ mm. The plasma was ignited using 600 V for the voltage amplitude at 15 kHz, and the laser wavelength was set to 86946.4 cm^{-1}, corresponding to the maximum signal.

Prior to plasma ignition, a background measurement was conducted with the gas mixture present but no plasma discharge. Each data point represents an average of 100 laser shots, and the background was subtracted.

The results are presented in figure 5.1. A clear linear increase in the TALIF signal over time is observed, indicating continuous CO production by the plasma. Even after the measurement was paused after 100 min, the increasing trend persisted. No saturation effects were detected within the observed time frame. This result confirms the CO production by the plasma, and therefore the investigation can go further.

The next section focuses on the estimation of rotational temperature, derived from the measured spectra, which is needed for calculation of absolute CO densities. As described in the theoretical background, a change in rotational temperature would require another analysis method 2.6.

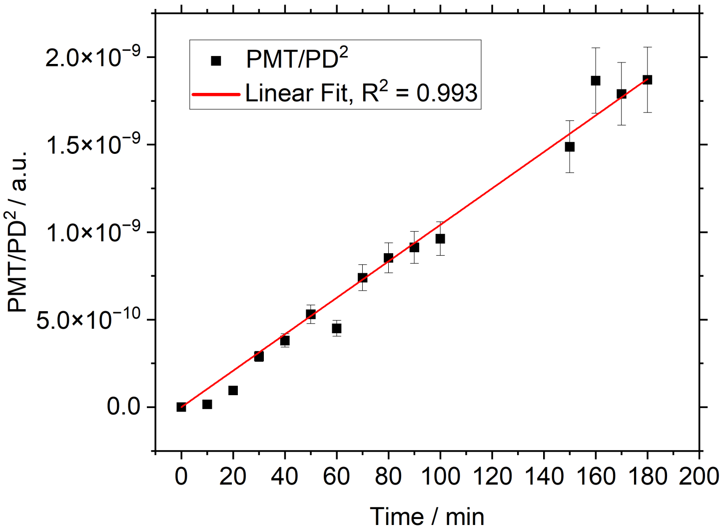

Figure 5.1: Measurement of plasma produced CO over time, performed at 800 mbar of He and 5 mbar of CO_2 at 86946.4 cm^{-1}. The plasma was ignited with 600 V at 15 kHz, and the stage height was at z = 0 mm, to avoid reflections.

5.2 Estimation of the Rotational Temperature

In this section, the rotational temperature of plasma-generated CO is investigated. The knowledge of the rotational temperature of the CO is essential for calculation of the absolute densities of CO, as the rotational temperature is directly linked to the population of different rotational states J. For this purpose, the chamber was filled with 795 mbar of He and 5 mbar of CO_2, corresponding to an admixture of 0.6 %. The plasma was ignited using a 15 kHz triangular frequency with an applied voltage amplitude of 700 V. The plasma was ignited for several hours, ensuring a sufficient concentration of CO in the chamber. The array surface was carefully positioned as close to the laser beam as possible without obstructing any portion of the beam.

A higher rotational temperature compared to room temperature is typically indicated by a stronger signal at higher rotational quantum numbers (J), particularly around 86923 cm^{-1} as shown in figure 2.15 b). However, in the present measurements, no such increase was observed. The signal remained relatively constant, as shown in 5.2 over a period of 4.5 h and 6 h. The fitting routine yielded the best results for a temperature of 290 K. This is a major result, as it shows, that the plasma does not significantly heat up the gas.

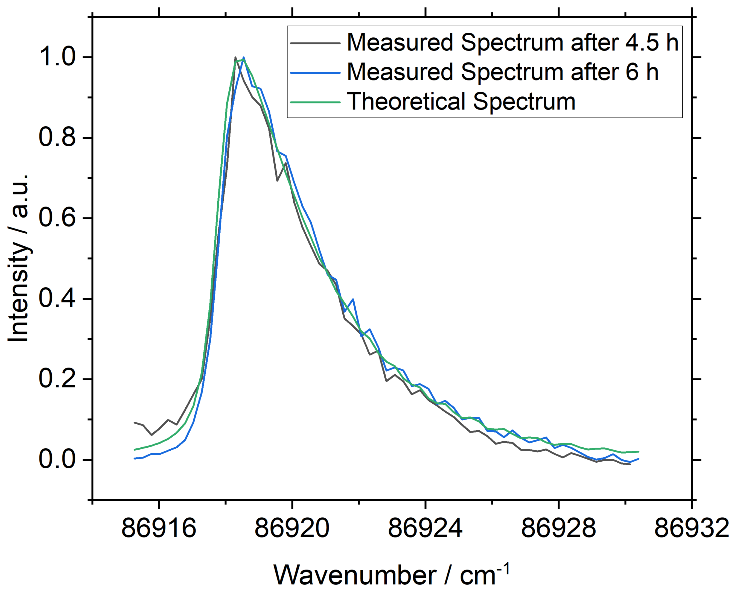

Figure 5.2: Measurement of a spectrum of plasma produced CO, after the plasma was running for 4.5 h (black) and 6 h (blue). The theoretical spectrum (green) was applied with a temperature of T = 290 K.

A comparison between the obtained experimental spectrum here and the theoretical one, especially in figure 2.15, yields an absolute difference of roughly 27 cm^{-1}. This shift can come from the optical pathway and reflections, and even a wavelength shift in the setting of the laser. They have been accounted for in the theoretical spectrum.
As the plasma was running during the measurement, the CO density was increasing, increasing the signal intensity and thus altering the spectrum. Therefore, the wavelength scan was performed faster than usual, with less averages, as the change in signal intensity would distort

the spectra. The result demonstrates, that this approach worked.

These findings indicate that, within the measurement accuracy, the plasma does not significantly influence the rotational temperature of CO under these conditions. With this knowledge, it is now possible to calculate the absolute CO densities produced by the plasma, which is covered in the next section.

5.3 Evolution of Absolute Density in Time

In this section, the absolute CO densities produced by the plasma are determined. Using equation 2.47 from the theoretical background, along with the knowledge that the rotational temperature of CO remains constant at room temperature, the absolute density at each measurement point in time can be determined. With that, there is no need to measure the whole spectrum, and one wavelength is sufficient to calculate the absolute CO density. The wavelength chosen is at maximum signal.

However, there are some uncertainties in this calculation, primarily related to quenching effects. Since CO_2 and CO have different quenching rate coefficients (as shown in table 2.1), the total quenching rate does not remain constant. It is assumed that in principle, it would be possible to recalculate the quenching iteratively at each time step using the first measurement point as a reference. However, the first measurement itself takes a finite amount of time, introducing additional uncertainty that would accumulate over subsequent points. To mitigate this issue, the quenching correction is only applied to the initial gas mixture. Consequently, for all later measurements, the CO density is overestimated. This comes from the values of the quenching frequencies: the CO_2 is overestimated in this calculation and therefore the the quenching is also overestimated. The quenching is in the denominator as in equation 5.3 for the calculation of the branching ratios. The branching ratio itself is in the denominator of the calculation of the CO density as in equation 5.1, so the final calculated CO density is overestimated.

An estimation at the same measurement point found that the difference between a conversion of 0 %, as assumed for the calculation of quenching in this thesis, and a conversion of 100 % of CO_2 to CO would yield a difference in absolute CO density of nearly 46 % for an admixture of 1 % CO_2. The systematic error in calculation therefore is 46 %, but for convenience, the statistical error is used in the graphs.
The equation used to calculate the CO density is:

$$N_{\mathrm{CO}} = \frac{a_{21,\mathrm{ref}}}{a_{21}} \cdot \frac{P_{\mathrm{ref}}^2}{\Gamma_{\mathrm{ref}}} \cdot \frac{\Gamma}{P^2} \cdot N_{\mathrm{CO,ref}} \tag{5.1}$$

with a_{21} being the branching ratio for each case, Γ being the photomultiplier signal and P^2 the diode signal. As can be seen, a reference density is needed, which is obtained by a measurement with fixed admixture. The reference density $N_{\mathrm{CO,ref}}$ is then calculated using the ideal gas law. For a reference pressure of 500 mbar at room temperature, the reference CO density is:

$$N_{\mathrm{CO,ref}} = \frac{p_{\mathrm{par}}}{k_{\mathrm{B}}T} = 1.25 \cdot 10^{23}\,\mathrm{m}^{-3} \tag{5.2}$$

In this equation, p_{par} is the partial pressure of CO, in the case of the reference measurement 5 mbar. The branching ratios are determined as follows:

$$a_{21} = \frac{31\,\mathrm{MHz}}{(0.083\,\frac{\mathrm{MHz}}{\mathrm{mbar}} \cdot f_{\mathrm{He}} + 26\,\frac{\mathrm{MHz}}{\mathrm{mbar}} \cdot f_{\mathrm{CO_2}} + 6.1\,\frac{\mathrm{MHz}}{\mathrm{mbar}} \cdot f_{\mathrm{CO}})p + 31\,\mathrm{MHz} + 13\,\mathrm{MHz}} \tag{5.3}$$

where p is the pressure in mbar and f_i represents the fractional concentration of each gas component.

Since the rotational temperature of CO remains constant at room temperature, this approach for density calculation is valid. If the temperature were not constant, then instead of using the maximum photomultiplier signal divided by the squared photodiode signal, the integrated signal over the whole excitation spectra would be required. The calculated absolute CO densities are shown in figure 5.3.

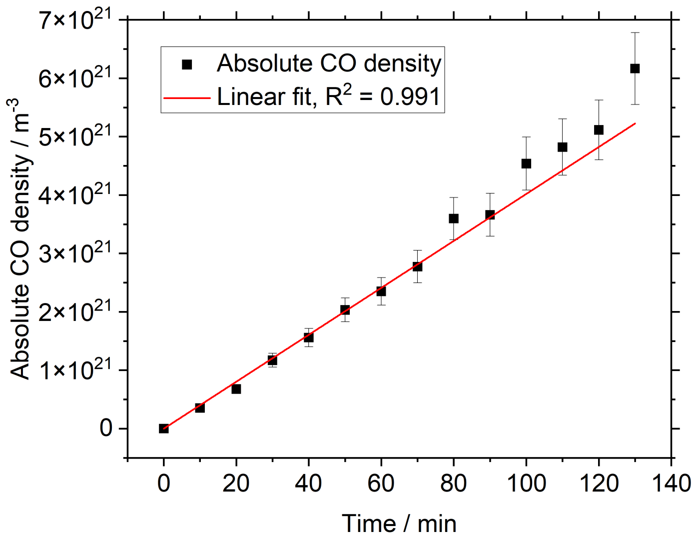

Figure 5.3: Plasma produced absolute CO densities over time. The frequency was 15 kHz, the voltage 600 V and the chamber was initially filled with 797 mbar of He and 7 mbar of CO_2.

As expected, the density increases linearly over time, indicating that the gas exchange within the chamber is highly efficient. This is also supported by the linear fit applied to the measurement points, which has a $R^2 = 0.991$, and thus a great agreement between fit and data. At 130 min, the absolute density reaches a value of $6.16 \pm 0.6 \cdot 10^{21}\,\mathrm{m}^{-3}$. This results in a conversion of $3.5 \pm 0.4\,\%$. In Roloffs work [59], CO densities were determined using Fourier-Transform-Infrared-Spectrometry (FTIR-Spectrometry) to obtain CO_2-to-CO conversion rates of an MCPA of same design as in this thesis. The measured conversion rates ranged between 0.5 % to 1.5 %, depending on the specific plasma parameters. Given that in this experiment, a voltage of 600 V was applied, the observed absolute conversion rate is higher than the expected range.

This can be explained by the difference in the measuring: Roloff measured in flowing mode, and not in stationary mode as done here. Furthermore, Roloff's experiments were performed at the gas exhaust, were then consequently only average values were obtained, where as here, the measurement was performed directly above the cavities, leading to a higher expectation of the density, since the CO will mainly be produced within closely above the cavity. This means, that although not directly comparable due to the different operation modes of the plasma, the obtained results seem reasonable.

In the next chapter, the plasma will be operated in flowing mode. This is the usual operation mode for this specific MCPA. But as already stated in in section 3.4, it is not possible to measure the fluorescence with the PMT in flowing mode operation due to the added quartz glass cover. This is why several precautionary steps must be taken before measuring absolute densities.

6 Flowing Mode Plasma Experiments

In this chapter, the plasma is operated in flowing mode, which represents the typical operation mode for this specific MCPA. The next section covers the background for the absolute density calculation.

6.1 Calculation of Absolute CO Densities using the ICCD Camera

The ICCD images taken consist of not only the CO TALIF signal, but also background noise. This is also the case for the PMT measurements, but there, a single measurement is sufficient for background correction. The background noise of the ICCD images is particularly bad in the case of this thesis, because the quartz glass cover is predestined for stray light in huge amounts. Additionally, the laser beam only has a width of about 200 µm at the measurement location, making the signal area small in contrast to the whole acquired area. A self written script addresses these issues and is described in this section.

In the first step, the program adjusts the values of each pixel of the measurement. This needs to be done to deal with hotspots of cosmic rays. These values, which are much higher then values of the signal, are set to zero. The pixel values are then adjusted with the squared value of the diode signal, as needed for normalisation. The diode signal comes from a simultaneous measurement at the oscilloscope, where 1000 averages are taken.

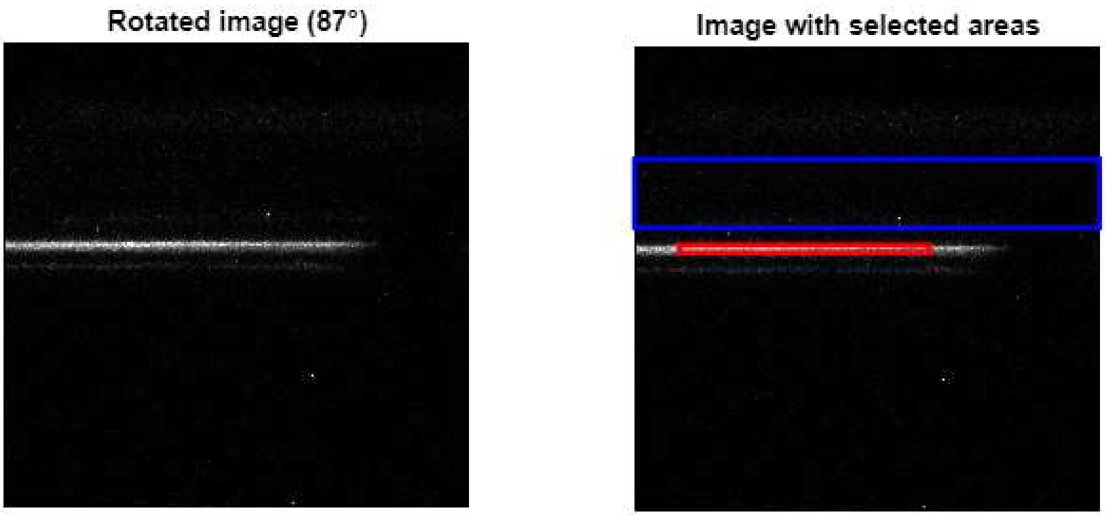

Figure 6.1: The left image shows the rotated and normalised image. Hotspots have been cancelled out. The right image shows the selected areas, with the red rectangular as the signal and the blue rectangular as the background.

In the next step, the taken ICCD image gets rotated by an angle of 87° because of an inaccuracy in the camera placement or the beam path, or even both. The laser beam seems to have a tilt in the original image, which with the chosen angle value is evened out. The last steps are, to choose the areas of interest for the signal as well as for the background. The program then sums up the values of each pixel in the signal and background area, averages both and subtracts the background value from the signal value. In figure 6.1 the areas are marked. Now, the density can be calculated with using the signal value and multiplying it with factor for density calculation ('density factor') which is given by the reference density N_{CO} and the branching ratios for measurement and reference conditions, as shown in equation 2.45 in the theoretical background. With this, the next section covers the quartz glass reflections, and how the background for the density calculation is chosen.

6.2 Reflections in the Quartz Glass Cover

To operate the plasma in flowing mode, a quartz glass cover must be placed over the MCPA array. Unlike standard glass, quartz glass is transparent to VUV light and does not absorb the photons required for TALIF excitation. The quartz glass cover needs to be glued to the array, to ensure that the gas flows over the MCPA and no leakage is happening.
In the following measurements, the detection is done using the ICCD camera instead of the PMT. This is due to geometric reasons, as the quartz glass cover leads to many reflections, making measurements with the PMT challenging. As the rotational temperature stays constant, there is no need for a wavelength scan, and ICCD images can be taken at one laser wavelength.
Initial ICCD images of the MCPA with the laser revealed significant reflections in the upper region of the quartz glass cover. To mitigate this, a 3D-printed plastic mold was attached to the cover, leaving openings only for the laser beam path and the ICCD camera. Figure 6.2 presents an overlay of two ICCD images, highlighting three distinct regions:

- Reflections in the upper part of the quartz glass cover, marked in red.
- The TALIF signal in the middle, signalling the laser beam path, marked in green.
- The plasma cavities at the bottom, marked in blue.

The reflections occur across the entire quartz glass cover, but are most prominent at the top. This may result from the cover's design, where the top section consists of a single quartz glass pane without additional interfaces to refract light. Additionally, the TALIF signal intensity in the middle section is comparable to the reflections, which must be accounted for during data analysis. The image also reveals a tilt in either the MCPA array, the laser beam path, or both. Additionally, the camera can also be the reason for the tilt. Resolving this misalignment was beyond the scope of this thesis, as determining the exact horizontal reference proved challenging. Consequently, image analysis requires an additional rotation correction to align the system horizontally. It is also to note that, in contrast to the PMT, which had a top view of the MCPA, the ICCD camera looks from the side at the MCPA.

In the next section, again a laser intensity variation using ND grey-filters was performed. Due to the change in setup and the introduction of the quartz glass, which weakens the laser beam, a ND grey-filter of smaller attenuation is needed to stay in the linear regime, as done in section 4.3. With a stronger ND grey-filter, the signal-to-noise ratio would just become worse.

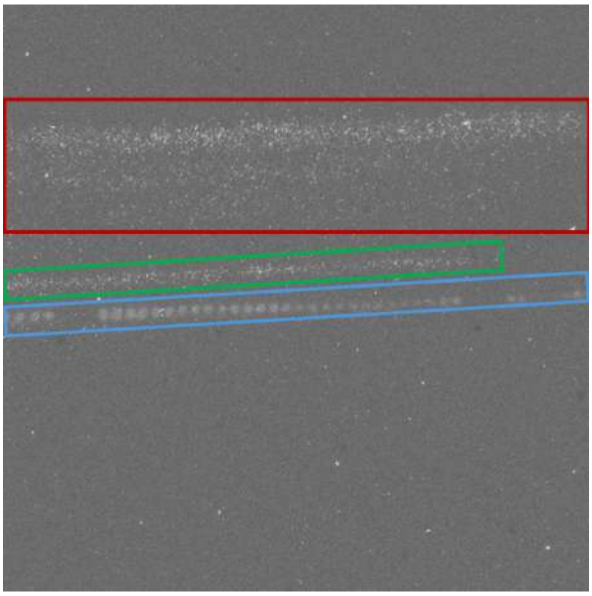

Figure 6.2: Two ICCD images laid on top of each other, showing the reflections of the quartz glass cover, the TALIF signal from the CO and the plasma cavities, from top to bottom.

6.3 Laser Intensity Variation in Flowing Mode

To ensure that the laser energy remains within the linear regime, a neutral density (ND) grey-filter variation was conducted. This experiment aimed to evaluate how the signal intensity changes when different ND grey-filters are applied. Additionally, the quartz glass cover itself reduces the laser energy, which must also be accounted for in the analysis.

For the ND grey-filter variation, the plasma was ignited at a frequency of 15 kHz, a voltage of 700 V and flows of 0.5 slm He as well as 6 sccm CO_2. The image capturing mode was accumulation, with 60 accumulations, a gatewidth of 300 ns, an exposure time of 15 s and a gain of 4000. These settings have been kept constant throughout the following chapter. The results are shown in figure 6.3, with additional detailed images available in the appendix (figures A.1 to A.4). The beam path is clearly distinguishable from the background in the case (a) with no ND grey-filter present in the beam path, and is not distinguishable with a ND0.3 grey-filter. This would hint that, the ND0.1 grey-filter or ND0.2 grey-filter might be the best option for making sure the laser energy is in the linear regime.

Since the quartz glass cover itself reduces the laser energy (because of reflections), its effect was quantified using an energy measurement diode of 541 V/J before and after the beam passed through the glass. The energy before the quartz glass was measured to be 39.7 µJ and after the glass at 18.8 µJ. This corresponds to a transmission of ≈ 75 % per pane, meaning that with two panes in the beam path, a total reduction of ≈ 50 % is expected.
Comparing this to the ND grey-filter measurement performed in section 4.3, the obtained value of 75 % transmission lies between ND0.1 (79 % transmission) and ND0.2 (63 % transmission). This means that an additional ND grey-filter is unnecessary. As we made sure that we have a good signal-to-noise ratio and are within the linear regime of the laser energy, we can now proceed with the measurement of absolute CO densities over time in the next section, as the changed setup is sufficiently explored.

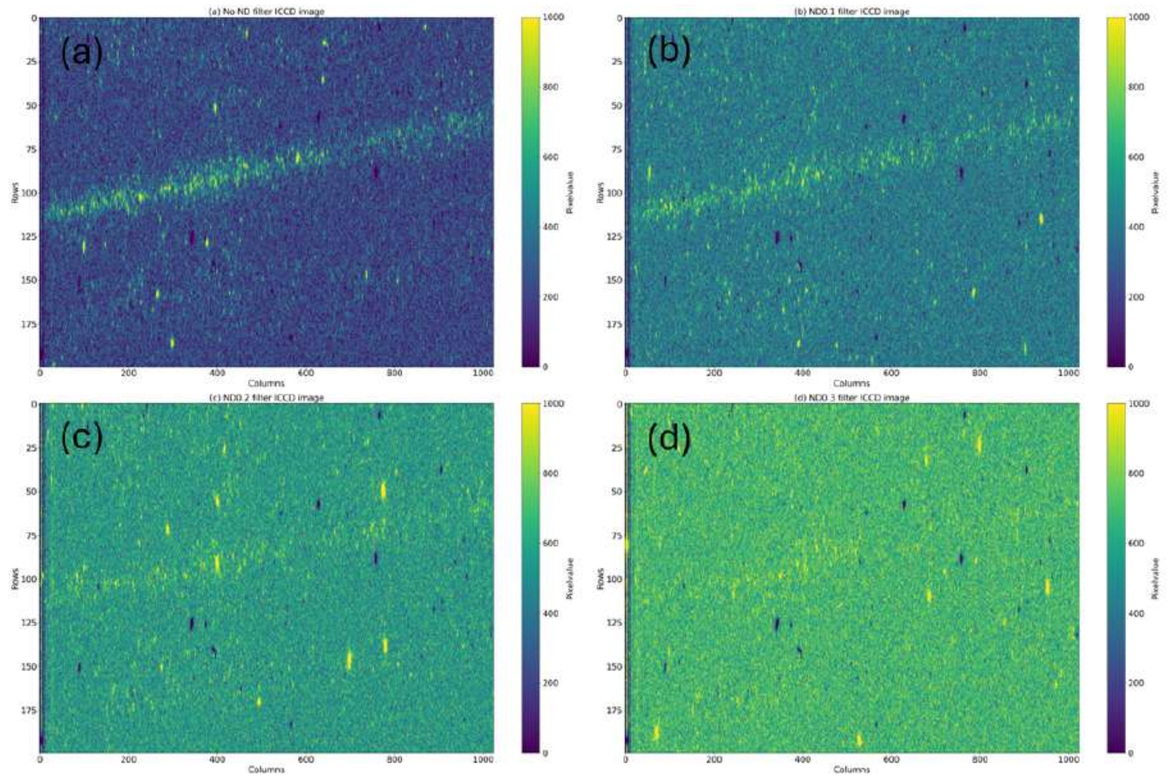

Figure 6.3: Results of the ND grey-filter variation. Illustrated are: (a) no ND grey-filter in beam path, (b) ND0.1 grey-filter, (c) ND0.2 grey-filter, (d) ND0.3 grey-filter.

6.4 Temporal Evolution of the CO Density

This section presents the measurement of absolute CO densities for constant plasma conditions to investigate a potential accumulation of CO under the glass cover. For this measurement, the plasma was ignited with 15 kHz at 700 V with a Helium flow of 0.5 slm and 6 sccm CO_2. The measured CO density over time is shown in figure 6.4.

For the measurement procedure, each image was obtained by accumulating data for 10 min to ensure a better signal-to-noise ratio. While shorter time steps (shorter than 10 min) were possible, they would have increased noise levels and reduced precision in analysis of the TALIF signal.

As shown in figure 6.4, the absolute CO densities in flowing mode are within the same order of magnitude as those observed in stationary operation. This confirms that the setup functions consistently in both modes, but is somewhat surprising that in the stationary case, the CO density is comparable, as one would expect higher densities. A slight CO build-up is observed in the first 10–20 min, after which an equilibrium is reached. However, the last measurement point at 50 min is slightly lower than the preceding one. Since this deviation remains within the error margin, the observed trend remains valid. In further measurements, this time constant until the plasma reaches an equilibrium has to be taken into account. The obtained absolute density of $\approx 7.9 \cdot 10^{21}\,\mathrm{m}^{-3}$ corresponds to a conversion rate of $3.2 \pm 0.3\,\%$.

When compared to the 20 % up to 30 % conversion rate measured by Damen et al. [20] in a CO_2 glow discharge using TALIF, this value appears low. However, their experiments were conducted in a pure CO_2 glow discharge plasma, whereas in this thesis, a DBD is used and additionally, the pressure used in their work is significantly lower, meaning they have less CO_2 molecules that can be converted to CO. The observed conversion is consistent with stationary plasma operation, indicating the result is reproducible.

In the following section, the distance of the MCPA to the laser beam will be varied to determine where the majority of CO_2 conversion is taking place.

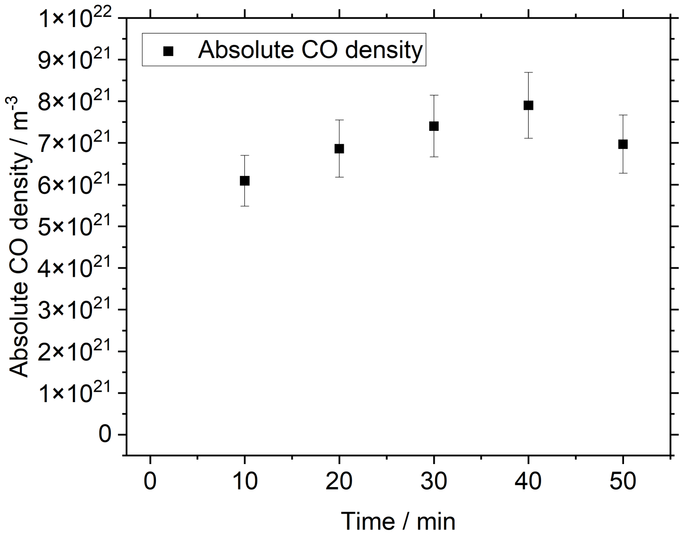

Figure 6.4: Time Variation of the plasma being operated in flowing mode.

6.5 Distance Variation between the MCPA and the Laser Beam

In this section, the height of the array is varied using the z-stage. The lowest possible distance is 0 mm, where the laser beam with 200 µm remains unobstructed. Any further decrease in height would result in partial beam cut-off. The plasma parameters remain unchanged from the previous measurements. The results are shown in figure 6.5.

A decrease in absolute CO density is observed as the measurement moves further from the plasma. This is expected since, at greater distances, the energy required for CO_2 dissociation via stimulated vibrational excitation may not be given by the plasma electrons. Additionally, diffusion of the CO away from the plasma also is a reason for this trend. The highest CO density is measured directly above the plasma, matching the values obtained in the time variation experiments. As a result, the conversion rate remains approximately the same at $3.0 \pm 0.3\,\%$. The best distance for conversion is therefore directly over the cavities.

In the next section, the voltage will be varied to determine the optimal conditions for maximizing CO_2 conversion.

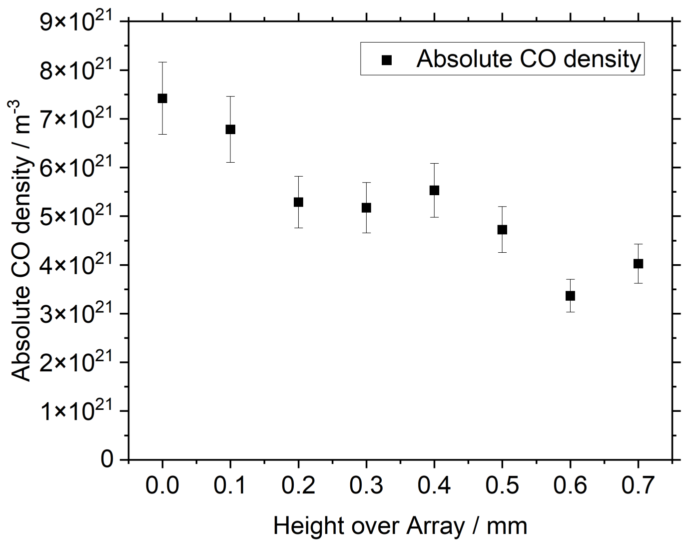

Figure 6.5: Variation of the distance between the MCPA and the laser beam.

6.6 Voltage Variation

In this section, the applied plasma voltage amplitude is varied between 600 V and 720 V to determine its effect on CO_2 conversion efficiency. It is expected, that for a higher voltage, the plasma has a higher power density and therefore, more high-energy electrons, which can dissociate more CO_2. The gas flow rates remain unchanged at 0.5 slm of He and 6 sccm of CO_2. The results are presented in figure 6.6.

A clear linear increase in absolute CO density is observed with increasing voltage. The highest measured CO density occurs at 720 V, reaching $\approx 1.1 \cdot 10^{22}\,\mathrm{m}^{-3}$, which corresponds to a conversion rate of $3.7{\pm}0.4\,\%$. While this is the highest conversion rate measured in this study, it remains significantly lower than the values reported by Damen et al. [20], who achieved conversion rates between 20 % and 30 % in a CO_2 glow discharge. This discrepancy could be attributed to differences between a DBD discharge and the glow discharge, as described earlier.

For this DBD, this is the highest measured conversion rate and therefore a success, as it shows the capability of the DBD of CO_2-dissociation. Additionally, many optimisations are possible, for example the use of catalysts, to improve the conversion rate even more.

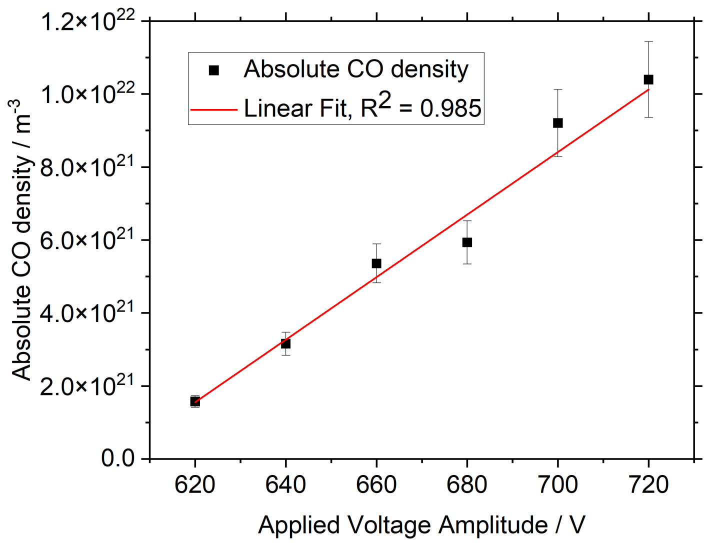

Figure 6.6: Variation of the applied voltage amplitude.

6.7 Further Measurements

One of the goals of this thesis was to achieve a 2D spatial resolution of the densities. While this goal could not be fully realised in the current study, valuable insights were gained regarding the challenges associated with this type of measurement. The reasons for that are:

- Low signal-to-noise ratio: In the analysis of the ICCD images beforehand, the whole signal area was selected and integrated to obtain the absolute densities. When trying to do it for each pixel, some pixels have a value that is only on the level of the background, making the whole signal not trustworthy. This highlights the need for future studies to explore techniques for improving the signal-to-noise ratio.

- Errors in analysis: The fact that for a good signal to be obtained, the background needs to be subtracted, causes further problems in analysis. Some pixels of the selected signal area have values that lay beneath the mean of the background, leading to densities of zero in those specific pixels. Addressing this issue could involve refining the background correction method or improving the sensitivity of the measurements.

One potential solution to this would be to increase the exposure time even further, which already is at 10 min for each measurement point. This was deemed not suitable within means of this thesis, but future experiments could explore this option. Another idea would be to increase the laser power further, although this might lead to signals out of the linear regime.

Another measurement that proved unsuccessful is the variation of the CO_2 gas flow, measured with the ICCD camera. The data were not reproducible, and multiple attempts resulted in inconsistent trends. The reason for this might be the limited usability and accuracy of the mass flow controllers at low flow rates. The mass flow controller works up to 100 sccm, but it might not work at flows of 5 sccm. The change of the mass flow controllers to for example one of 25 sccm would possibly enable this measurement.

7 Conclusion and outlook

In this thesis, the conversion of CO_2 to CO using a MCPA was investigated through two-photon absorption laser-induced fluorescence (TALIF). The TALIF experiment was set up and thoroughly analysed before a fitting routine was applied to the measured excitation spectra to determine the rotational temperatures of CO. Subsequently, absolute CO densities were measured under two different plasma operation modes while varying plasma conditions.

The laser setup, consisting of the Nd:YAG laser and the dye laser, was carefully characterised. The energy of the Nd:YAG laser beam was monitored over time to ensure stability during measurements, which lasted several hours. After the warm-up phase, the Nd:YAG laser maintained a constant energy output of 320 mJ per pulse. The dye laser's output energy was measured at approximately 300 µJ, showing a decreasing trend likely caused by thermal effects, possibly unrelated to the laser itself. Despite the air-conditioned laboratory environment, temperature fluctuations still might have affected the second and third harmonic generator crystals, leading to a poorer laser profile in space and thus, to a smaller energy per pulse.

Another critical aspect of the laser beam was its polarisation, as the calculation of absolute CO density assumes linear polarisation. To verify this, a single polarisation filter was placed in the laser beam, and the intensity was measured at different angles. The results followed a $\cos^2(\theta)$ pattern, consistent with Malus' law, confirming that the laser light was indeed linearly polarised.

The crystal alignment posed a significant challenge during this work. In contrast to TALIF on atomic oxygen, TALIF for CO needs a whole excitation spectrum to determine absolute densities. Therefore, the alignment of the crystals, resulting in a good and evenly distributed laser profile in space, is absolutely crucial to obtain reasonable results for the absolute CO densities. Several approaches were tested to optimise the quality of the excitation spectra, but they were ultimately unsuccessful. The breakthrough came with the implementation of a LabVIEW program that automated crystal adjustments via an Arduino interface, using step sizes determined manually. This proved to be the breakthrough, as now the measured excitation spectra were in agreement with the theoretical spectra.

Additionally, the laser beam profile was examined at different wavelengths to obtain a comprehensive understanding of its behaviour. While the profile was not ideal, it remained consistent across the entire spectral range when the crystals were properly adjusted.

Another crucial measurement involved determining whether the laser energy operated in the linear or saturated regime. This was assessed using neutral density (ND) grey-filters for an laser energy variation and a delay variation of the laser amplifier of the Nd:YAG. The results confirmed that an ND grey-filter was necessary to ensure operation within the linear regime. With these characterisations completed, the laser system was deemed sufficiently optimised for TALIF measurements. Thus, the first major step of this thesis to achieve the goal of measuring absolute CO densities, the development of the TALIF setup, incorporating both a photomultiplier and an ICCD camera, was successfully achieved.

Before proceeding with the TALIF measurements, a pressure variation study was conducted to validate the correct handling of collisional quenching in data analysis. The TALIF signal was divided by the branching ratio, revealing a clear linear relationship, confirming that the quenching correction was correctly implemented. This validation enabled the subsequent plasma experiments.

A distance variation study was performed to assess how the signal changed when the laser beam was obstructed by the array. This experiment also provided an estimation of the statistical error.

The plasma was operated in two different modes: in a stationary atmosphere and a flowing mode. Initial experiments in stationary mode led to the following observations:

- Validation of CO Detection: The chamber was filled with helium and CO_2, and an increase in the TALIF signal from CO was observed, as expected in a stationary atmosphere. Since CO is a stable molecule in this setting with no gas exchange, its presence confirmed the system's capability to detect CO.
- Rotational Temperature of CO: The plasma was ignited for several hours while the chamber remained filled with helium and CO_2. Even after six hours, no increase in the rotational temperature was observed. The temperature was determined using a fitting routine applied to the measured spectra. This finding suggests that the microscaled DBD used in this thesis does not significantly affect the rotational temperature within the measurement and fitting accuracy.
- Absolute CO densities: With the established rotational temperature, absolute CO densities were determined over time. The results showed a linear increase in density, as expected. No saturation was observed after two hours, though it is anticipated once the available CO_2 is nearly depleted. The maximum measured CO density was $6.16 \pm 0.6 \cdot 10^{21}\,\mathrm{m}^{-3}$, corresponding to a CO_2-to-CO conversion of $3.5 \pm 0.4\,\%$, which aligns well with conversion rates reported by Roloff [59].

Before conducting absolute CO density measurements in the flowing mode, modifications to the setup were necessary. A quartz glass cover was added atop the MCPA to maintain gas flow at atmospheric pressure. This alteration necessitated a laser intensity variation study using ND grey-filters, which revealed that no additional ND grey-filter was required, as the quartz glass cover itself transmitted only 75 % of the laser energy per pane.

In the next experiment, the potential build up of CO under the quartz glass cover was examined. Despite the long accumulation time of 10 min per data point using the ICCD camera, a slight increase in CO density was detected. The measured densities were on the same order of magnitude as those from stationary operation, with a maximum conversion rate of $3.2 \pm 0.3\,\%$, again consistent with values reported by Roloff.

A distance variation experiment was then conducted, where the MCPA was moved relative to the laser beam. The highest CO density was found directly above the plasma, as close as possible to the MCPA without obstructing the laser. The measured density of $7.4 \cdot 10^{21}\,\mathrm{m}^{-3}$ corresponds to a conversion rate of $3.0 \pm 0.3\,\%$.

Finally, a voltage variation study was performed. The highest CO density recorded in this thesis was $1 \cdot 10^{22}\,\mathrm{m}^{-3}$, resulting in a conversion of $3.7 \pm 0.4\,\%$. This density was measured at the highest applied voltage, and the density increased linearly with voltage. In [59], Roloff however measured a quadratic dependence. Nevertheless, the result remains reasonable.

The statistical error in the measurement data was estimated to be approximately 10 %. However, the systematic error - primarily driven by uncertainties in quenching calculations - was estimated at nearly 50 %, as is common in TALIF measurements. The recursive nature of the quenching calculation, which depends on fractional gas components, contributes significantly to this uncertainty. A quenching factor calculation assuming both 0 % and 100 % CO_2-to-CO conversion resulted in a 46 % variation of the absolute CO density, indicating that the absolute CO densities reported in this thesis may be overestimated.

In conclusion, the second main step of this thesis, measuring the rotational temperature of CO from the plasma, was successfully achieved, along with key aspects of the third goal: determining absolute CO densities under different plasma conditions.

However, spatially resolving CO production within the plasma was not achieved due to a low signal-to-noise ratio. While integrated signals provided reasonable density estimates, individual pixel values were too small for reliable spatial mapping. This could be improved by increasing the exposure time. Additionally, challenges arose in background subtraction, sometimes leading to negative densities. Thus, while spatial resolution remains feasible, further improvements are necessary.

Another limitation was the unsuccessful variation of gas admixtures in flowing mode, as the 100 sccm mass flow controller operated near its lower limit, causing inconsistencies. This issue could be resolved by using a lower-range mass flow controller (e.g., a maximum flow of 25 sccm).

Overall, this thesis was a success. Nearly all objectives were met, and the results align well with comparable studies. Future work could focus on achieving spatial resolution of CO densities and measuring a flow variation.

A Appendix

The calculation for the gas correction factors works as follows: the scaling control factor (SCF) is equal to the product of the gauge factor (GF) and the gas correction factor (GCF):

$$\mathrm{SCF} = \mathrm{GF} \cdot \mathrm{GCF} \tag{A.1}$$

The gas correction factor itself consists of the product of the conversion factor (CF), provided by the manufacturer, and a correction for temperature, in our case to room temperature:

$$\mathrm{GCF} = \mathrm{CF} \cdot \frac{293\,\mathrm{K}}{273.15\,\mathrm{K}} \tag{A.2}$$

Putting the two equations together:

$$\mathrm{SCF} = \mathrm{GF} \cdot \mathrm{CF} \cdot \frac{293\,\mathrm{K}}{273.15\,\mathrm{K}} \tag{A.3}$$

we obtain the SCF values for both He and CO_2 of

$$\mathrm{SCF}_{\mathrm{He}} = 100 \cdot 1.45 \cdot \frac{293\,\mathrm{K}}{273.15\,\mathrm{K}} = 155.5 \tag{A.4}$$

$$\mathrm{SCF}_{\mathrm{CO}_2} = 100 \cdot 0.7 \cdot \frac{293\,\mathrm{K}}{273.15\,\mathrm{K}} = 75.1 \tag{A.5}$$

In the case of the premixed bottle, the SCF value is not the weighted average of the single values for He and CO, it has to be calculated like this, according to the manufacturer [60]:

$$\mathrm{GCF} = \frac{0.3106 \cdot (a_1 s_1 + a_2 s_2)}{(a_1 d_1 c_1 + a_2 d_2 c_2)} \tag{A.6}$$

In this equation, the a_i stands for the fractional flow, s_i is the molecular structure correction factor, d_i stands for the densities of the gases and c_i for the specific heat of the gases. The values are shown in table A.1. The calculation of the SCF is then:

$$\mathrm{SCF}_{HeCO} = 100 \cdot 1.43 \cdot \frac{293\mathrm{K}}{273.15\mathrm{K}} = 153.3 \tag{A.7}$$

Constant	Value	Constant	Value	Constant	Value
a_{He}	0.99	d_{He}	$0.1786\,\frac{g}{l}$	c_{He}	$1.241\,\frac{cal}{g°C}$
a_{CO}	0.01	d_{CO}	$1.964\,\frac{g}{l}$	c_{CO}	$0.2016\,\frac{cal}{g°C}$

Table A.1: Constants used for calculation of the GCF for gas mixtures. Values taken from [60].

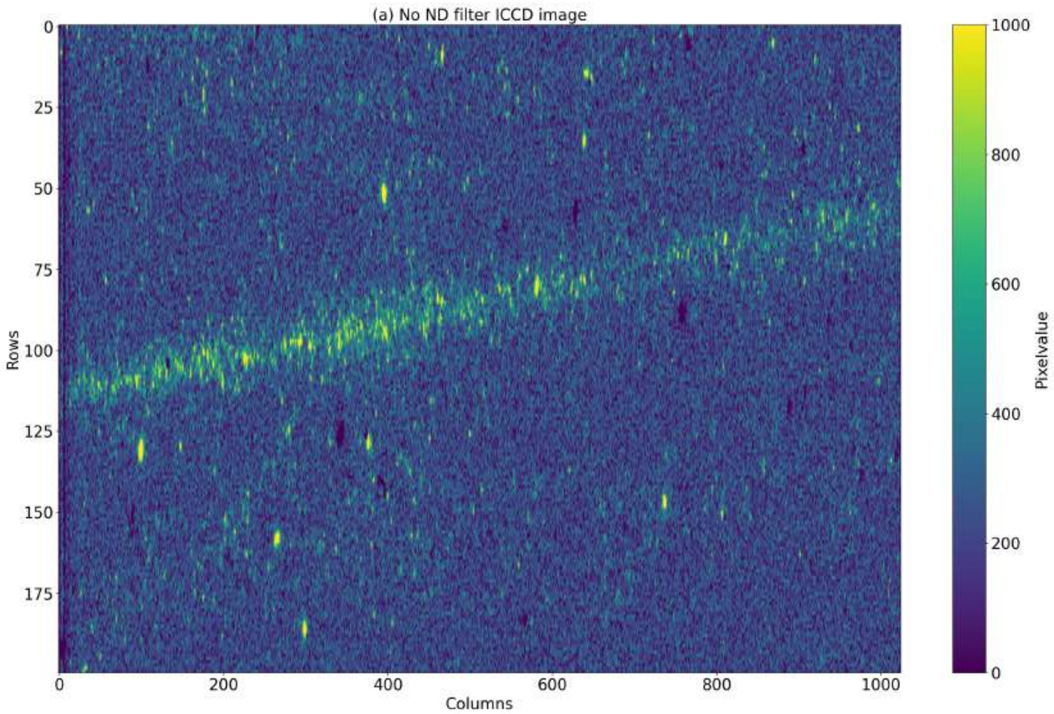

Figure A.1: Results of the ND grey-filter variation with no ND grey-filter.

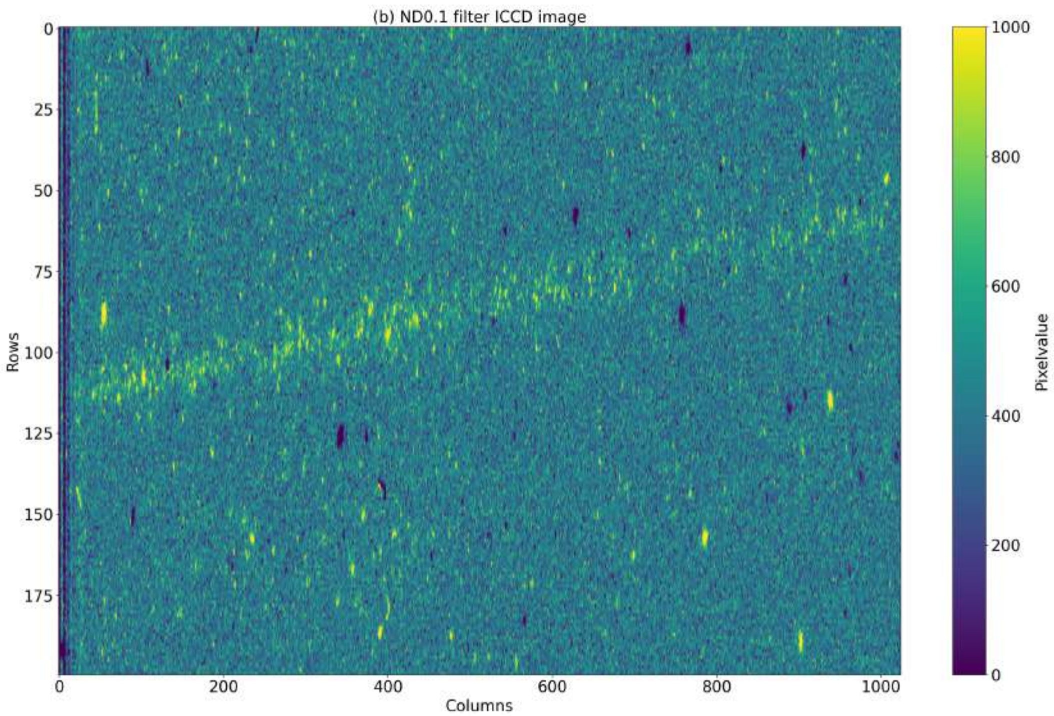

Figure A.2: Results of the ND grey-filter variation with ND0.1 grey-filter.

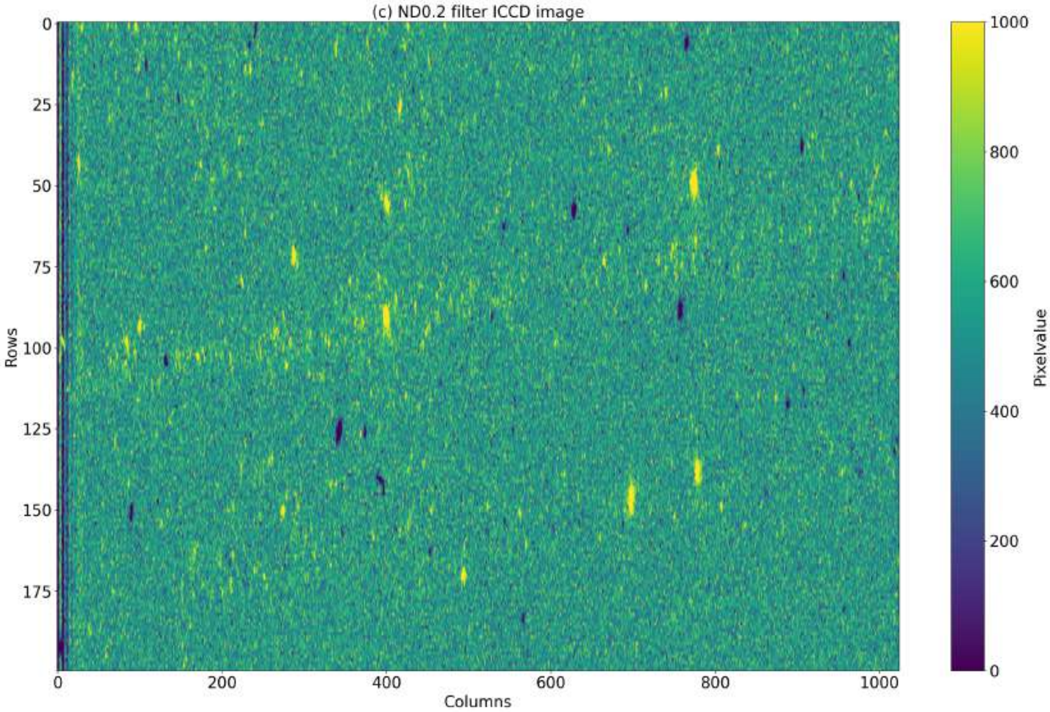

Figure A.3: Results of the ND grey-filter variation with ND0.2 grey-filter.

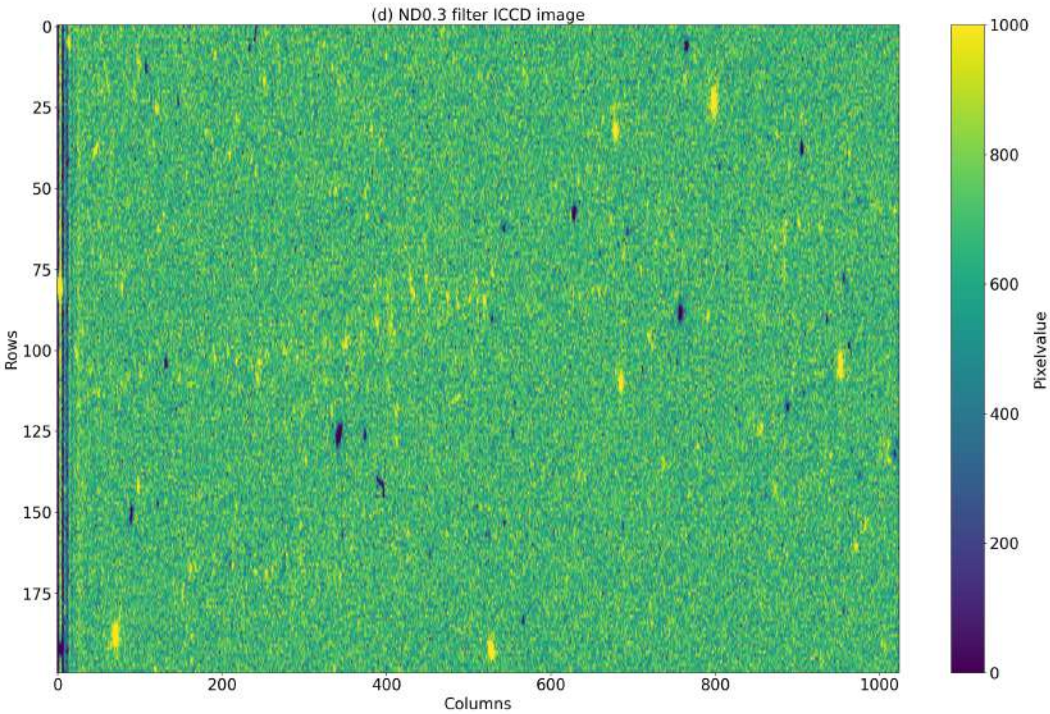

Figure A.4: Results of the ND grey-filter variation with ND0.3 grey-filter.

Literature

[1] V. Masson-Delmotte et al. “Climate Change 2021: The Physical Science Basis. Contribution of Working Group I to the Sixth Assessment Report of the Intergovernmental Panel on Climate Change.” In: *IPCC, 2021: Summary for Policymakers* (2021). DOI: doi:10.1017/9781009157896.001 (cit. on p. 1).

[2] R. M. Hochstrasser R. G. Bray. “Climate Change and the Impact of Greenhouse Gasses: CO2 and NO, Friends and Foes of Plant Oxidative Stress.” In: *Frontiers in Plant Science* (2018). DOI: 10.3389/fpls.2018.00273 (cit. on p. 1).

[3] C. F. Baes et al. “Carbon Dioxide and Climate: The Uncontrolled Experiment.” In: *American Scientist, 65(3), 310–320* (1977). DOI: http://www.jstor.org/stable/27847841 (cit. on p. 1).

[4] R. C. Duncan. “World Energy Production, Population Growth, and the Road to the Olduvai Gorge.” In: *Population and Environment 22, 503–522 (2001)* (2001). DOI: https://doi.org/10.1023/A:1010793021451 (cit. on p. 1).

[5] G. Yamamoto. “Direct Absorption of Solar Radiation by Atmospheric Water Vapor, Carbon Dioxide and Molecular Oxygen.” In: *J. Atmos. Sci., 19, 182–188* (1962). DOI: https://doi.org/10.1175/15200469(1962)019<0182:DAOSRB>2.0.CO;2. (cit. on p. 1).

[6] R. Rohde. *Global Temperature Report for 2024*. Online, Link:https://berkeleyearth.org/global-temperature-report-for-2024/. 2025 (cit. on p. 1).

[7] National Academies of Sciences et al. *Attribution of Extreme Weather Events in the context of Climate Change*. Book, Link: https://nap.nationalacademies.org/catalog/21852/attribution-of-extreme-weather-events-in-the-context-of-climate-change. 2016 (cit. on p. 1).

[8] E. Rignot et al. “Ice-Shelf Melting Around Antarctica.” In: *Science 341, 266-270* (2002). DOI: https://doi.org/10.1126/science.1235798 (cit. on p. 1).

[9] P. Huybrechts et al. “The greenland ice sheet and greenhouse warming.” In: *Palaeogeography, Palaeoclimatology, Palaeoecology 89, 4* (1991). DOI: https://doi.org/10.1016/0031-0182(91)90174-P (cit. on p. 1).

[10] E. Kabir et al. “Solar energy: Potential and future prospects.” In: *Renewable and Sustainable Energy Reviews, 82, 1, pp. 894-900* (2018). DOI: https://doi.org/10.1016/j.rser.2017.09.094 (cit. on p. 1).

[11] C.-J. Liu et al. “Non-thermal plasma approaches in CO2 utilization.” In: *Fuel Processing Technology, 58, 2-3* (1999). DOI: https://doi.org/10.1016/S0378-3820(98)00091-5 (cit. on p. 1).

[12] J. Van Durme et al. “Combining non-thermal plasma with heterogeneous catalysis in waste gas treatment: A review.” In: *Applied Catalysis B: Environmental, 78, 3–4* (2008). DOI: https://doi.org/10.1016/j.apcatb.2007.09.035 (cit. on p. 1).

[13] J. Golda et al. “Circular Emission and Destruction Patterns on a Silicon-Based Microdischarge Array.” In: *IEEE Transactions on Plasma Science, vol. 42, no. 10, pp. 2646-2647* (2024). DOI: 10.1109/TPS.2014.2337657 (cit. on p. 1).

[14] S. Dzikowski et al. "Modular constructed metal-grid arrays—an alternative to silicon-based microplasma devices for catalytic applications." In: *Plasma Sources Science and Technology 29,3* (2020). DOI: `10.1088/1361-6595/ab71f6` (cit. on pp. 1, 4).

[15] S. Dzikowski et al. "Electric field strengths within a micro cavity plasma array measured by Stark shift and splitting of a helium line pair." In: *Plasma Sources Science and Technology 31,6* (2022). DOI: `https://dx.doi.org/10.1088/1361-6595/ac7820` (cit. on pp. 1, 27).

[16] H. van Impel et al. "Electric field components within a micro-scaled DBD measured by Stark shifting and splitting of helium lines." In: *Plasma Sources Sci. Technol. 33 105008* (2024). DOI: `10.1088/1361-6595/ad7d34` (cit. on p. 1).

[17] S. Kreuznacht et al. "Intra-cavity dynamics in a microplasma channel by side-on imaging." In: *Plasma Sources Sci. Technol. 30 015014* (2021). DOI: `10.1088/1361-6595/abd61e` (cit. on p. 1).

[18] D. Steuer et al. "Spatially and temporally resolved atomic oxygen densities in a micro cavity plasma array." In: *Plasma Sources Sci. Technol. 32 025013* (2023). DOI: `10.1088/1361-6595/acb9b9` (cit. on p. 1).

[19] R. Labenski et al. "Novel methods for determination and manipulation of surface charges performed on an atmospheric DBD microplasma." In: *Plasma Sources Sci. Technol. 33 105022* (2024). DOI: `10.1088/1361-6595/ad802d` (cit. on p. 1).

[20] M. A. Damen et al. "Absolute CO number densities measured using TALIF in a non-thermal plasma environment." In: *Plasma Sources Sci. Technol. 28 115006* (2019). DOI: `10.1088/1361-6595/ab496e` (cit. on pp. 2, 10–12, 21–23, 60, 63).

[21] L. W. Dotchin et al. "The Fischer–Tropsch process: 1950–2000." In: *Catalysis Today, 71, 3–4,* (2000). DOI: `https://doi.org/10.1016/S0920-5861(01)00453-9.` (cit. on p. 2).

[22] W. Siemens. "Ueber die elektrostatische Induction und die Verzögerung des Stroms in Flaschendrähten." In: *Annalen der Physik 178, 9* (1857). DOI: `https://doi.org/10.1002/andp.18571780905` (cit. on p. 3).

[23] Y. Mou et al. "Surface modification of carbon-based materials using a double dielectric barrier discharge for efficient removal of OPFRs with different polarity." In: *Journal of the Indian Chemical Society 101,1* (2023). DOI: `https://doi.org/10.1016/j.jics.2023.101112` (cit. on p. 3).

[24] R. De Meyer et al. "Importance of plasma discharge characteristics in plasma catalysis: Dry reforming of methane vs. ammonia synthesis." In: *Chemical Engineering Journal 488* (20204). DOI: `https://doi.org/10.1016/j.cej.2024.150838` (cit. on p. 3).

[25] R. Brandenburg et al. "Plasma-Based Pollutant Degradation in Gas Streams: Status,Examples and Outlook." In: *Contributions to Plasma Physics* (2014). DOI: `https://doi.org/10.1002/ctpp.201310059` (cit. on p. 3).

[26] U. Kogelschatz. "Dielectric-Barrier Discharges: Their History, Discharge Physics, and Industrial Applications." In: *Plasma Chemistry and Plasma Processing 23, 1–46* (2003). DOI: `https://doi.org/10.1023/A:1022470901385` (cit. on p. 3).

[27] R. Brandenburg. "Dielectric barrier discharges: progress on plasma sources and on the understanding of regimes and single filaments." In: *Plasma Sources Sci. Technol. 26 053001* (2017). DOI: `10.1088/1361-6595/aa6426` (cit. on pp. 3, 4).

[28] K. Buss. "Die elektrodenlose Entladung nach Messung mit dem Kathodenoszillographen." In: *Archiv f. Elektrotechnik 26, 261–265* (1932). DOI: `https://doi.org/10.1007/BF01657192` (cit. on p. 4).

[29] F. Massines et al. "Experimental and theoretical study of a glow discharge at atmospheric pressure controlled by dielectric barrier." In: *J. Appl. Phys. 83, 2950–2957* (1998). DOI: `https://doi.org/10.1063/1.367051` (cit. on p. 4).

[30] S. Okazaki et al. "Appearance of stable glow discharge in air, argon, oxygen and nitrogen at atmospheric pressure using a 50 Hz source." In: *J. Phys. D: Appl. Phys. 26 889* (1993). DOI: `10.1088/0022-3727/26/5/025` (cit. on p. 4).

[31] D. Steuer et al. "Mode transition in a helium barrier discharge with oxygen admixtures: insights into a micro cavity plasma array reactor." In: *J. Phys. D: Appl. Phys. 58 085211* (2024). DOI: `10.1088/1361-6463/ad9ebe` (cit. on p. 4).

[32] F. Massines et al. "Recent advances in the understanding of homogeneous dielectric barrier discharges." In: *European Physical Journal-applied Physics* (1998). DOI: `10.1051/epjap/2009064.` (cit. on p. 4).

[33] Y. Akishev et al. "'Memory' and sustention of microdischarges in a steady-state- DBD: volume plasma or surface charge?" In: *Plasma Sources Sci. Technol. 20 024005* (2011). DOI: `10.1088/0963-0252/20/2/024005` (cit. on p. 4).

[34] A. Fridman. *Plasma Chemistry.* Cambridge University Press, 2008. DOI: `https://doi.org/10.1017/CBO9780511546075` (cit. on pp. 4–9).

[35] F. Kneubühl and M. Sigrist. *Laser.* Vieweg+Teubner, pp. 229f, 2008. DOI: `ISBN978-3-8351-0145-6` (cit. on p. 5).

[36] H. van Impel. *Analyse des elektrischen Feldes in einer mikroskalierten dielektrisch behinderten Entladung.* Master Thesis, Ruhr-Universitaet Bochum. 2023 (cit. on p. 6).

[37] D. Larsen et al. *Physical Chemistry.* 2025 (cit. on p. 10).

[38] E. Condon. "A theory of Intensity Distribution in Band Systems." In: *Phys. Rev. 28, 1182* (1926). DOI: `https://doi.org/10.1103/PhysRev.28.1182` (cit. on p. 9).

[39] A. W. van de Steeg. *Two-photon absorption laser induced fluorescence on carbon monoxide for spatially resolved temperature measurements.* Master Thesis, Eindhoven University of Technology. 2018 (cit. on pp. 11, 13, 18, 20).

[40] R. G. Bray and R. M. Hochstrasser. "Two-photon absorption by rotating diatomic molecules." In: *Molecular Physics, 31(4), 1199–1211* (1976). DOI: `https://doi.org/10.1080/00268977600100931` (cit. on pp. 10, 11).

[41] C.-Y. She. "Spectral structure of laser light scattering revisited: bandwidths of nonresonant scattering lidars." In: *Applied Optics. 40. 4875-4884* (2001). DOI: `10.1364/AO.40.004875` (cit. on p. 10).

[42] P.J.H. Tjossem and K. C. Smyth. "Multiphoton excitation spectroscopy of the $B^1\Sigma^+$ and $C^1\Sigma^+$ Rydberg states of CO." In: *J. Chem. Phys. 91 (4): 2041–2048* (1989). DOI: `https://doi.org/10.1063/1.457064` (cit. on p. 11).

[43] G. W. Loge et al. "Multiphoton induced fluorescence and ionization of carbon monoxide $B^1\Sigma^+$." In: *J. Chem. Phys. 79 (1): 196–202* (1983). DOI: `https://doi.org/10.1063/1.445556` (cit. on p. 11).

[44] V. Schulz-von der Gathen. *Plasmadiagnostik.* Lecture Script, Ruhr-Universitaet Bochum. 2023 (cit. on p. 14).

[45] F. Di Teodoro et al. "Collisional quenching of $CO^+ B^2\Sigma^+(\nu = 0)$ probed by two-photon laser-induced fluorescence using a picosecond laser." In: *The Journal of Chemical Physics 113, 8* (2000). DOI: `https://doi.org/10.1063/1.1287144` (cit. on pp. 16, 20, 21, 46).

[46] R. T. Jongma et al. "Double-resonance spectroscopy on triplet-states of CO." In: *Journal of Molecular Spectroscopy, 165, 2, pp. 303-314* (1994). DOI: `https://doi.org/10.1006/jmsp.1994.1134` (cit. on p. 19).

[47] L. Chantranupong et al. "A configuration interaction study of the oscillator strengths for various low-lying transitions of the CO molecule." In: *Chemical Physics, 161, 3,pp. 351-362,* (1992). DOI: `https://doi.org/10.1016/0301-0104(92)80152-L` (cit. on p. 20).

[48] W. F. Chan et al. "Absolute optical oscillator strengths for discrete and continuum photoabsorption of carbon monoxide (7-200 eV) and transition moments for the $X^1\Sigma^+ \rightarrow A^1\Pi$ system." In: *Chemical Physics, 170, 1, pp. 123-138* (1992). DOI: `https://doi.org/10.1016/0301-0104(93)80098-T` (cit. on p. 20).

[49] L. W. Dotchin et al. "Radiative lifetimes and pressure dependence of the relaxation rates of some vibronic levels in N2, N2, CO+, and CO." In: *J. Chem. Phys. 59, 3960–3967* (2000). DOI: `https://doi.org/10.1063/1.1680585` (cit. on p. 20).

[50] T. B. Settersten et al. "Temperature- and species-dependent quenching of CO B probed by two-photon laser-induced fluorescence using a picosecond lasers." In: *The Journal of Chemical Physics 117, 7, pp. 3173-3179* (2002). DOI: `10.1063/1.1493198` (cit. on p. 21).

[51] M. D. Di Rosa and R. L. Farrow. "Temperature-dependent collisional broadening and shift of Q-branch transitions in the B←X(0,0) band of CO perturbed by N_2, CO_2 and CO." In: *Journal of Quantitative Spectroscopy and Radiative Transfer 68, 4* (2001). DOI: `https://doi.org/10.1016/S0022-4073(00)00029-7` (cit. on pp. 21, 31, 32).

[52] M. D. Di Rosa and R. L. Farrow. "Two-photon excitation cross section of the B ← X(0,0) band of CO measured by direct absorption." In: *J. Opt. Soc. Am. B 16, 1988-1994* (1999). DOI: `https://doi.org/10.1364/JOSAB.16.001988` (cit. on pp. 21, 31, 32).

[53] M. D. Di Rosa and R. L. Farrow. "Cross sections of photoionization and ac Stark shift measured from Doppler-free B ← X(0,0) excitation spectra of CO." In: *J. Opt. Soc. Am. B 16, 861-870* (1999). DOI: `https://doi.org/10.1364/JOSAB.16.000861` (cit. on p. 21).

[54] A. C. Le Floch and C. Amiot. "Fourier transform spectroscopy of the CO Ångström bands." In: *Chemical Physics, Volume 97, Issues 2–3* (1985). DOI: `https://doi.org/10.1016/0301-0104(85)87046-4` (cit. on p. 21).

[55] A. Böddeker. *Vergleich der atomaren Sauerstoffdichten in einem coplanaren Plasmajet mit ns- oder RF-Anregung.* Master Thesis, Ruhr-Universitaet Bochum. 2019 (cit. on p. 26).

[56] P. J. Harrop and J. N. Wanklyn. "The dielectric constant of zirconia." In: *Br. J. Appl. Phys. 18 739* (1967). DOI: `10.1088/0508-3443/18/6/305` (cit. on p. 26).

[57] G. Herzberg. *Molecular Spectra and Molecular Structure I. Spectra of Diatomic Molecules.* Van Nostrand Reinhold Company, 1950. DOI: `ISBN0442033850` (cit. on pp. 30, 31).

[58] P. H. Krupenie. *The Band Spectrum of Carbon Monoxide.* National Institute of Standards and Technology, 1966. DOI: `https://doi.org/10.6028/NBS.NSRDS.5` (cit. on p. 31).

[59] M. Roloff. *Optische Diagnostik des Einflusses von Katalysatoren auf dielektrisch behinderte Entladungen.* Bachelor Thesis, Ruhr-Universitaet Bochum. 2024 (cit. on pp. 55, 66, 67).

[60] Inc. MKS Instruments. *MKS Tyype 247D Four-Channel Readout, 120714-P1 Rev A, 7/97, Instruction Manual.* Online, Link: http://uhv.cheme.cmu.edu/manuals/ mks. fourchannelreadout .pdf.pdf. 2019 (cit. on p. 69).

Danksagung

An dieser Stelle möchte ich mich bei allen Menschen bedanken, die mir bei der Anfertigung meiner Masterarbeit geholfen haben. Insbesondere möchte ich mich bedanken bei:

- Jun.-Prof. Dr. Judith Golda für die Möglichkeit, meine Masterarbeit in ihrer Arbeitsgruppe zu schreiben und für die hilfreichen Antworten auf meine Fragen in und außerhalb der Meetings.

- Dr. Marc Böke für seine Ratschläge und die Übernahme der Zweitkorrektur.

- Dr. Volker Schulz-von der Gathen für seine Expertise und Hinweise rund um den Laser und TALIF sowie für das Korrekturlesen.

- Henrik van Impel für die ausgezeichnete Betreuung während der gesamten Masterarbeit, auch während einer Konferenz oder im Urlaub, und für seine Programmierkünste in LabVIEW.

- Den Technikern Björn Redeker, Kai Fiegler, Michael Konkowski und Axel Lang, die die nötigen Gasleitungen eingebaut und bei Problemen mit dem Laser geholfen haben.

- Allen anderen Mitgliedern des Lehrstuhls, die diesem eine gute Arbeitsatmosphäre geben.

- Meinen Studiengefährten Daniel Henze und Neil Unteregge, ohne die ich vermutlich schon im ersten Corona-Semester an der Physik verzweifelt wäre.

- Meiner Freundin Julia, die mich während der gesamten Masterzeit unterstützt und mich so manchen schlechten Tag an der Uni mit ihrem Lächeln vergessen lassen hat. Ich liebe dich!

- Meiner Familie, ohne die das Studium unmöglich gewesen wäre. Inbesondere möchte ich mich bedanken bei meiner Mutter Beate, die mir immer den Rücken freigehalten hat, bei meinem Vater und großem Vorbild Heinrich, von dem ich in meinem Leben so viel lernen durfte und noch heute tue, meiner Schwester Anja, die immer ein offenes Ohr für mich hatte, und meinen Großeltern Genowefa und Eva sowie Henryk und Leo, die das Ende des Studiums leider nicht mehr miterleben können.

Ad maiorem Dei gloriam